The Pennsylvania State University

The Graduate School

College of Engineering

TECHNIQUES FOR DESIGNING MICROWAVE AND MILLIMETER WAVE ANTENNAS AND COMPONENTS USING ARTIFICIALLY ENGINEERED MATERIALS AND METASURFACES

A Dissertation in

Electrical Engineering

by

Shaileshachandra V Pandey

Submitted in Partial Fulfillment
of the Requirements
for the Degree of

Doctor of Philosophy

December 2017

The dissertation of Shaileshachandra V Pandey was reviewed and approved* by the following:

Raj Mittra
Professor of Electrical Engineering
Dissertation Advisor
Co-Chair of Committee

Ram Narayanan
Professor of Electrical Engineering
Co-Chair of Committee

James Breakall
Professor of Electrical Engineering

Michael T. Lanagan
Professor of Engineering Science and Mechanics

Kultegin Aydin
Professor of Electrical Engineering
Head of the Department of Electrical Engineering

*Signatures are on file in the Graduate School

ABSTRACT

Recent years have witnessed extensive research into the synthesis of new materials (e.g., metamaterials that typically utilize periodic structures). It is well known that periodic structures comprising metallic patches or apertures behave as artificial dielectrics, and screens that resemble frequency selective surfaces (FSSs) can be used as artificially synthesized materials to replace conventional dielectrics. Several designs have been developed for some applications where metamaterials were engineered by utilizing arrays of small patches or apertures to realize desired electromagnetic behavior for antenna applications, thus improving their performance.

This dissertation begins with an innovative approach for engineering artificial materials or commercial-off-the-shelf (COTS) materials to achieve any dielectric constants that we need to implement flat lens design, which does not suffer from the shortcomings of metamaterials, typically required in designs based on transformation optics (TO). We refer to this technique as “dial-a-dielectric” (DaD). The DaD method is the one in which we tweak the dielectric constants of the artificial material by placing square patches on top of dielectric rings, to achieve the desired dielectric constants. We investigate the use of the proposed technique for synthesizing artificial dielectrics to the design of metasurfaces (e.g., reflectarrays) that have wider bandwidths than those of the present designs, which also utilize resonant elements that rely on resonant inclusions (e.g., narrow bandwidth, dispersion, and loss).

Next, we introduce an alternate design that extends the DaD-based lens design procedure to the dielectric-only reflectarray problem. This reflectarray design is realized

by printing dielectric blocks on a PEC ground plane. The proposed reflectarray design gives a linearly increasing gain variation compared to the bandwidth as typically reported in the literature (i.e., 10% for the designs based on the conventional approach).

This dissertation further explores the design of a flat lens, which utilizes multilayer frequency selective surfaces (FSSs) in *free space.* The lens can be space-qualified since, unlike conventional designs for lenses, it does not need to use dielectric materials. We further describe a systematic procedure for realizing the requisite radially varying phase shifts, by using locally periodic multilayer FSSs to realize a lightweight, low-profile and low-cost design.

Next, we present a novel approach for designing a low-cost phase-shifting device based on the use of reconfigured FSS screens, which have relatively low insertion loss and are easy to fabricate. Our goal is to provide an arbitrary phase shift to the antenna element of an array that it would require for precise control of the beam-pointing to communicate with a satellite.

Lastly, offset-fed-metal-only reflectarrays realized by using cross-slot and cross/cross-groove phasing elements, which are 2D and 3D FSS elements, respectively, are presented. These reflectarray designs are suitable for space applications in which the use of dielectrics is not desired. These FSS elements are chosen such that they can be 3D-printed. We also compare the performances of reflectarrays with the existing metal-only reflectarray design to show the efficacy of the proposed method. The design investigated shows the improved gain, aperture efficiency, and low-profile features.

Table of Contents

List of Figures viii

List of Tables xiii

Acknowledgements xiv

Chapter 1

Overview 1

1.1 Motivation……... 1

1.2 Organization of Dissertation ……. 2

Chapter 2

Lens Designs Using Synthesized Artificial Dielectrics 4

2.1 Introduction ……. 4

2.2 Traditional Lens Design…….. 6

2.2.1 Ray-Optics and Ray-Optics Zone-plate (ZP) Lens Design……. 6

2.3 Technical Approach for Designing Artificially Engineered Materials…… 10

2.3.1 Design Strategy I (Obtaining Higher Dielectric Constant than Base Material Using Single Dielectric) ……. 11

2.3.2 Design Strategy II (Obtaining Lower Dielectric Constants than Base Material Using Multiple Dielectrics)……. 13

2.4 Performance Comparison of RO-Based Lenses with DaD Lens Designs.. 15

2.4.1 RO-Based DaD Lens Design……..... 15

2.4.2 RO(ZP)-Based DaD Lens Design……... 18

2.5 Results…… 20

2.6 Conclusions…… 24

Chapter 3

Dielectric-Only Reflectarray Antenna (DORA) Design Using Metasurfaces 26

3.1 Introduction ……. 26

3.2 DORA Design Using Dielectric Blocks (Metasurfaces)…… 29

3.3 Results……. 35

3.4 Conclusions……. 38

Chapter 4

Flat Lens Design Using Space-qualifiable Multilayer Frequency selective surfaces (FSSs) 39

4.1 Introduction ……. 39

4.2 Traditional Ray Optics (RO) Lens Design…….. 41

4.3 Technical Approach for the Multilayer FSS lens Design…… 44

4.4 Performance Comparison of RO-Based Lens with Multilayer-FSS-Based Planar Lens Design……..... 48

4.5 Comparison of RO- and FSS-Based Planar Lens…… 54

4.6 Conclusions……. 56

Chapter 5

Low-Cost Phase Shifter Design for Beam-Scanning Antennas 58

5.1 Introduction ……. 58

5.2 Design Strategy for Phase-Shifter Design……... 60

5.3 Phase-Shifter in Linear Array for Beam Scanning……. 69

5.4 Results……. 72

Chapter 6

Offset-Fed Metal-Only Reflectarray (MORA) Antenna Designs Using Frequency Selective Surfaces (FSSs) 76

6.1 Introduction ……. 76

6.2 Offset-Fed Metal Only Reflectarray (MORA) Designs…….. 78
6.2.1 Metal-Only Reflectarray Design Using Cross-Slot Element……... 79
6.2.1.1 Results…….. 84
6.2.2 Metal-Only Reflectarray Design Using 3D-Cross Element…… 86
6.2.2.1 Simulated Results for Reflectarray Designs……. 91
6.2.3 Metal-Only Reflectarray Design Using 3D-Cross-Groove Element……... 92
6.2.3.1 Design Steps for Dual-band (Ka/W-band) MORA Design…….. 95
6.2.3.2 Simulation Results for Dual-Band Reflectarrays……..... 100
6.3 Conclusions……. 103

Chapter 7
Conclusions and Future Work 105

Bibliography 109

List of Figures

2.1 (a) Curved lens (Homogeneous dielectric) (b) Flat lens (Radially varying dielectric) ……..…… 4

2.2 Geometry of the RO lens…….. 7

2.3 (a) Trimetric view of proposed DaD lens (b) Unit cell for Design Strategy-I ……..... 12

2.4 (a) Trimetric view of proposed multi-layer lens (b) Unit cell for Design Strategy-II ……...……... 14

2.5 S_{21} parameters of unit cells using Design Strategy I (a) S_{21} magnitude (b) S_{21} phase..... 16

2.6 S_{21} parameters of unit cells using Design Strategy I (a) S_{21} magnitude (b) S_{21} phase..... 17

2.7 S_{21} parameters of unit cells using Design Strategy II (a) S_{21} magnitude (b) S_{21} phase…… 19

2.8 Different DaD lens designs; Trimetric view of (a) RO-based DaD lens with patches (b) RO(ZP)-based DaD lens without patches…… 21

2.9 Gain comparison of different RO-based lenses……. 22

2.10 Gain comparison of different RO (ZP)-based lenses……. 23

2.11 Gain comparison of different RO (ZP)-based lenses……. 24

3.1 Design trends of reflectarray (RA) antenna (a) Parabolic reflector (b) Printed flat RA ……..... 27

3.2 (a) Isometric view (b) Top view of conventional design of reflectarray……... 28

3.3 Isometric view of proposed reflectarray design……..... 30

3.4 Isometric view of the different aperture locations……. 31

3.5 Phase distribution on the different aperture locations…… 32

3.6 Phase comparison on the different aperture locations with dielectric blocks…… 33

3.7 Proposed DORA (a) Isometric view (b) Side view of proposed DORA by using image theory to derive an equivalent lens……. 34

3.8 Comparison of radiation patterns of reflectarrays……..... 36

3.9 Radiation patterns of the different reflectarrays at f_c=15GHz…… 37

3.10 Gain comparison of the different reflectarrays……..... 37

4.1 (a) RO-based flat Lens (b) FSS-based flat Lens..... 40

4.2 Geometry of the traditional RO lens……..... 42

4.3 Top view and side view of the traditional RO lens……. 43

4.4 RO lens and its phase distribution along the diameter of the exit aperture…. 45

4.5 (a) Side view; (b) Top view; Unit cell for achieving phase delays for multilayer-FSS lens……... 47

4.6 Design strategy for FSS-based planar lens…… 49

4.7 S_{21} parameters of unit cells for ring no.2 (a) S_{21} magnitude (b) S_{21} phase….. 50

4.8 S_{21} parameters of unit cells for ring no.5 (a) S_{21} magnitude (b) S_{21} phase….. 51

4.9 S_{21} parameters of unit cells for ring no.8 (a) S_{21} magnitude (b) S_{21} phase….. 52

4.10 S_{21} parameters of unit cells for ring no.10 (a) S_{21} magnitude (b) S_{21} phase… 53

4.11 Top view of proposed multilayer-FSS planar lens……..... 55

4.12 Gain Comparison of different planar lenses…….. 56

5.1 Examples of phase-shifting configurations: (a) Switch-based, (b) Liquid crystal-based…….. 59

5.2 Unit-cell of metasurface-based phase shifter comprising (a) Trimetric view; (b) Top view……..... 61

5.3 Unit cell of the superstrate comprising of nested square split rings: (a) xy-plane; (b) yz-plane; and (c) xz-plane…….. 62

5.4 Performance characteristics of the superstrate unit cell: (a) S_{21} magnitude; (b) S_{21} phase…….. 63

5.5 Metasurface-based superstrate with a rectangular shape loading an MPA source located below: (a) top view; (b) side view……. 65

5.6 Metasurface based superstrate loaded on MPA source (a) Magnitude (dB); (b) Differential Phase (°)……..……..... 65

5.7 Metasurface-based superstrate loading an MPA; (a) rectangular; (b) circular…….. 67

5.8 Metasurface-based superstrate circular shape loaded on MPA source (a) Magnitude (dB); (b) Differential Phase (°)……..……. 68

5.9 Metasurface-based superstrate-loaded linear array of 1×10 elements…… 70

5.10 Linear array of 1×10 elements loaded with the metasurface-based superstrate……..... 72

5.11 Phase comparisons of 1×10 linear array for the scan angle of θ_o = 45°…… 73

5.12 Gain for 1×10 element linear array for different scan angles…… 74

6.1 Design schematics of reflectarray (RA) (a) Parabolic reflector; (b) Printed RA……..... 77

6.2 Cross-slot phasing element, green part is metal and red part is the slot carved out of metal…… 81

6.3 Reflection phase of cross-slot phasing element…… 81

6.4 Metal-only Reflectarray (MORA) using Cross-slot phasing element…….. 82

6.5 Typical Reflectarray derived by using cross-slot phasing elements…….. 82

6.6 Phase comparison of cross-slot reflectarray along x-axis at y=0 for radiation in normal direction. …… 84

6.7 Simulated radiation pattern of the MORA designed using cross-slot phasing element in the normal direction…… 85

6.8 Simulated radiation pattern of the MORA designed using cross-slot 85

phasing element in the specular direction…….

6.9 3D-Cross phasing element, green part is 3D metallic element and red part ground plane…….. 87

6.10 Reflection phase of 3D-cross phasing element……..... 88

6.11 Metal-only Reflectarray using 3D-Cross phasing element…… 88

6.12 Typical Reflectarray derived by using 3D-cross phasing elements…..…….. 89

6.13 Phase comparison of 3D-cross reflectarray along x-axis at y=0 for radiation in normal direction. ……... 90

6.14 Simulated radiation pattern of the MORA designed using 3D-Cross phasing element……. 91

6.15 Ka-band (Low-frequency(Lf)) phasing element (a) Top view; (b) Trimetric view……... 93

6.16 Reflection phase of cross-groove phasing element for different groove widths..…… 94

6.17 W-band (high-frequency(Hf)) phasing element (a) Top view; (b) Trimetric view……... 94

6.18 Reflection phase of cross-groove at *f* (design frequency) = 94.05GHz, for different groove-width……... 95

6.19 Dual-band (Ka/W-band) phasing element (a) Top view; (b) Trimetric view…….…….. 98

6.20 Reflection phase of Hf phasing element depth by fixing Lf element depth = 1mm……... 98

6.21 Offset-fed Ka-band proposed MORA using cross-groove phasing element.. 99

6.22 Proposed dual-band metal-only reflectarray…… 99

6.23 Simulated radiation pattern of the dual-band MORA using cross-groove phasing element in presence of W-band elements……... 101

6.24 Simulated radiation pattern of the dual-band MORA using cross-groove phasing element in presence of Ka-band elements……. 102

6.25 Gain response within desired frequency band of the proposed Ka-band 102

MORA in presence of W-band elements……...

6.26 Gain response within desired frequency band of the proposed W-band MORA in presence of Ka-band elements…….……. 103

List of Tables

2.1 Material parameters for RO lenses…….. 8

2.2 Material parameters for RO(ZP) lenses……... 9

2.3 COTS material available from ROGERS for lens design…… 10

3.1 Material parameters along the x-axis at y=0mm……..... 33

3.2 Material parameters for the DORA……..... 35

4.1 Material parameters of traditional RO lens……..... 43

4.2 Parameters of FSS-based planar lens……... 55

5.1 Dimensions of metasurface-based phase-shifting element.……. 62

5.2 Desired Phase shifts needed for the array scan angle of $\theta_o = 45°$……. 71

5.3 Phase comparison of 1×10 linear array for the scan angle of $\theta_o = 45°$…….. 73

5.4 Gain values for the different beam scan angles……..... 74

6.1 Phase comparison of cross-slot reflectarray for the beam angle of $\theta_b = 0°$…... 83

6.2 Phase comparison of 3D-cross reflectarray for the beam angle of $\theta_b = 0°$…… 90

6.3 Phase comparison of Ka-band, cross-groove reflectarray for the beam angle of $\theta_b = 0°$……..... 100

6.4 Radiation performances of proposed MORA for the beam angle of $\theta_b = 0°$… 104

ACKNOWLEDGEMENTS

I would like to express my sincerest gratitude to my dissertation advisor, Dr. Raj Mittra. Without his inspiration, guidance, support and encouragement throughout this dissertation would not have been possible. He always encourages me to think about the objective and physics behind the problem. It has been a great honor to have him as my Ph.D. advisor.

I am also grateful to my other committee members—Dr. Ram Narayanan, Dr. Jim Breakall and Dr. Michael Lanagan—for taking out the time from their busy schedule to serve on my committee and provide their suggestions on my dissertation.

I would like to acknowledge and thank my colleagues in the Electromagnetic Communication Laboratory, namely Dr. Kadappan Panayappan, Dr. Chiara Pelletti, Dr. Giacomo Bianconi, Dr. Sidharath Jain, Dr. Yuda Zhou, Dr. Ravi Kumar Arya, Mr. Mohamed Abdel-Mageed and Mr. Kapil Sharma. I would also like to thank Dr. Shiyu Zhang and Dr. Yiannis Vardaxoglou from Loughborough University for their help with the fabrication and measurement of the prototype.

I am grateful to Ms. SherryDawn Jackson and Ms. Lisa Timko, without whom I could not have made it to this point.

I would also like to thank Dr. Dilip K. Kothari for motivating me to select an Electromagnetic and RF Engineering as my research area for future career.

Finally, and most importantly, I would like to thank my grandfather, Dr. Rajnath Pandey, for teaching me the importance of education in life from my childhood and helping me to choose the right career. My parents, Vachaspati & Gayatri Pandey; my uncle and

aunt, Satyendra & Shakuntala Pandey; my wife, Namrata Pandey and my children, Medha and Mrudul for their overwhelming love and support throughout the program at Penn State.

A special mention to my in-laws, Dr. Hridaynarayan Mishra and Dr. Divyakant Mishra, for their consistent and constant encouragement during the program. My journey would not have been possible without the dedication and encouragement of my wife during my difficult times in this program.

DEDICATION

To my lovely children, Medha and Mrudul, for their love which gave me the strength during my critical times in this program and my wife for her love, endless support and encouragement.

Chapter 1

Overview

1.1 Motivation

Recent years have witnessed a great deal of attention being devoted to the problem of controlling electromagnetic fields by using artificially engineered materials to design and develop the antennas for microwaves, millimeter waves, and terahertz frequencies.

Further incorporating the trends in designing the antennas for millimeter waves, we look into the flat lens and reflectarray designs. We present a systematic technique, referred to (due to the design of artificially engineered dielectric materials) as dial-a-dielectric (DaD) and tailored to the needs of the flat lenses or metasurfaces. This technique is useful for designs of microwave components for which permittivity values are usually commercially unavailable.

We further introduce an alternate design for reflectarrays using dielectric blocks, which is the extension of DaD-based lens design procedure to the reflectarray problem. The motivation behind the approach is the narrow bandwidth (i.e., 10% for the reflectarray designs based on the conventional approach).

We also further investigate the artificially synthesized materials to replace the conventional dielectrics. These artificially synthesized materials comprise periodic structures such as metallic patches and apertures, or combinations thereof. We seek to use such artificial dielectrics where the use of conventional dielectrics is not permissible (i.e., space applications). We investigated the approach of using locally periodic multilayer FSSs to realize the desired radially varying phase delays without unduly compromising the

magnitude of S_{21}. We also present a novel approach to designing phase shifters for array antennas for satellite communication by using reconfigurable FSS screens where, unlike conventional dielectrics, we can control their effective medium properties relatively easily without having to use electric fields. This provides us great advantages regarding ease of fabrication, cost, and loss characteristics. We also look into the illustrative designs of metal-only reflectarrays, designed by using metallic 2D and 3D FSS phasing elements. These designs are also suitable for space applications with the motivation earlier described.

1.2 Organization of Dissertation

This dissertation is organized into seven chapters.

Chapter 2 presents an innovative method for designing flat lenses by using artificially engineered materials. We propose the DaD technique to design different types of lenses in this chapter and have compared their performance characteristics with the conventional lens design.

Chapter 3 shows the dielectric-only reflectarray (DORA) design, which is an extension of the work done in Chapter 2. We design the reflectarray using dielectric blocks printed on a PEC plane. We also show the linearly increasing gain performance of the proposed design.

Chapter 4 introduces the FSS-based multi-layer lens design for space applications. The proposed lens design does not use dielectrics. The performance characteristics are compared with the conventional lens design.

Chapter 5 shows the novel phase-shifter design that is designed using metasurfaces.

The phase-shifter is loaded on the linear arrays, and beam scanning is observed.

Chapter 6 presents a single- as well as dual-band metal-only reflectarray design. We introduce the 2D and 3D phasing elements to design the reflectarrays.

The last chapter, Chapter 7, summarizes and draws conclusions from the investigations performed. It also shows the directions for further extension of the work.

Chapter 2

Lens Designs Using Synthesized Artificial Dielectrics

2.1 Introduction

A lens is a popular antenna component that collimates incident diverging waves to prevent them from widening in undesired directions. It also collimates a spherical or cylindrical wavefront emanating from a point or line source located at the focal point into an outgoing planar wavefront; therefore, it can be used for antenna application to realize a highly directive beam. However, conventional lenses are made from homogeneous materials that are not attractive for antenna applications due to their curved surfaces (Fig. 2.1(a)). In contrast, a flat lens (Fig. 2.1(b)) has a low profile, is lightweight, and could be easily used in proximity to the feed source, which makes it an excellent choice for antenna applications.

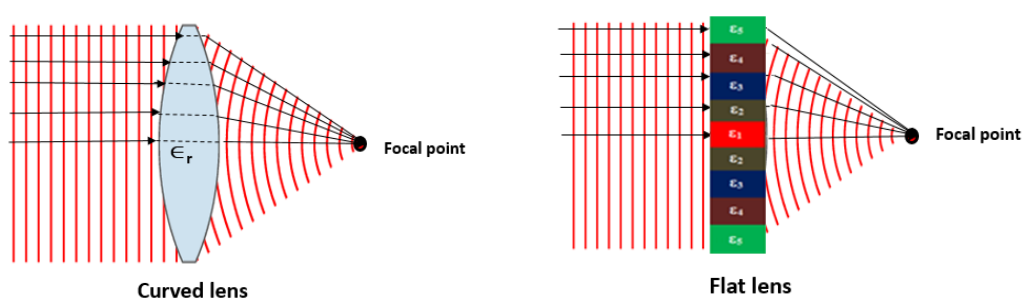

(a) (b)

Fig. 2.1 (a) Curved lens (Homogeneous dielectric) (b) Flat lens (Radially varying dielectric)

Recent years have witnessed a great deal of attention devoted to the problem of controlling electromagnetic fields by using engineered materials, to design flat lenses [1] -

[10] that are based on transformation optics (TO) and other techniques. These materials not only provide improved performance characteristics for these devices but also help in developing them with compact footprints. The TO approach, which is very elegant and systematic, often leads to designs based on metamaterials that can be difficult to realize because they require ϵ_r and μ_r values that are either less than 1 or very large, or both. Contemporary approaches to avoid these problems and develop ϵ-only designs have recently been developed by a number of researchers, though this is still noted as "work in progress."

When the lens applications start to move towards the higher frequencies, the dimensions and weights become smaller. Researchers are still developing innovative approaches to make low-profile and thin flat lenses where the major applications are covered and one need not move towards the expensive techniques. The traditional ray optics (RO) approach, although it leads to dielectric-only designs without the need to use magnetic materials, still requires dielectric materials that may not be available off-the-shelf.

In this chapter, we discuss the design of flat lenses using artificial dielectrics that are slightly modified versions of commercial-off-the-shelf (COTS) materials, which do not suffer from the shortcomings of metamaterials (MTM) that are typically required in designs based on TO(e.g., narrow bandwidth, dispersion and loss). We also investigate the use of the proposed technique for synthesizing artificial dielectrics to the design of metasurfaces (e.g., reflectarrays) that have much wider bandwidths than those of the present designs that also utilize resonant elements that rely on resonant inclusions. The design procedure also enables us to control the matching characteristics by utilizing a multilayer approach, which

provides more design flexibility than is available in the TO approach.

In the following sections, we show different designs to demonstrate the procedure for synthesizing artificial dielectrics that are of single-layer as well as multilayer design. The latter design enables us to control the matching characteristics, which provides more design flexibility than is available with the TO approach.

2.2 Traditional Lens Designs

2.2.1 Ray-Optics(RO) and Ray-Optics Zone-plate (ZP) Lens Design

We proceed to design the traditional RO lens by using the methodology described in [10]. Fig. 2.2 shows the geometry of the RO lens. The specifications for the RO lens are (i) required gain, (ii) center frequency f=30GHz, (iii) focal length F=12.7mm, and (iv) thickness h=9mm. The diameter D of the lens is chosen to be 63.5mm on the basis of the gain requirements. We use 10 discrete rings for the lens, each with a width of 3.175mm along the transverse direction. The dielectric parameters are chosen to satisfy the path length condition of these rings and are shown in Table 2.1. We also modify these parameters to design a zone-plate (ZP) version of the lens, to reduce the $\in_r$ values; the parameters of the ZP lens are shown in Table 2.2. We can see that the ZP version helps the lens, which would make it easier to find the required COTS materials easily to build as compared to the RO lens. For further study, we herewith include the dielectric constants of the most commonly available COTS materials in Table 2.3.

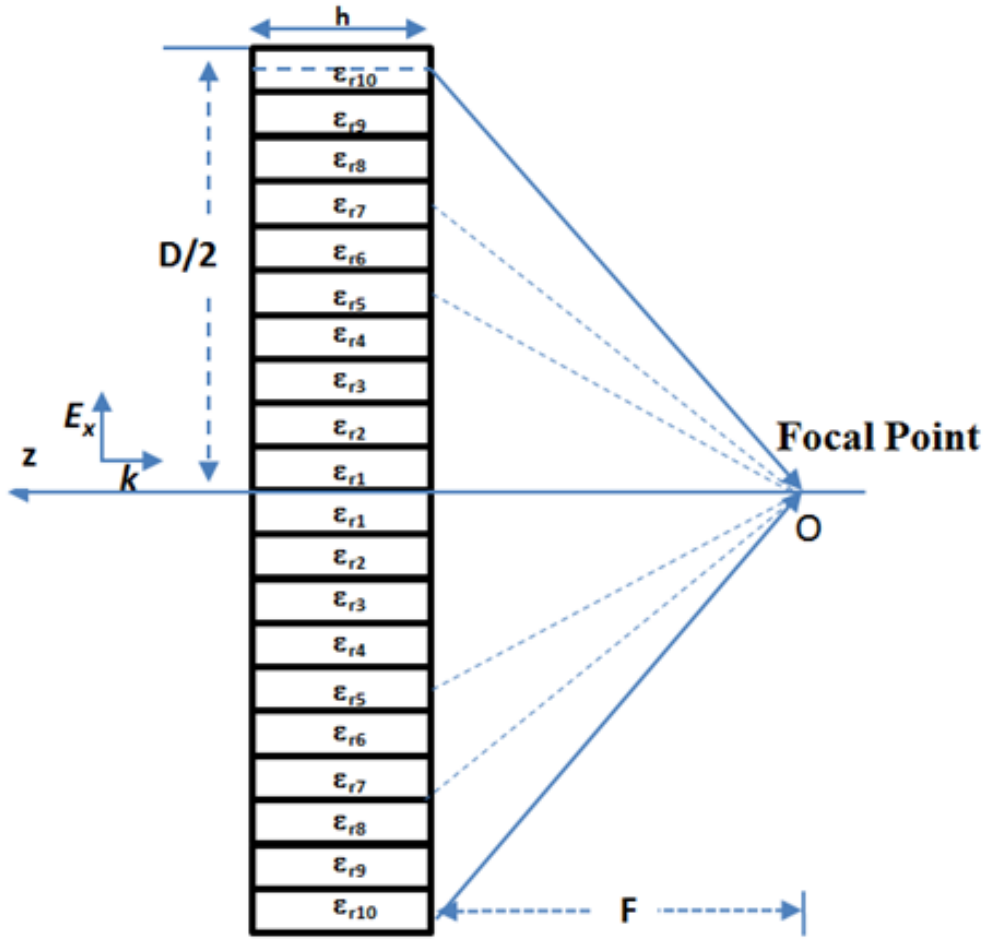

Fig. 2.2. Geometry of the RO lens

Table 2.1: Material parameters for RO lenses

Ring No.	RO Lens	RO COTS Lens	RO DaD Lens (dielectric + dielectric) without patches		RO DaD Lens (dielectric + dielectric) with patches		
	$\epsilon_{r\_desired}$	$\epsilon_{r\_available}$	ϵ_1/ϵ_2	t_1/t_2 (mm)	ϵ_1/ϵ_2	a (mm)	t_1/t_2 (mm)
1	11.15	10.2	$\epsilon_1 = 10.2$ $\epsilon_1 = 1$	$t_1 = 9$ $t_2 = 0$	$\epsilon_1 = 10.2$ $\epsilon_1 = 1$	1.25	$t_1 = 9$ $t_2 = 0$
2	10.64	10.2	$\epsilon_1 = 10.2$ $\epsilon_1 = 1$	$t_1 = 9$ $t_2 = 0$	$\epsilon_1 = 10.2$ $\epsilon_1 = 1$	0.98	$t_1 = 9$ $t_2 = 0$
3	9.8	9.8	$\epsilon_1 = 9.8$ $\epsilon_1 = 1$	$t_1 = 9$ $t_2 = 0$	$\epsilon_1 = 9.8$ $\epsilon_1 = 1$	-	$t_1 = 9$ $t_2 = 0$
4	8.7	9.2	$\epsilon_1 = 9.2$ $\epsilon_2 = 6.15$	$t_1 = 8$ $t_2 = 1$	$\epsilon_1 = 9.2$ $\epsilon_2 = 6.15$	-	$t_1 = 8$ $t_2 = 1$
5	7.45	6.15	$\epsilon_1 = 9.2$ $\epsilon_2 = 6.15$	$t_1 = 4.3$ $t_2 = 4.7$	$\epsilon_1 = 9.2$ $\epsilon_2 = 6.15$	-	$t_1 = 4.3$ $t_2 = 4.7$
6	6.15	6.15	$\epsilon_1 = 6.15$ $\epsilon_2 = 1$	$t_1 = 9$ $t_2 = 0$	$\epsilon_1 = 9.2$ $\epsilon_2 = 6.15$	-	$t_1 = 9$ $t_2 = 0$
7	4.88	4.7	$\epsilon_1 = 6.0$ $\epsilon_2 = 4.7$	$t_1 = 1.58$ $t_2 = 7.42$	$\epsilon_1 = 9.2$ $\epsilon_2 = 6.15$	-	$t_1 = 1.58$ $t_2 = 7.42$
8	3.7	3.66	$\epsilon_1 = 4.5$ $\epsilon_2 = 3.66$	$t_1 = 0.78$ $t_2 = 8.22$	$\epsilon_1 = 9.2$ $\epsilon_2 = 6.15$	-	$t_1 = 0.78$ $t_2 = 8.22$
9	2.64	2.75	$\epsilon_1 = 2.75$ $\epsilon_2 = 2.5$	$t_1 = 5.4$ $t_2 = 3.6$	$\epsilon_1 = 9.2$ $\epsilon_2 = 6.15$	-	$t_1 = 5.4$ $t_2 = 3.6$
10	1.73	2.17	$\epsilon_1 = 1.96$ $\epsilon_2 = 1$	$t_1 = 7.25$ $t_2 = 1.75$	$\epsilon_1 = 9.2$ $\epsilon_2 = 6.15$	-	$t_1 = 7.25$ $t_2 = 1.75$

Table 2.2: Material parameters for RO(ZP) lenses

Ring No.	RO (ZP) Lens	RO (ZP) COTS Lens	RO (ZP) DaD Lens (dielectric + dielectric)			RO (ZP) DaD Lens (dielectric + dielectric) without patches	
	$\epsilon_{r\_desired}$	$\epsilon_{r\_available}$	ϵ_r	a (mm)	t_1/t_2 (mm)	ϵ_r	t_1/t_2 (mm)
1	4.96	4.7	4.7	0.98	--	$\epsilon_1 = 6.0$ $\epsilon_2 = 4.5$	$t_1 = 3.1$ $t_2 = 5.9$
2	4.62	4.5	4.5	0.81	--	$\epsilon_1 = 4.7$ $\epsilon_2 = 4.5$	$t_1 = 5.8$ $t_2 = 3.2$
3	4.08	3.66	3.66	1.43	--	$\epsilon_1 = 4.5$ $\epsilon_2 = 3.66$	$t_1 = 4.7$ $t_2 = 4.3$
4	3.38	3.27	3.27	0.95	--	$\epsilon_1 = 3.55$ $\epsilon_2 = 3.27$	$t_1 = 4.3$ $t_2 = 4.7$
5	2.62	2.5	2.5	0.95	--	$\epsilon_1 = 3.0$ $\epsilon_2 = 2.5$	$t_1 = 2.52$ $t_2 = 6.48$
6	1.87	1	$\epsilon_1 = 2.17$ $\epsilon_2 = 1.0$	0.4	$t_1 = 2.1$	$\epsilon_1 = 1.96$ $\epsilon_2 = 1.0$	$t_1 = 8.25$ $t_2 = 0.75$
7	1.20	1	$\epsilon_1 = 2.17$ $\epsilon_2 = 1.0$	0.76	$t_1 = 0.76$	$\epsilon_1 = 1.96$ $\epsilon_2 = 1.0$	$t_1 = 2.3$ $t_2 = 6.7$
8	3.7	3.66	3.66	0.8	--	$\epsilon_1 = 4.5$ $\epsilon_2 = 3.66$	$t_1 = 0.78$ $t_2 = 8.22$
9	2.64	2.5	2.5	1	--	$\epsilon_1 = 2.75$ $\epsilon_2 = 2.5$	$t_1 = 5.4$ $t_2 = 3.6$
10	1.73	1	$\epsilon_1 = 2.17$ $\epsilon_2 = 1.0$	0.66	$t_1 = 3.1$	$\epsilon_1 = 1.96$ $\epsilon_2 = 1.0$	$t_1 = 7.25$ $t_2 = 1.75$

Table 2.3: COTS material available from ROGERS for lens design

Rogers RT/duroid	1.96
	2.17, 2.2, 2.33, 2.5, 2.75, 2.94
	3, 3.02, 3.2, 3.27, 3.55, 3.66
	4.5, 4.7
	6, 6.15
	9.2, 9.8
	10.2

We introduce a novel technique for engineering artificial materials or COTS materials to achieve any dielectric constants that we need to implement our design. We refer to this technique as “dial-a-dielectric” (DaD). The DaD method is the one in which we tweak the dielectric constants of the artificial material by placing square patches on top of dielectric rings, to achieve the desired dielectric constants. The novelty of this method is that it does not rely on resonance properties of patches or apertures to realize the artificial dielectrics. As a result, it bypasses the problems of losses and narrow bandwidths suffered by materials synthesized by some of the other methods described in [6]-[10]. However, it is useful to model both the conventional and the ZP versions, as they serve as benchmarks for the DaD-based designs that are demonstrated in the following sections.

2.3 Technical Approach for Designing Artificially Engineered Materials

We hasten to point out that the required materials for the RO and RO(ZP) lenses designed in Section 2.1 are typically unavailable (Tables 2.1 and 2.2). Therefore, we must resort to

artificial synthesis of these materials, say by using the DaD approach to realize a practical design. After determining the required dielectric materials for the lens design, we developed the following design strategies to achieve the desired dielectric materials.

2.3.1 Design Strategy-I (Obtaining Higher Dielectric Constant than Base Material Using Single Dielectric)

In this scenario, we begin with COTS dielectric materials whose parameters are close to the desired ones, and then tweak them by introducing either patches or apertures that are small compared to the wavelength at the operating frequency to achieve the desired $\in$r values artificially. We refer to this procedure in this work as "dial-a-dielectric" or DaD. A typical DaD design for a flat lens is shown in Fig.2.3 (a). As mentioned above, we choose the closest COTS material available for desired $\in_r$ and then tweak it by printing patches on top of the dielectric material to realize the desired $\in_r$.

The detail of this procedure is illustrated in Fig.2.3 (b). We carry out the simulation of the unit cell by using a plane-wave source placed below the COTS materials and patch combination, in Port-1, along with the periodic boundary conditions (PBC) in the commercial EM solver i.e., Ansys HFSS. In this figure, *t* is thickness of COTS dielectric material, *a* is the patch dimension, and *b*=1.58*mm* is the unit cell dimension of a "locally periodic" structure comprising a patch or an aperture used to perturb the $\in_r$. The periodicities were chosen on the order of $\lambda/10$, far away from the resonance of the structure comprising the unit cell, in order to ensure that the design would be relatively wideband.

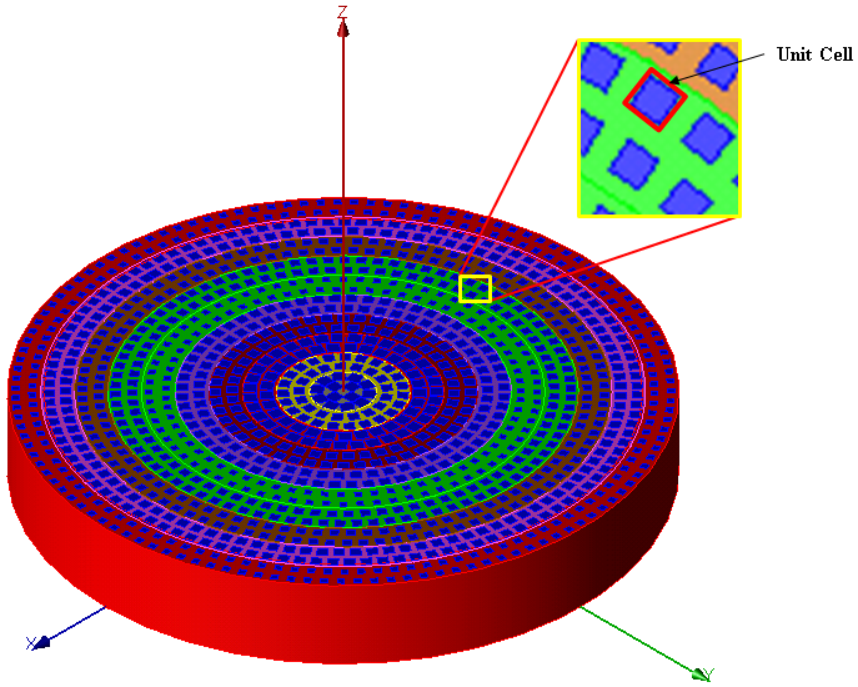

(a)

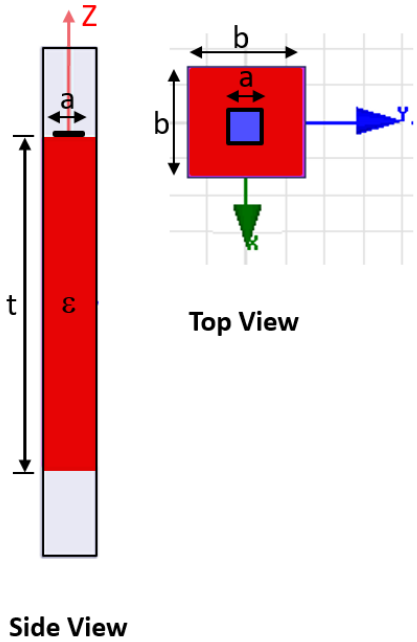

(b)

Fig. 2.3. (a) Trimetric view of proposed DaD lens (b) Unit cell for Design Strategy-I

2.3.2 Design Strategy II (Obtaining Lower Dielectric Constants than Base Material Using Multiple Dielectrics)

The second case is a generalization of the first scenario described above. In this approach, we begin by using a multilayer structure comprising a stacking of COTS materials, not only to realize the desired ϵ_r, but also to realize a matching behavior that reduces the reflection at the interface. We still have the flexibility of tweaking the composite structure by using patches or apertures, printed on top of the composite, to fine-tune the ϵ_r. We should point out that this strategy also works well if the composite was realized in an alternate manner (e.g., by using 3D printing or by mixing two different dielectric materials). The reason why we often need to tweak these materials is because the original realizations of these materials often miss the mark. It is much more practical to tweak them rather than start from scratch, since redoing the whole thing from the beginning is both time-consuming and cost-prohibitive. An example of a multilayer composite, which has been tweaked by using small rectangular patches, is shown in Fig.2.4. Here, t_1 and t_2 are the thicknesses of the COTS materials ϵ_1 and ϵ_2 that we combined to achieve the desired ϵ_r.

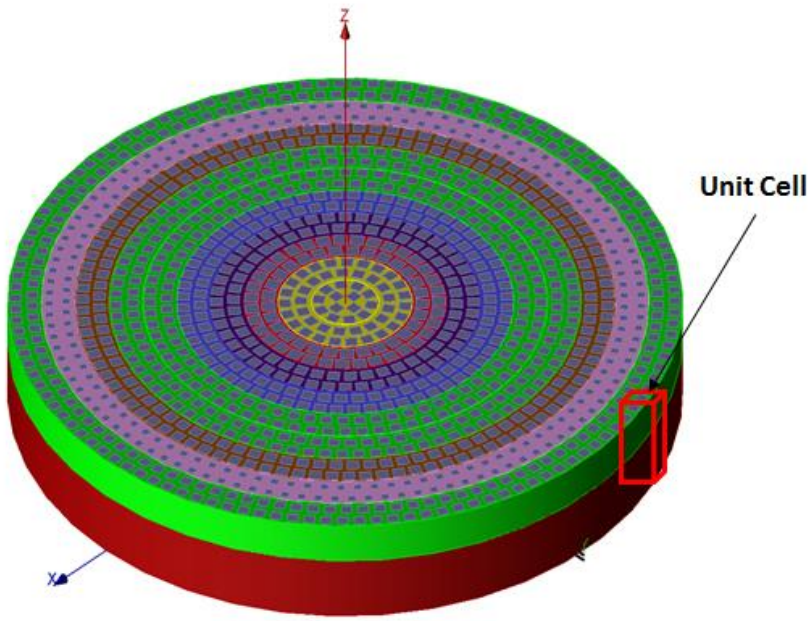

(a)

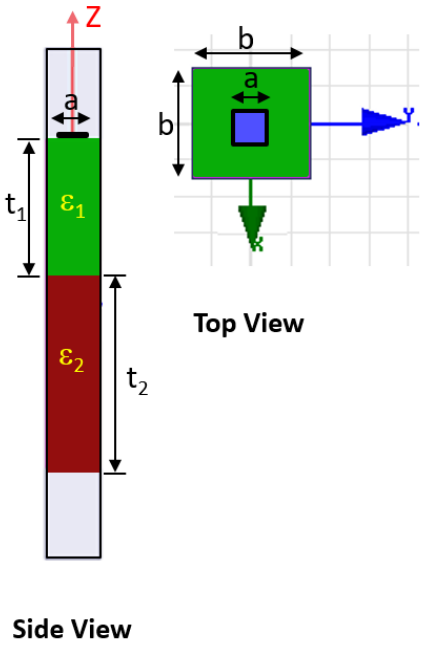

(b)

Fig. 2.4. (a) Trimetric view of proposed multi-layer DaD lens (b) Unit cell for Design Strategy-II

Finally, we choose the dimensions of the patches such that the phase of S_{12} of a purely dielectric layer matches the one in which the COTS materials are covered by the patch. The DaD approach to synthesizing dielectrics yields materials that have performance characteristics similar to those of COTS materials. Hence, they are the preferred choice to typical MTMs that are based on the use of resonant inclusions, which suffer from narrow bandwidths, dispersion and losses.

2.4 Performance Comparison of RO-based Lenses with DaD Lens Designs

2.4.1 RO-based DaD Lens Design

For the RO-based DaD lens design, we start with a COTS material and use the methodology discussed in Section 2.3. A quick search from Table 2.1 reveals that not all of the desired materials ($\in_{r\_desired}$) are commercially available from vendors such as Rogers. We start by selecting the local unit cells for the rings to be 1.58mm × 1.58mm, for which COTS materials with desired dielectric values are not available to complete the RO-based DaD lens design. Design parameters for the unit cell as shown in Fig. 2.3 (b) are chosen to be b=1.58mm, t=9mm, and $\in_r$=4.7. We have chosen patch size (*a*)=0.98mm such that the phase of S_{21} of a desired dielectric layer matches one in which the COTS materials are covered by the patch (i.e., DaD approach). This is the key concept behind the low-loss design in which the patch dimensions are varied very little with the combination of COTS material. Note that the periodicity varies locally to realize the level of perturbation needed. It is worthwhile to point out that the DaD design is carried out by taking advantage of the "locally periodic" property of the design, which enables us to impose the periodic boundary

conditions on a unit cell to reduce the original problem to a manageable size, substantially reducing the computational burden in the process by using the EM simulator Ansys HFSS. In Figs.2.5 and 2.6, we show the validity of Design Strategy-I by comparing the transmission coefficients of the dielectric unit cells of the $\in_{r\_desired}$ as well as DaD approach-based designs for a few rings as an example for the RO-based DaD lens design. We can see from the S_{21} phase plots as shown in Figs. 2.5(b) and 2.6(b) that there is a close agreement between the $\in$r-desired and DaD approaches, which means that we are able to realize the desired $\in$r using the design strategies as mentioned in Section 2.3. Next, we move towards the final design phase where we use the square patches arranged in circular pattern as shown in Fig.2.3(a).

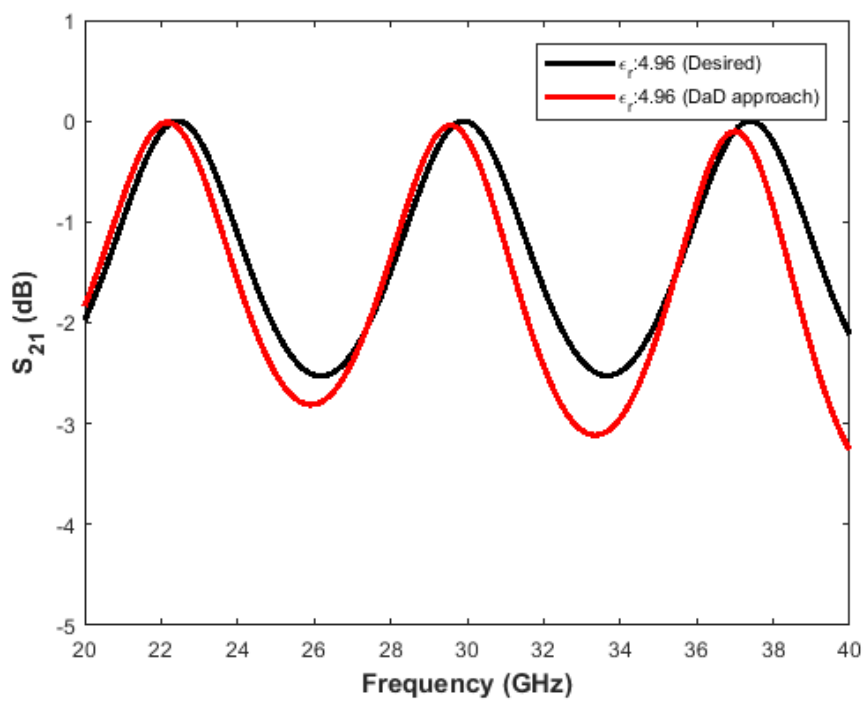

(a)

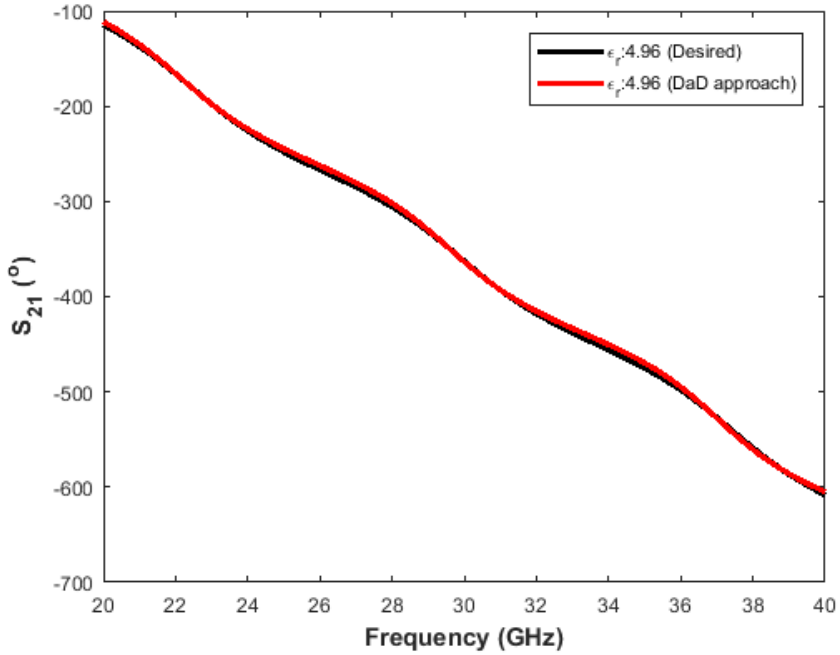

(b)

Fig. 2.5. S_{21} parameters of unit cells using Design Strategy I (a) S_{21} magnitude (b) S_{21} phase

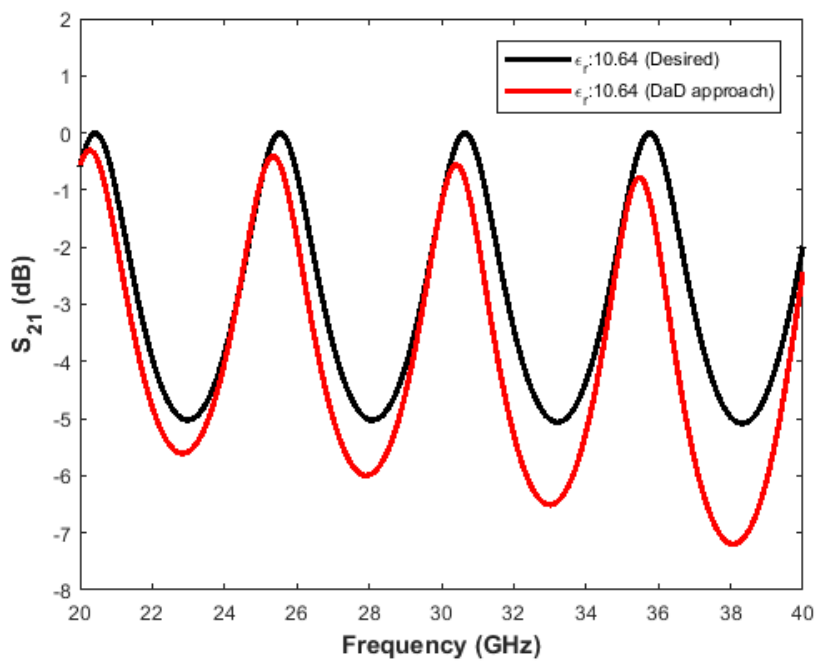

(a)

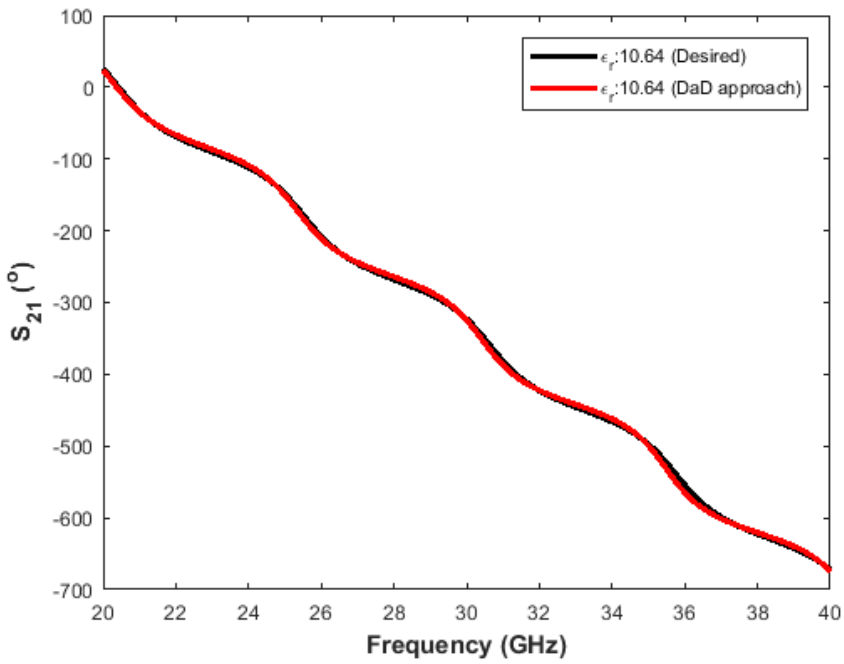

(b)

Fig. 2.6. S_{21} parameters of unit cells using Design Strategy I (a) S_{21} magnitude (b) S_{21} phase

2.4.2 RO(ZP)-based DaD Lens Design

For the RO(ZP)-based DaD lens design, we can quickly check from Table 2.2 that the dielectric values calculated are based on the 2π subtraction from the phase variations of the RO-based lens design. We would like to point out that the method of zone-plating has helped us to reduce the required values of the material parameters, which eases the difficulties of finding the closest COTS material to develop the RO(ZP)-based DaD lens design. We use the methodology as mentioned in Section 2.3 to achieve those dielectric materials needed to design the RO(ZP)-based DaD lens design. We can check from Table 2.2 that the RO(ZP)-based DaD lens design can be completed using dielectric-plus-dielectric combinations, either with or without patches. As stated earlier, the EM

simulations are conducted in HFSS to complete the final design. In Fig.2.7, we show the S_{21} behavior of dielectric unit cells designed based on Design Strategy-II. The S_{21} phase as shown in Fig.2.7 (b) shows comparable performance, which means that the desired dielectric material was achieved using the methodologies discussed in the above section. We move forward and complete the RO (ZP)-based DaD lens design where we use the square patches arranged in a circular pattern with the composite unit cell (i.e., dielectric plus dielectric) as shown in Fig.2.3 (a).

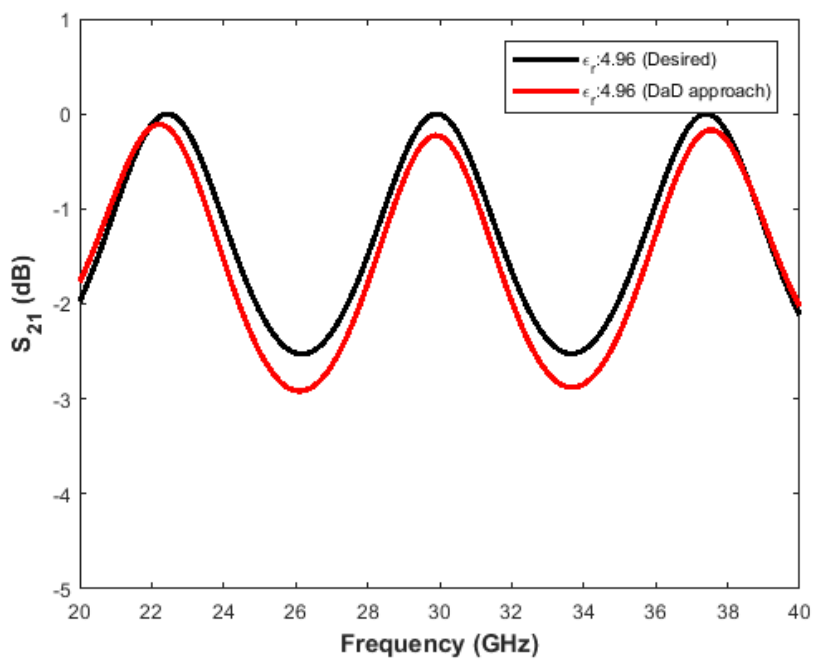

(a)

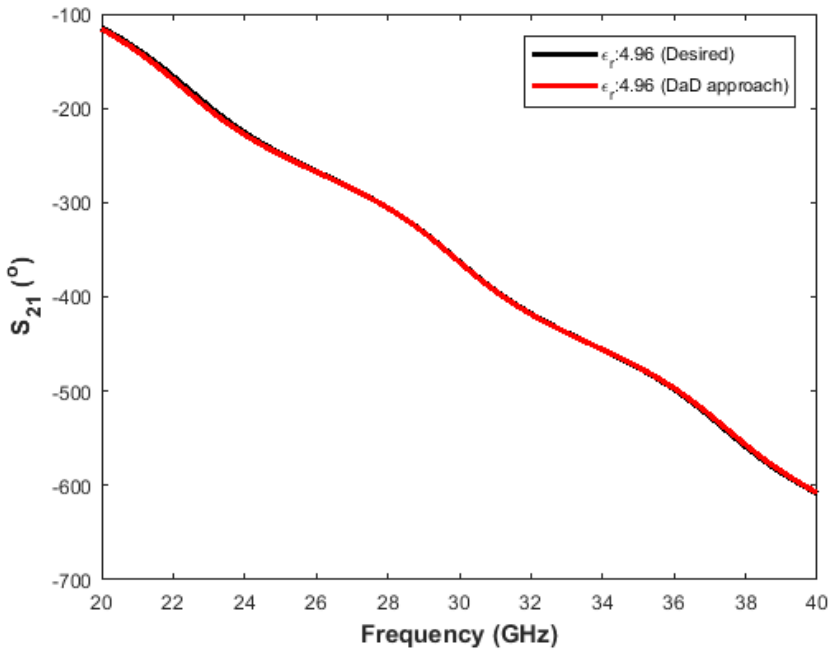

(b)

Fig.2.7. S_{21} parameters of unit cells using Design Strategy II (a) S_{21} magnitude (b) S_{21} phase

2.5 Results

We have completed the final designs of the lenses discussed above (i.e., RO-based and RO (ZP)-based DaD lens designs) as shown in Figs.2.8 and 2.9, whose parameters are given in Tables 2.1 and 2.2.

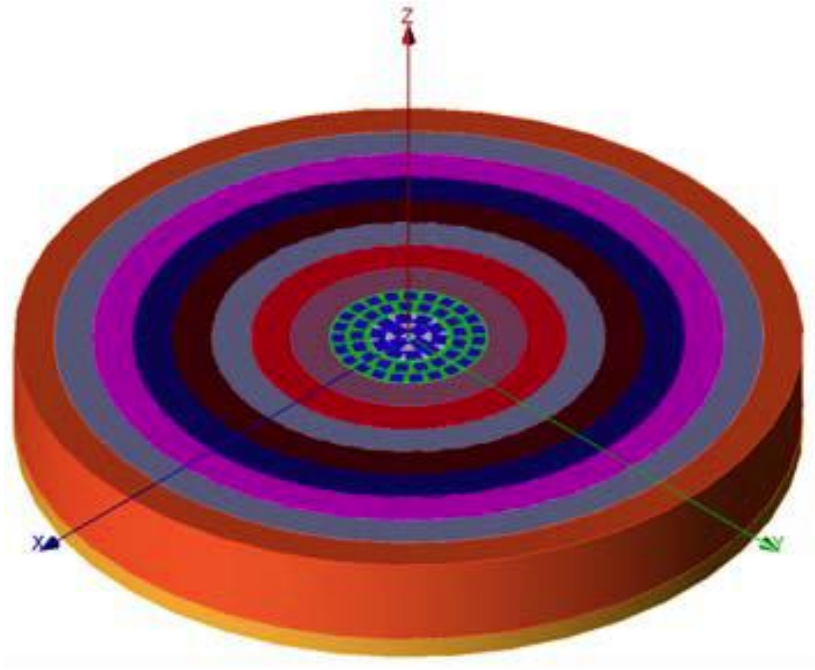

(a)

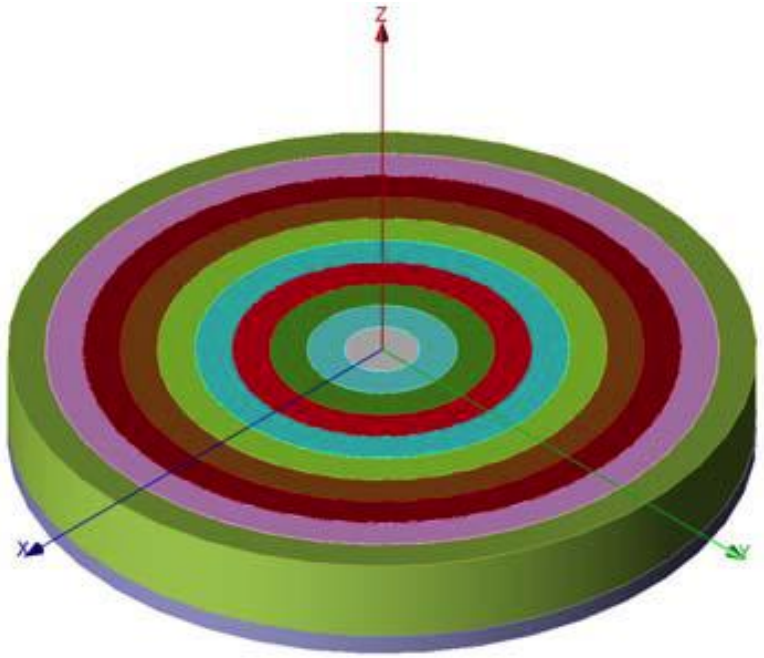

(b)

Fig.2.8. Different DaD lens designs; Trimetric view of (a) RO-based DaD lens with patches (b) RO (ZP)-based DaD lens without patches

Four different designs for the lens have been investigated in the above research. They are (i) RO lens, (ii) RO (ZP) lens, (iii) RO (ZP) COTS lens, and (iv) RO (ZP) COTS lens (DaD lens design) with patches, and their performance characteristics are compared in Figs.2.9 and 2.10.

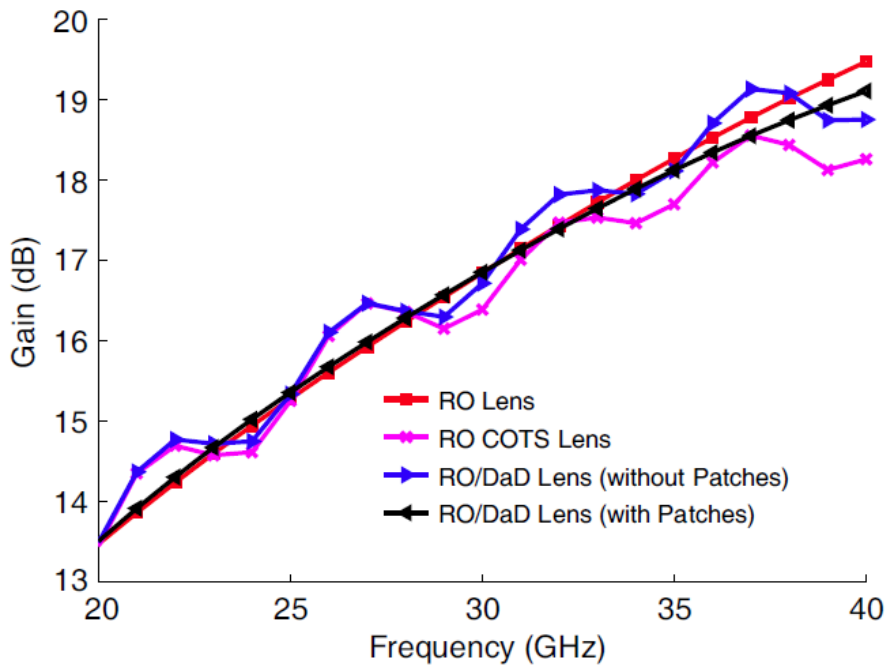

Fig.2.9. Gain comparison of different RO-based lenses

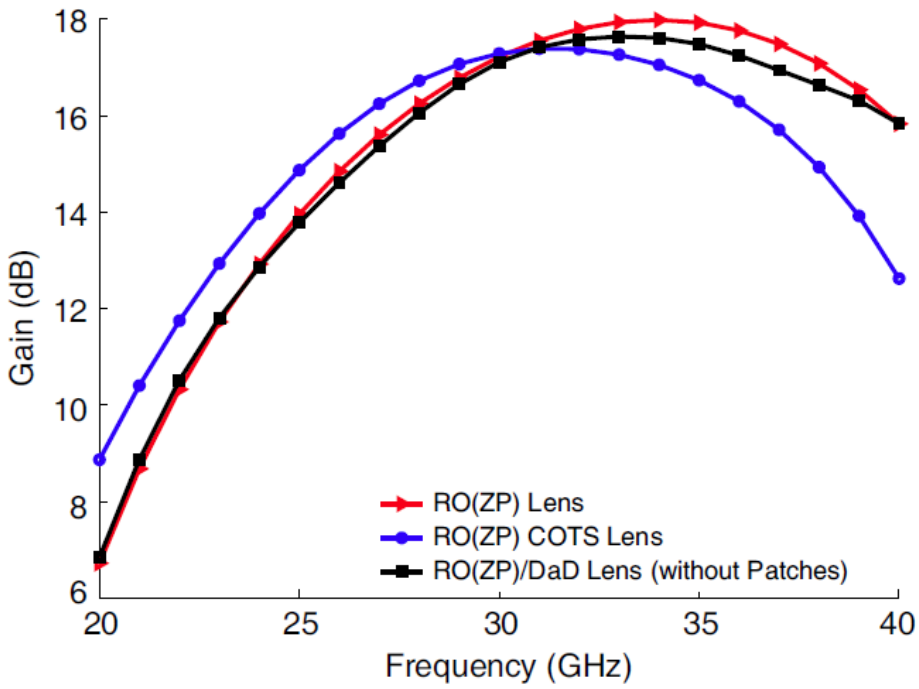

Fig. 2.10. Gain comparison of different RO (ZP)-based lenses

The above plots show the gain comparison for different versions of the RO lens (i.e., the RO lens, RO COTS lens, RO/DaD lens without patches, and RO/DaD lens with patches). It is seen from Fig.2.9 that the DaD-based lens performs well in the desired operating frequency band (i.e., 20-40GHz) when compared to the RO lens, for which dielectric materials are typically unavailable off-the-shelf [13]. Fig.2.10 shows the gain comparisons of the RO (ZP) (i.e., the RO (ZP) lens, RO(ZP) COTS lens, and RO(ZP)/DaD lens without patches).

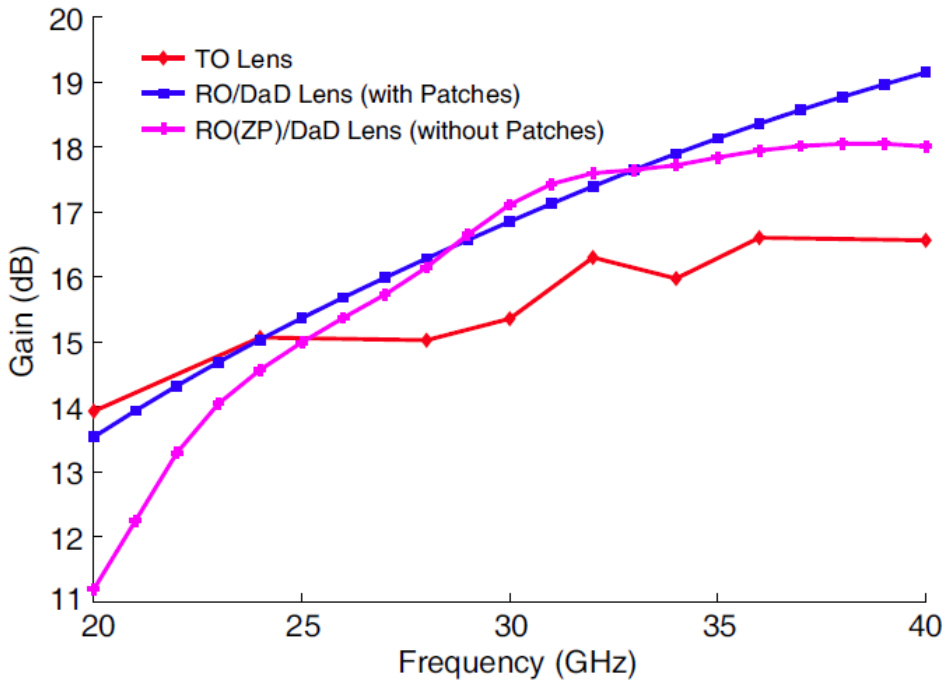

Fig.2.11. Gain comparison of different RO(ZP)-based lenses

The gain comparison of the above lenses was made with flat lens design based on the transformation optics (TO) approach stated in [9], for which plots are shown in Fig. 2.11. It is evident that the DaD-based lenses perform better than the TO-based design. We also note that the ZP version does not perform as well as the non-ZP RO/DaD lens.

2.6 Conclusions

In this chapter, we presented a new lens design (i.e., dial-a-dielectric), which was designed for the center frequency of 30GHz, where desired operating frequency ranges from 20 to 40GHz. The performance of the lens realized by following the strategy outlined earlier is comparable to that of the original RO lens, which requires materials that are not available

COTS. It has wide operating bandwidth and superior gain performances compared to the TO-based lens.

Chapter 3

Dielectric-Only Reflectarray Antenna (DORA) Design Using Metasurfaces

3.1 Introduction

With the increasing demands on point-to-point communication, radar, and satellite communications, the need for high-gain antennas is inevitable. Point-to-point communication links use antennas with very narrow beams, whereas satellites use antennas with excellent radiation characteristics, such as high gain, broadband, and wide-angle beam scanning, in order to provide coverage to a selected geographic area. These features also demand compact, synthesizable, and low-cost designs for the needed applications. Parabolic reflector and array antennas are examples of high-gain antennas that are widely used in radar, satellite and point-to-point communications [15]. These antennas have advantages because of low-cost and simple manufacturing. However, parabolic reflectors are bulky, which is undesirable for certain applications. Two desired features for this type of high-gain antenna are portability and easy deployablity in extreme and unfavorable temperature conditions. On the other hand, the array antennas come with major design complexity and high cost due to their amplifier modules and phase shifters. Reflectarray antennas have received considerable attention over the past few decades [16]. They combine some advantages of parabolic reflectors and phased arrays, which make reflectarrays suitable for various advanced applications. A trend from conventional parabolic reflector to printed flat reflectarray can be seen in Fig. 3.1.

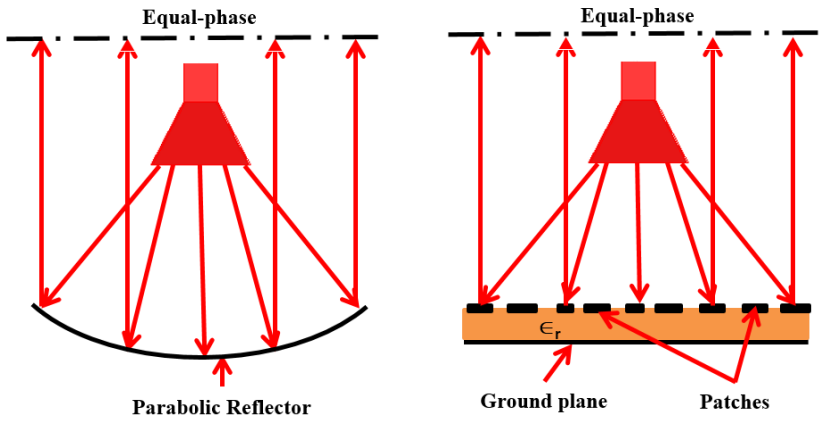

(a) (b)

Fig. 3.1. Design trends of reflectarray (RA) antenna (a) Parabolic reflector (b) Printed flat RA

Reflectarray antennas have been considered as a good candidate for efficient, directive, and beam scanning applications due to their advantage of combining reflectors and antenna arrays [16-20]. Berry et al. introduced the concept of reflectarray design using elements as waveguides [21]. Microstrip element-based reflectarray design was first experimented in 1978 [22]. As the technology of advanced microstrip-based reflectarray started to become popular in the 1990s as low profile [22], [23] and easily fabricated alternatives to conventional parabolic reflectors.

Basically, the reflectarray is an artificially engineered surface backed by a PEC sheet, which transforms the spherical wave emanating from a source tilted at angle θ with respect to the normal to the surface, to a beam directed at an angle, also normal to the surface, which typically points in the specular direction relative to the incident angle.

The legacy (conventional) approach [22] to designing the reflectarray is to print microstrip patches of different shapes, sizes and orientations on a dielectric substrate to

locally control the phase of the reflected wave when illuminated by an offset feed horn, which illuminates the surface as shown in Fig. 3.2.

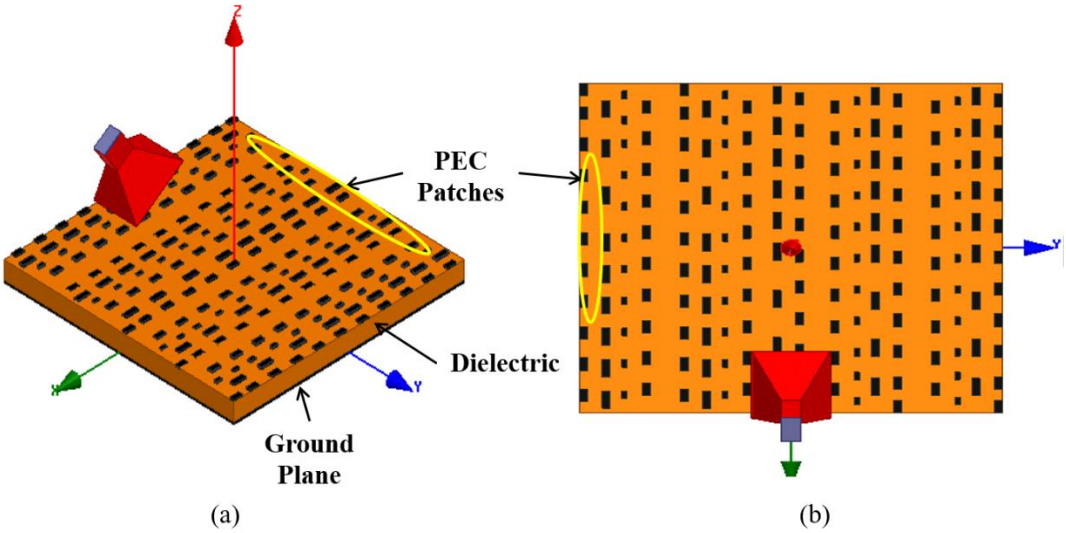

Fig. 3.2. (a) Isometric view (b) Top view of conventional design of reflectarray

In recent years, people have become more aware of the capabilities of 3D-printing technologies such as dielectric and metal-based printing referred to as additive and low-cost manufacturing. This technique eliminates many factors such as use of excessive and expensive machinery, as well as the use of adhesive material that is used to combine the dielectric layers and reduce the usage of unnecessary material.

In this chapter, we have discussed the dielectric-only reflectarray (DORA) design. This reflectarray design is realized by printing dielectric blocks on PEC ground plane. The proposed reflectarray design gives the linearly increasing gain variation compared to the bandwidth as typically reported in the literature (i.e., 10% for the designs based on the legacy approach).

3.2 DORA Design Using Dielectric Blocks (Metasurfaces)

Here, we introduce an alternate design that extends the DaD-based lens design procedure to the reflectarray problem. We invoke the image principle to show that the reflectarray design problem is equivalent to that of designing a graded index (GRIN) lens, which converts the spherical wave emanating from the feed horn to a collimated beam in the specular direction. Hence, we can readily adapt the design procedure described in the previous chapter of different flat lenses to design the reflectarray. If the feed is a prime-focus type, as opposed to offset, then the reflectarray is exactly similar to the lenses we have discussed in Section 2.2 of Chapter 2. For the offset case, the reflectarray is obviously no longer circularly symmetric. The isometric and top views of the reflectarray are shown in Fig. 3.3.

The design specifications chosen for the reflectarray are f (center frequency) = 15GHz; h_f (height of feed) = 144mm; θ (horn tilt angle) = 33° and ϕ = 180°; A_x & A_y (aperture size) = 210mm.

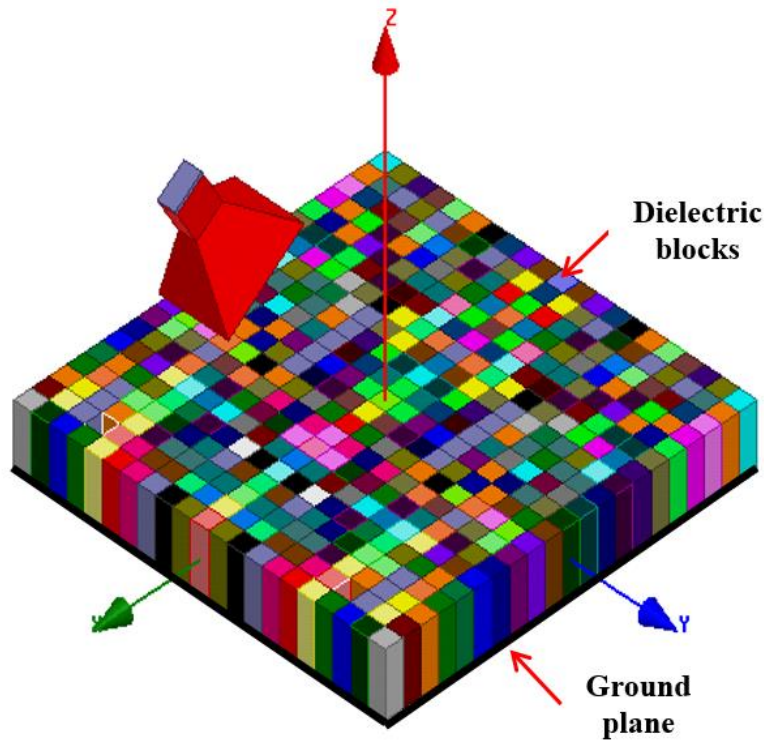

Fig. 3.3. Isometric view of proposed reflectarray design

The desired frequency band range is Ku-band (12-18GHz) and the center frequency chosen for our design was 15GHz. We assume that the feed horn illuminates the reflectarray surface with a tilted spherical wave at an angle of θ=33°. Next, we determine the phase distribution (ϕ_i) on the top surface of the reflectarray (input aperture) located at z = 15mm (see Fig. 3.4), when illuminated by the feed horn. We compute the desired phase distribution (ϕ_o) at the exit aperture plane (z = -15mm) that would generate a directed beam below the equivalent lens, also pointing at θ = 33°.

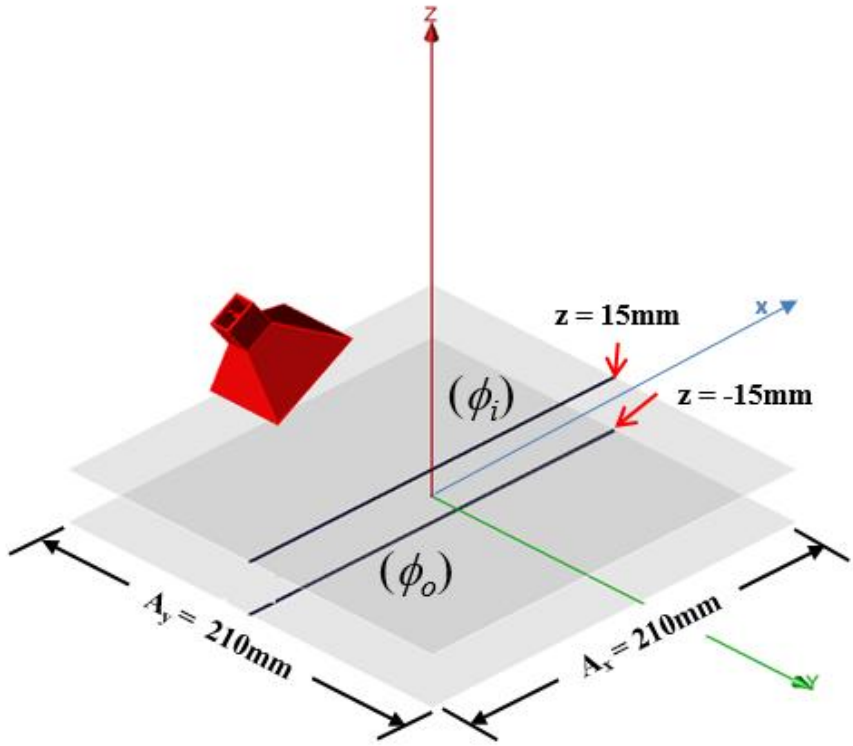

Fig. 3.4. Isometric view of the different aperture locations

Based on the phase distributions on the input, ϕ_i, and output, ϕ_o apertures as mentioned in Fig. 3.5., the phase difference (ϕ_o - ϕ_i) is taken and dielectric constants are found using the following:

$$\emptyset_o - \emptyset_i = \frac{2\pi}{\lambda} t\sqrt{\epsilon_{rj}} \tag{3.1}$$

where λ is free space wavelength, t is thickness of lens, and ϵ_{rj} is the dielectric constant of the jth block along the x-axis. The blocks (j) along the x-axis are numbered from 1 to 21 in Table 3.1, which are ϵ_r values of the equivalent lens.

In Fig. 3.6, we show the phase distribution at the exit aperture, ϕo, using the lens (dielectric blocks as shown in Fig. 3.7). We see that we are able to achieve the comparable

phase distribution using the dielectric blocks at the exit aperture (i.e., ϕ_o), with the desired phase distribution as shown in Fig. 3.5., using equation 3.1.

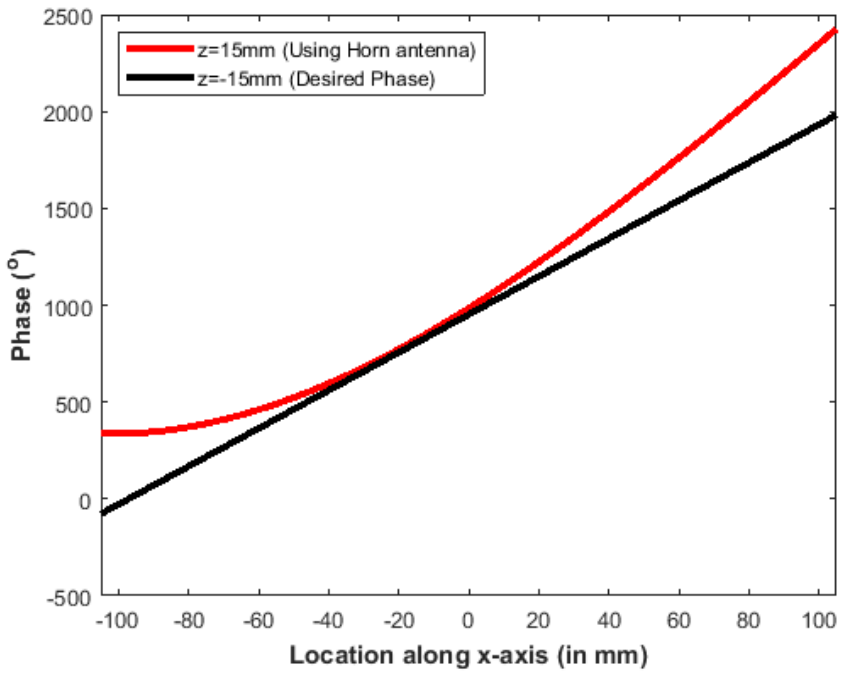

Fig. 3.5. Phase distribution on the different aperture locations

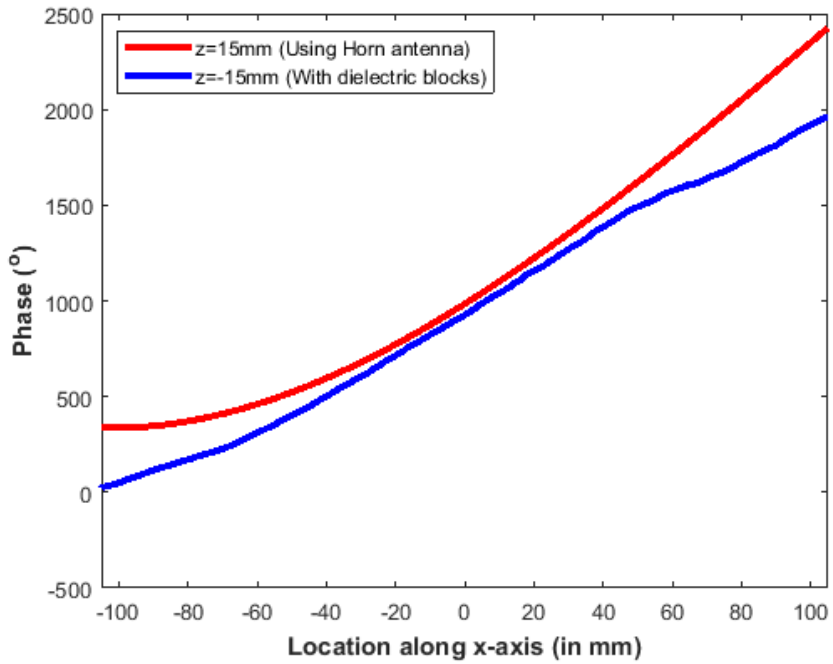

Fig. 3.6. Phase comparison on the different aperture locations with dielectric blocks

Table 3.1: Material parameters along the x-axis at y=0mm

Loc. Along x-axis (in mm)	-100	-90	-80	-70	-60	-50	-40	-30	-20	-10	0	10	20	30	40	50	60	70	80	90	100
$\in_r$	1.24	1.66	2.03	2.37	2.64	2.87	3.02	3.12	3.15	3.13	3.06	2.94	2.78	2.59	2.4	2.2	1.97	1.7	1.45	1.26	1.08

Similarly, the $\in_r$ values needed along the *x*-axis for different values of *y* are calculated, which are shown in Table 3.2. Here each dielectric block is of size 10mm × 10mm × 30mm and the final design has 21 × 21 blocks of dielectrics, as shown in Fig. 3.3.

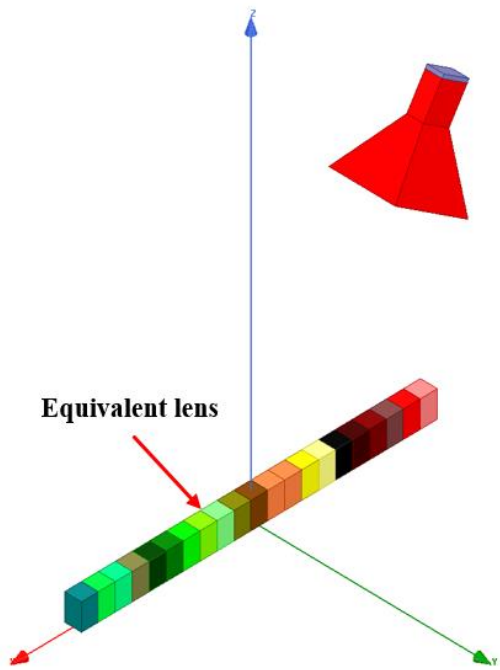

(a) Isometric view

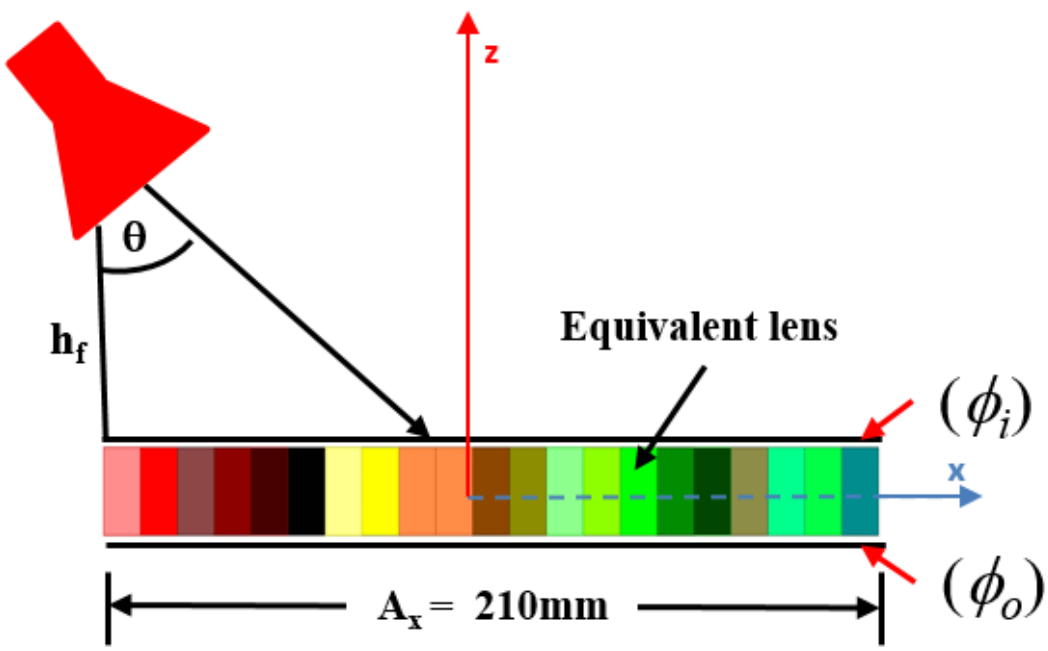

(b) Side view of proposed DORA by using image theory to derive an equivalent lens

Fig. 3.7. Proposed DORA

Table 3.2: Material parameters for the DORA

Y-axis (mm) / X-axis (mm)	0	10	20	30	40	50	60	70	80	90	100
-100	1.24	1.23	1.2	1.19	1.21	1.21	1.2	1.19	1.2	1.21	1.2
-90	1.66	1.64	1.6	1.59	1.61	1.6	1.58	1.59	1.62	1.62	1.66
-80	2.03	2.02	1.97	1.96	1.99	1.98	1.98	1.99	2.02	2.04	2.05
-70	2.37	2.36	2.32	2.31	2.32	2.33	2.34	2.37	2.43	2.44	2.49
-60	2.64	2.63	2.59	2.59	2.62	2.62	2.63	2.67	2.78	2.82	2.86
-50	2.87	2.86	2.82	2.82	2.85	2.85	2.88	2.94	3.07	3.13	3.2
-40	3.02	3.01	2.97	2.98	3.02	3.03	3.07	3.15	3.32	3.39	3.46
-30	3.12	3.12	3.08	3.08	3.12	3.13	3.19	3.28	3.49	3.6	3.7
-20	3.15	3.15	3.11	3.13	3.17	3.19	3.26	3.35	3.56	3.72	3.85
-10	3.13	3.12	3.09	3.12	3.17	3.19	3.28	3.37	3.62	3.83	3.95
0	3.06	3.05	3.02	3.04	3.11	3.14	3.22	3.34	3.63	3.82	3.98
10	2.94	2.94	2.91	2.94	3	3.04	3.13	3.28	3.5	3.8	3.99
20	2.78	2.79	2.77	2.8	2.87	2.9	3.01	3.12	3.43	3.71	3.94
30	2.59	2.6	2.58	2.62	2.7	2.77	2.87	2.99	3.29	3.56	3.79
40	2.4	2.41	2.39	2.44	2.53	2.57	2.67	2.83	3.1	3.37	3.67
50	2.2	2.18	2.19	2.24	2.33	2.36	2.47	2.57	2.87	3.09	3.48
60	1.97	1.96	1.96	2	2.1	2.15	2.24	2.36	2.67	2.87	3.29
70	1.7	1.7	1.7	1.74	1.82	1.87	2.01	2.14	2.44	2.69	3.08
80	1.45	1.48	1.48	1.52	1.61	1.66	1.8	1.95	2.23	2.48	2.9
90	1.26	1.25	1.27	1.32	1.39	1.48	1.6	1.76	2.05	2.28	2.59
100	1.08	1.1	1.1	1.14	1.23	1.31	1.41	1.57	1.77	2.07	2.3

The design that utilizes the top half of the designed lens, backed by a PEC plane, was simulated by using Ansys HFSS; the normalized radiation pattern of the reflectarray was compared with the pattern for the case when the dielectric was removed.

3.3 Results

Fig. 3.8 shows the patterns that demonstrate the effectiveness of the reflectarray design we have presented in improving the gain of the base horn alone. We also see the radiation

pattern of different reflectarrays, namely WO dielectric (ground plane only) and DORA in Fig. 3.9, where beam pointing in θ=0°; ϕ=0°.

We can also see the gain comparison of the above different reflectarrays in Fig. 3.10, where we can see the gain improvement of +4dB using DORA design over the entire frequency band (i.e., Ku-band).

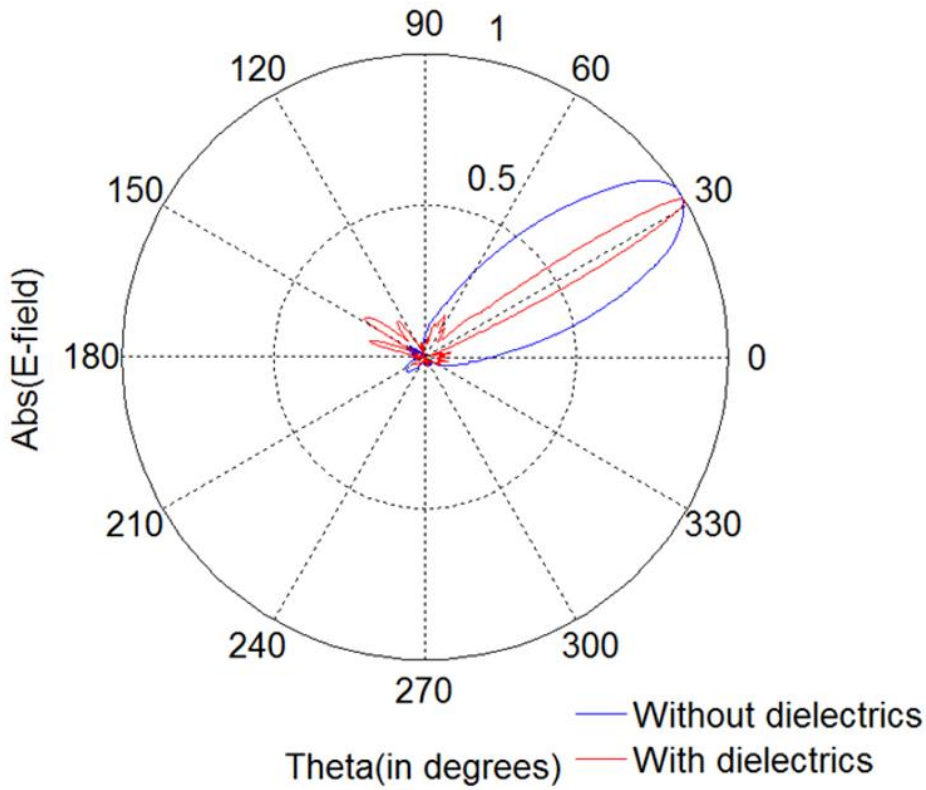

Fig. 3.8. Comparison of radiation patterns of reflectarrays

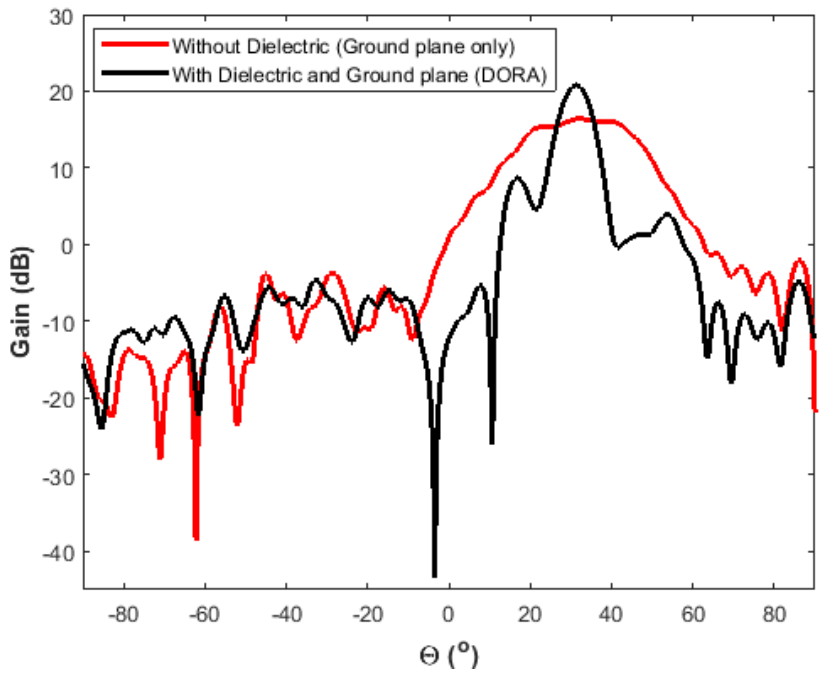

Fig. 3.9. Radiation patterns of the different reflectarrays at f_c=15GHz

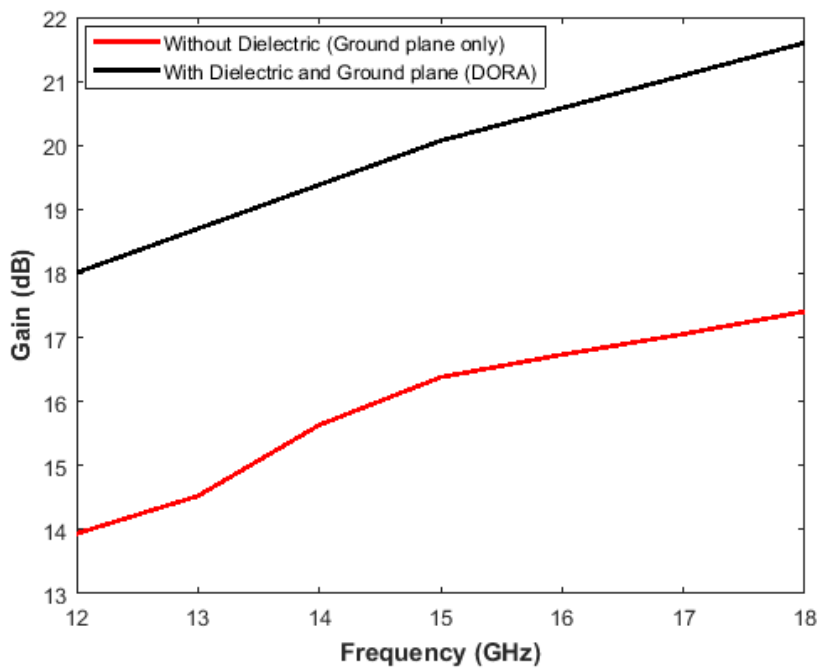

Fig. 3.10. Gain comparison of the different reflectarrays

3.4 Conclusions

In this chapter, we have shown the DORA design that uses the lens design approach (i.e., dielectric blocks) as discussed in the earlier chapter on flat lens design. These dielectric materials are arranged in the manner to point the beam in the specular direction (i.e., θ=33°; ϕ=0°). The proposed DORA design gives the linearly increasing gain variation compared to the bandwidth as typically reported in the literature (i.e., 10% for the designs based on a conventional approach).

Chapter 4

Flat Lens Design Using Space-Qualifiable Multilayer Frequency Selective Surfaces (FSSs)

4.1 Introduction

Recently, considerable efforts have been made to develop long-haul RF communications systems, which require RF components such as reflectors and lenses that have unprecedented capabilities in manipulating electromagnetic fields efficiently using artificially engineered materials for microwaves, millimeter waves, and Terahertz frequencies. Important performance considerations for the design of the above components include gain, bandwidth, low profile, low cost, and easy deployability in extreme and adverse environmental conditions, especially for space applications.

Conventional high-gain antennas (e.g., planar lens antennas) exhibit the benefit of mitigating aperture blockage by the source and supporting rods, which also helps to achieve low cross-polarization levels. Dielectric-substrate-based lenses mitigate some of these limitations, but they are generally bulky and heavy because they rely on the spatially dependent phase accumulation introduced by geometric shaping of lens materials with sufficient thickness and dielectric-constant contrast to that of air. Printed flat lenses have also been proposed as substitutes for their dielectric counterparts [34]. Microwave lens antennas have also been demonstrated using arrays of constrained patch antennas [35], [36], where the required phase retardations were obtained by controlling the lengths of microstrips that connect the patches from one end to the other end of the lens.

However, due to the resonant feature of the patch, the operational bandwidths of these lens antennas are narrowband in nature. A variety of methodologies have been proposed by researchers to design flat lenses. These are based on traditional ray optics, transformation electromagnetics or field transformation techniques [37], among others. More recently, there have been several studies on low-profile printed lenses utilizing FSSs [39], and on flat lens designs based on the use of artificially engineered materials to achieve the requisite material parameters [40]–[43].

In this chapter, we describe a systematic procedure for realizing the requisite radially varying phase shifts, by using locally periodic multilayer FSSs to realize a lightweight, low-profile and low-cost design. We also carry out a performance study of the proposed FSS-based lens as shown in Fig. 4.1(b) and compare its gain behavior and frequency response characteristics with those of a lens designed by using the traditional ray optics (RO) method shown in Fig. 4.1(a) to demonstrate the efficacy of the proposed approach.

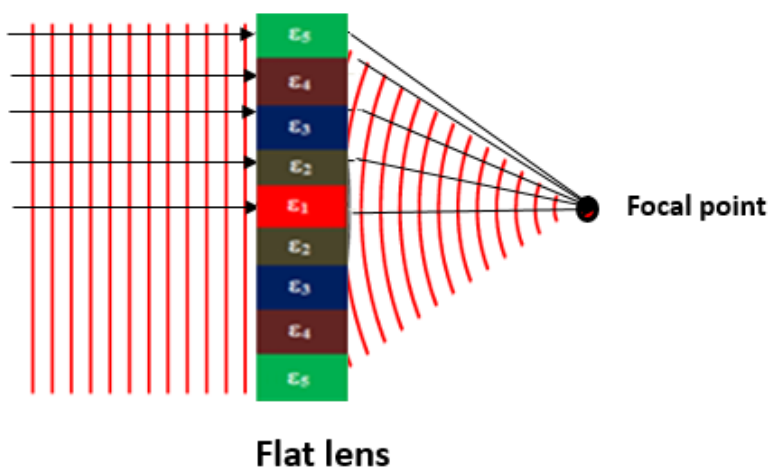

(a)

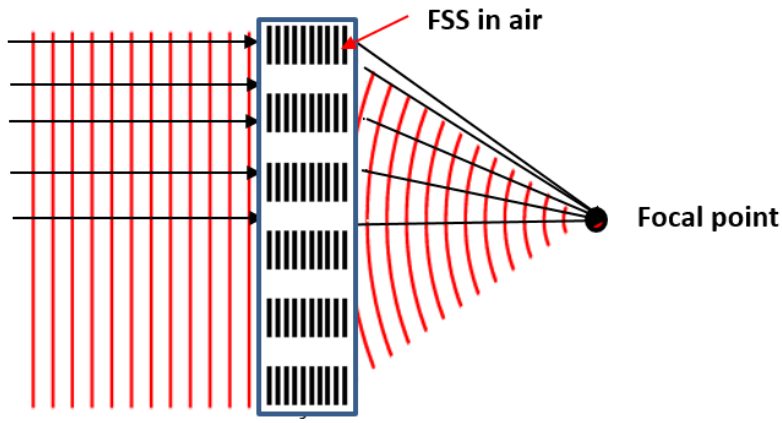

(b)

Fig. 4.1. (a) RO-based flat lens (b) FSS-based flat lens

4.2 Traditional Ray Optics (RO) Lens Design

To effectively carry out a comparison of the performance characteristics of the FSS-based lens design to those of the traditional RO-based flat lens, we proceed to design the traditional RO-based flat lens by using the methodology described in [37]. Fig. 4.2 and 4.3 shows the geometry of the RO-based flat lens. The specifications for the lens are (i) required gain, (ii) center frequency f=30GHz, (iii) focal length F=60mm, and (iv) thickness h=10mm. The diameter D of the lens is chosen to be 80mm on the basis of the gain requirements, and the level of discretization of the dielectric parameters is defined along the radial direction, which determines the number of rings. Here, we have used 10 discrete rings for the lens design, each with a radial width of 4mm, in order to facilitate a later comparison of its performance with that of the FSS-based flat lens design. The dielectric parameters are chosen to satisfy the path length conditions of these rings and are shown in Table 4.1. However, it is useful to model the traditional RO lens because it serves as a

benchmark for the multilayer FSS-based lens design that is carried out in the following sections.

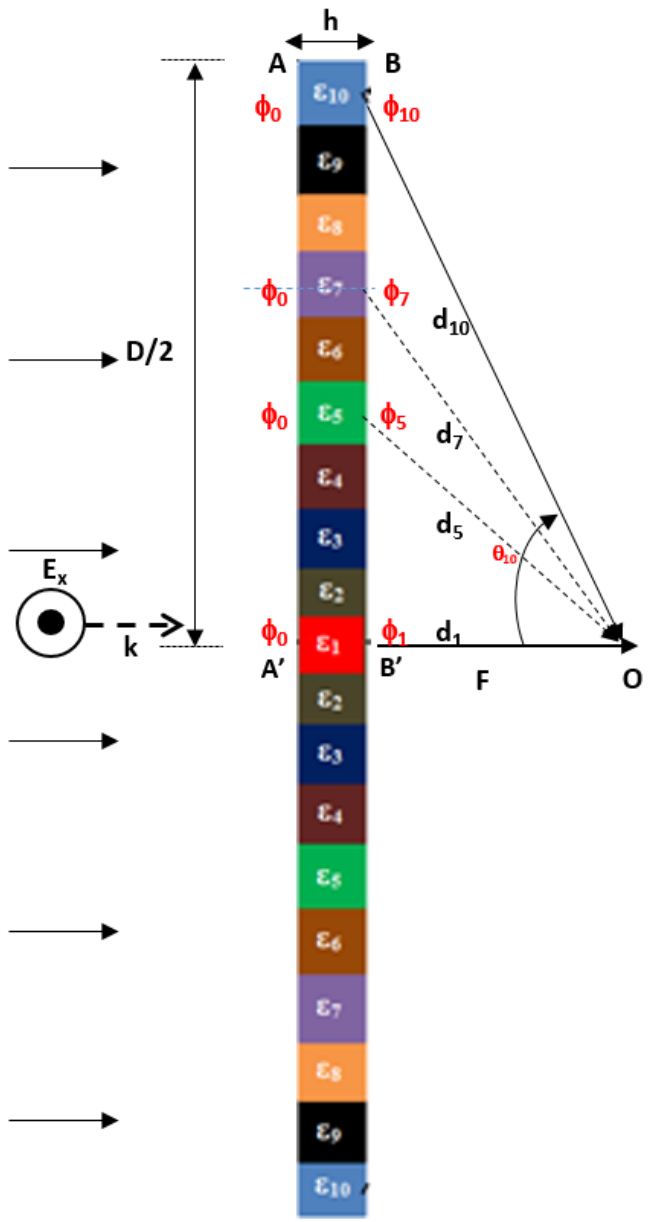

Fig. 4.2. Geometry of the traditional RO lens

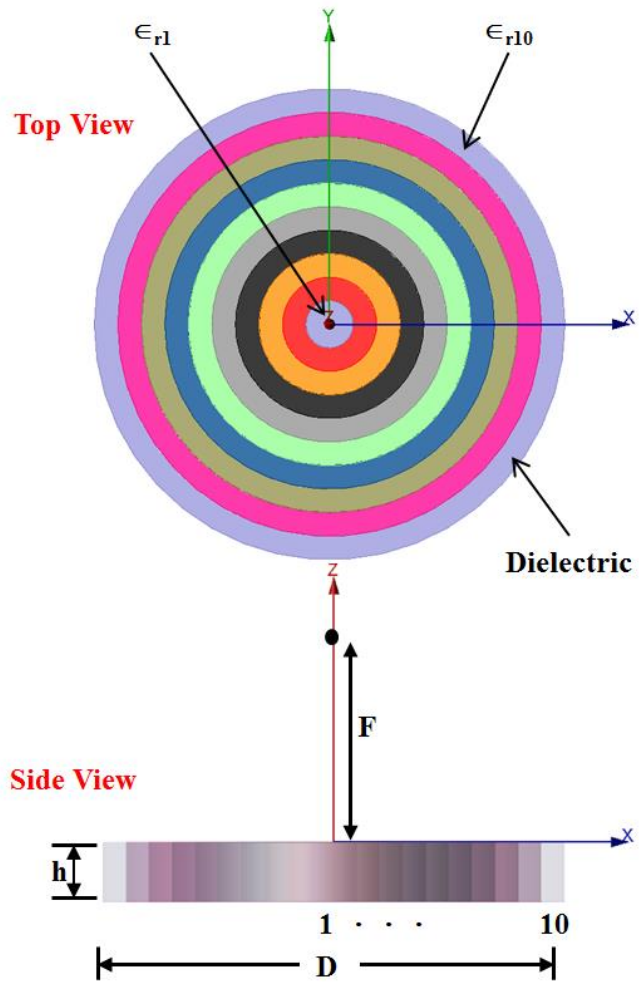

Fig. 4.3. Top view and side view of the traditional RO lens

Table 4.1: Material parameters of traditional RO lens

Ring No.	1	2	3	4	5	6	7	8	9	10
∈	4.40	4.28	4.08	3.78	3.42	2.99	2.52	2.04	1.57	1.12

4.3 Technical Approach for the Multilayer FSS Lens Design

We employ a novel technique for designing the flat lens based on the multilayer FSS technique to achieve the desired phase behavior needed in the exit aperture of the planar lens without unduly compromising the magnitude of S_{21}. We tweak the dimension and spacing between the multilayer FSS screen accordingly and use square patches as an example (other shapes can be used as well), such that the goal of the desired phase behavior can be achieved. The novelty of this method is that the square patches are of subwavelength sizes and do not rely on resonance properties of patches, which is the key to realizing a wideband low-loss design.

We start out with the desired phase distribution in the exit aperture of the traditional RO lens design, which is the design goal for the phase behavior of the proposed FSS-based lens design as illustrated in Fig. 4.4.

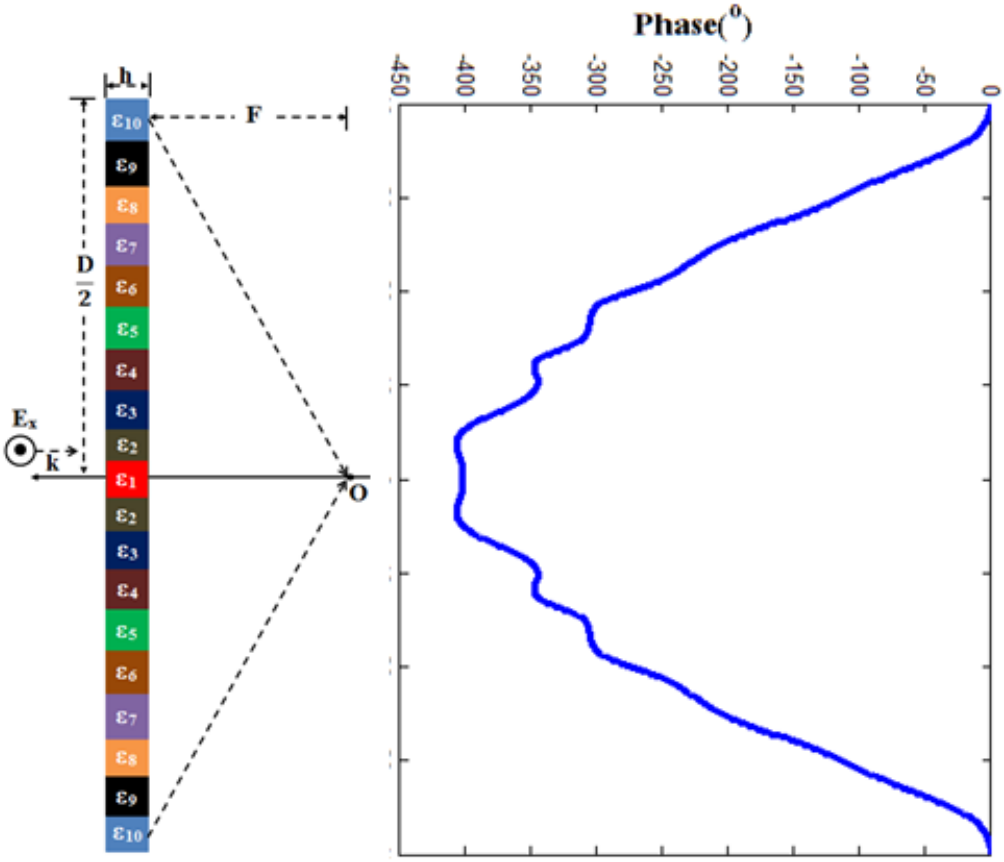

Fig. 4.4. RO lens and its phase distribution along the diameter of the exit aperture

After determining the required phase behavior at exit aperture of the RO lens design, we developed the following design strategy to achieve the desired phase delays.

(i) We began by selecting the subwavelength size square patch element (<λ/10) for the FSS unit cell shown in Fig. 4.5.

(ii) We computed the desired phase distribution in the exit aperture of the RO lens design, which is the design goal for the phase behavior of the proposed FSS-based lens design.

(iii) It became evident during the above study that it is not possible to obtain the desired

phase-shift range by using a single FSS screen, which prompted us to use multilayer FSS screens to achieve the desired phase shifts covering the range of 0 to 360° without unduly compromising the S_{21} magnitude.

(iv) The dimensions ‘a’ and spacing‘d’ of the patches were chosen such that the local S_{21} phases of the FSSs match those of the each of the dielectric rings in the RO design.

To carry out the simulation, the particular ring is discretized in the unit cell of appropriate periodicity (*b*). The periodicities were chosen to be on the order of $\lambda/10$, far away from the resonance of the structure comprising the unit cell, in order to achieve wide-band performances. Here, a plane-wave source is placed below the multilayer square patches, in Port-1, along with the periodic boundary conditions in the EM simulator HFSS. In Figure 4.5, h is the overall thickness of the multilayer-FSS elements (i.e., square patches), ‘a’ is the patch dimension and b=1mm.

It is worth pointing out that this approach does not rely on the resonance properties of the patches to realize the artificial dielectrics; hence, it bypasses the problems of high losses and narrow bandwidths suffered by materials synthesized by using some of the other techniques mentioned in [35] and [42], for instance.

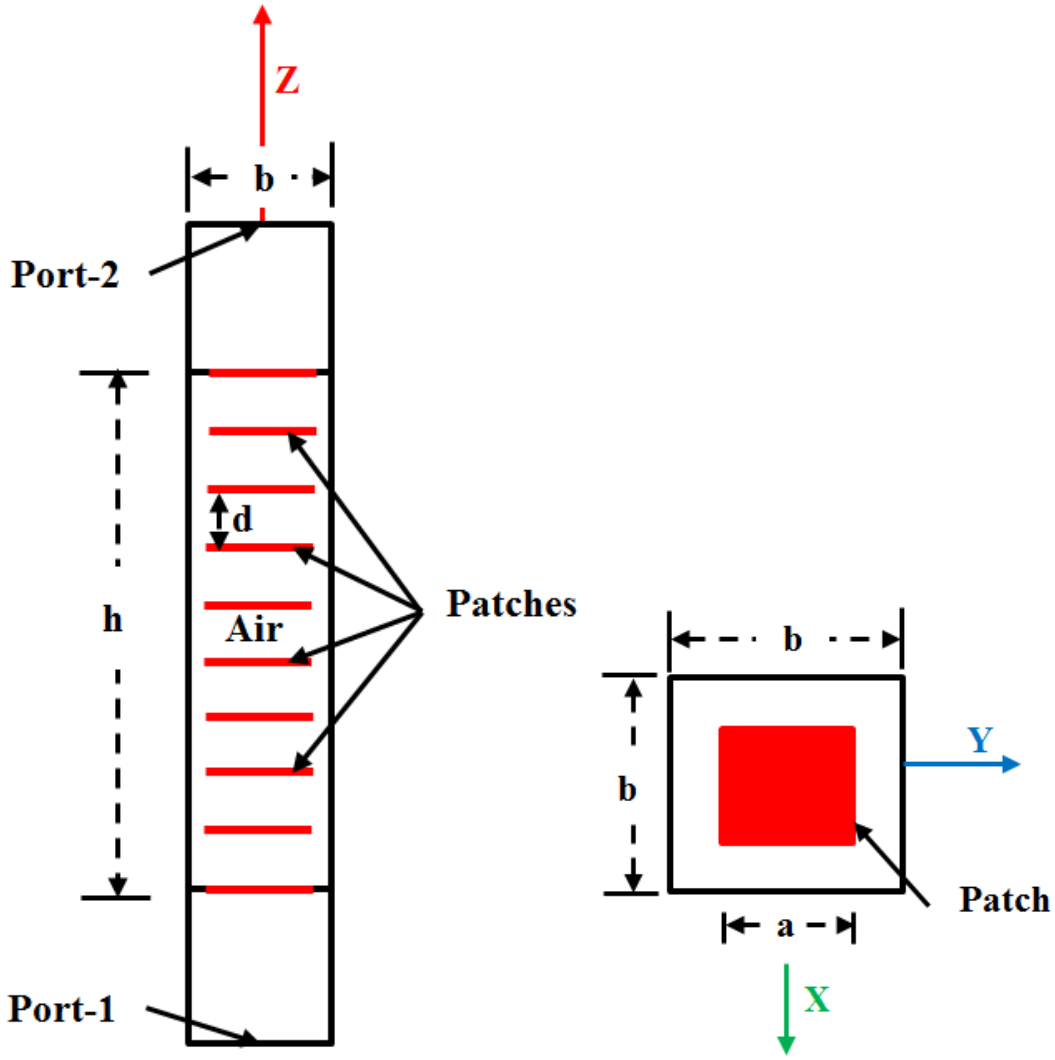

(a) (b)

Fig. 4.5. (a) Side view; (b) Top view; Unit cell for achieving phase delays for multilayer-FSS lens

4.4 Performance Comparison of RO-Based Lens with Multilayer-FSS-Based Planar Lens Design

For the FSS-based planar lens design, we start with a square patch element in free space as the FSS unit cell, which in view of its symmetry, can not only support orthogonal polarizations of the incident field, but circular polarization (CP) incidence as well. Next, we use the methodology as mentioned in Sec. 4.3. We start by selecting the local unit cells for the rings to be 1*mm* x 1*mm* x 10*mm*, for which the desired phase delays has to be calculated as per the design goal shown in Fig. 4.4. Design parameters for the unit cell as shown in Fig. 4.5(b) are chosen to be b=1mm, t=10mm. The detail of the design procedure is illustrated in Fig. 4.6. It shows that the lens is composed of locally periodic multilayer FSS cells of square patches with a total thickness of ‘h’. The local patch dimension is ‘a’ and the spacing between the patches is ‘d’. These parameters are adjusted to achieve the desired phase shift behavior of the dielectric rings in the RO design without compromising the S_{21} magnitude.

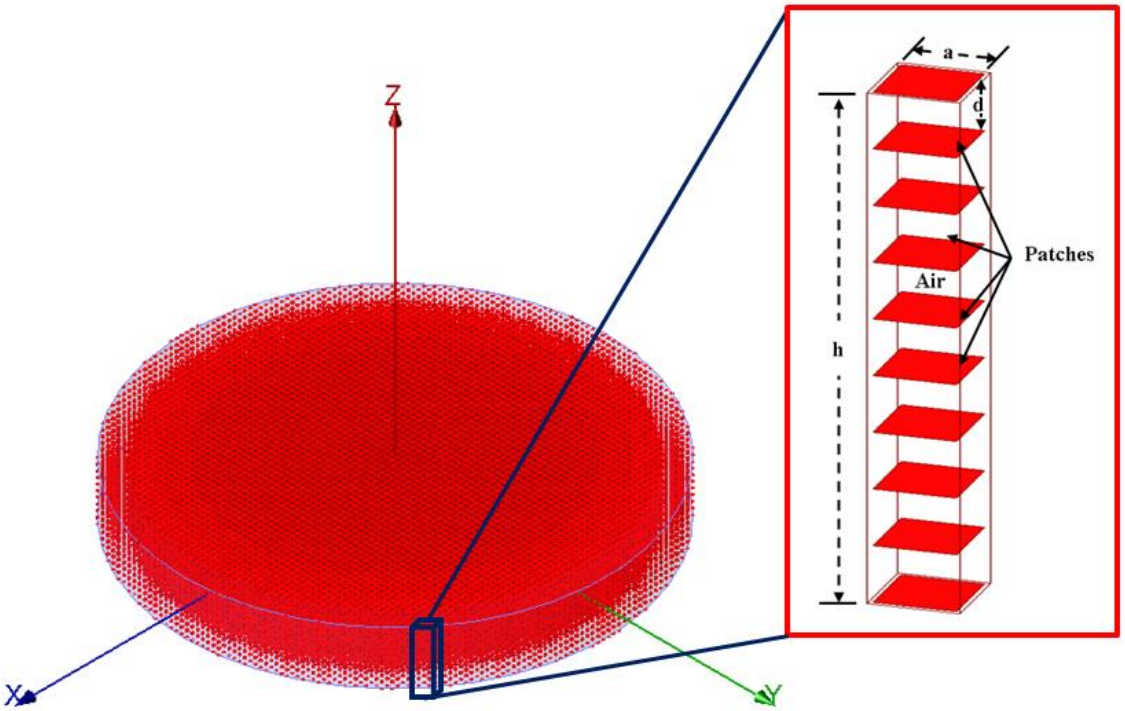

Fig. 4.6. Design strategy for FSS-based planar lens

It is important to point out that the FSS-based planar lens design is carried out by taking advantage of the "locally periodic" property of the design, which enables us to impose the periodic boundary conditions to a unit cell to reduce the original problem to a manageable size, substantially reducing the computational burden in the process by using the EM simulator Ansys HFSS.

In Figs. 4.7, 4.8, 4.9 and 4.10, we show the validation of the phase delays of S_{21} using the design strategy mentioned in Sec.4.3 by comparing the desired phase delays of the traditional RO lens as well as FSS-based planar lens design approach for a few rings as an example for the multilayer-FSS lens design. We can see from the S_{21} phase plots as shown in Figs. 4.7(b), 4.8(b), 4.9(b) and 4.10(b) that there is a close agreement between the desired

phase shifts and FSS-based approach, which means that we are able to realize the desired phase behavior using the design strategy as mentioned in Sec 4.3. Next, we move towards the final multilayer-FSS lens design where we use the square patches arranged in a Cartesian grid as shown in Fig. 4.11.

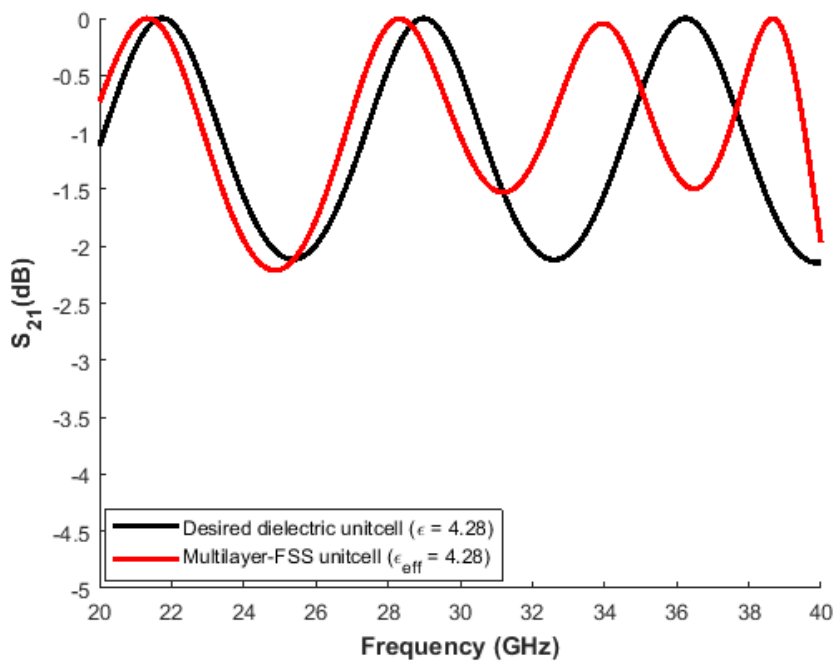

(a)

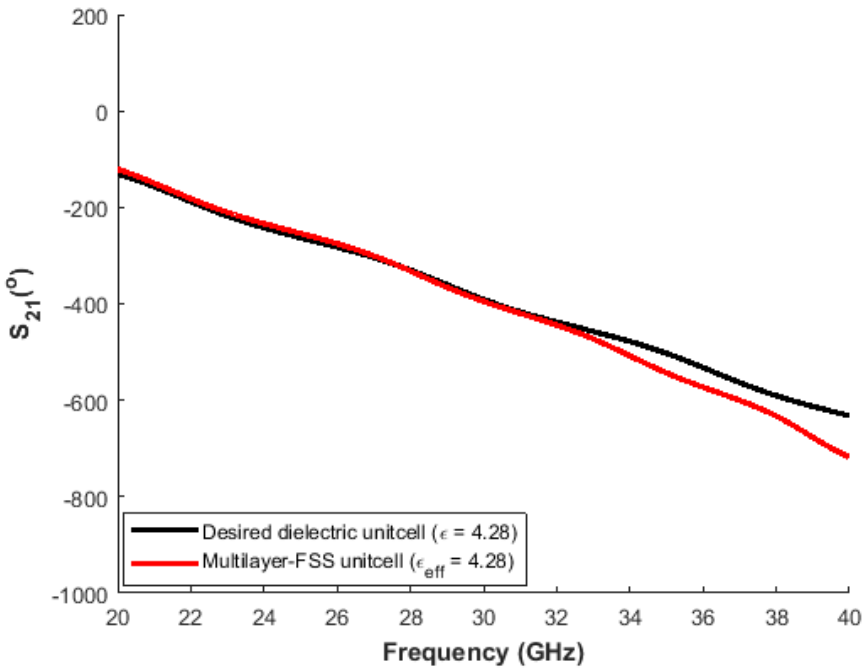

(b)

Fig. 4.7. S_{21} parameters of unit cells for ring no. 2 (a) S_{21} magnitude (b) S_{21} phase

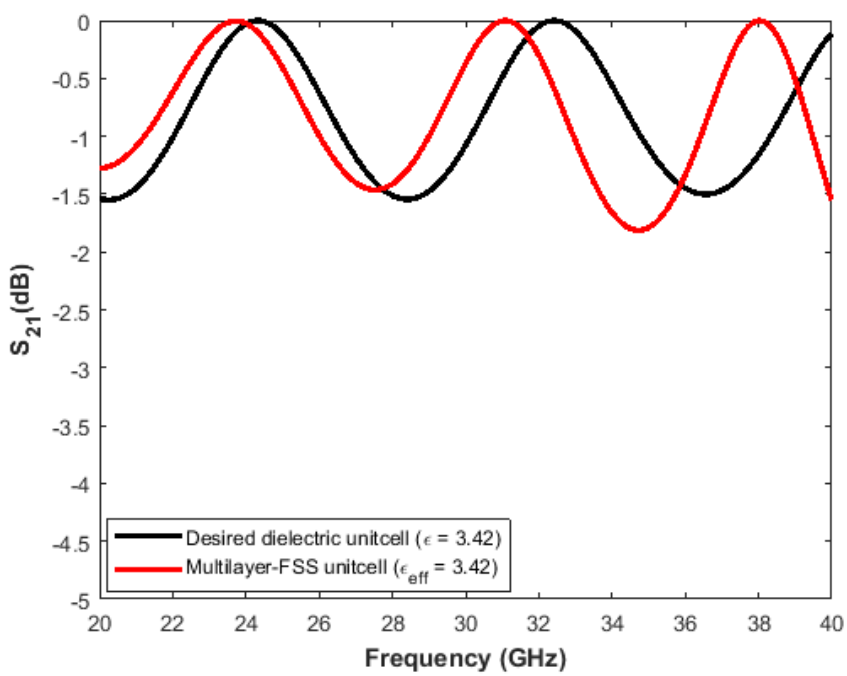

(a)

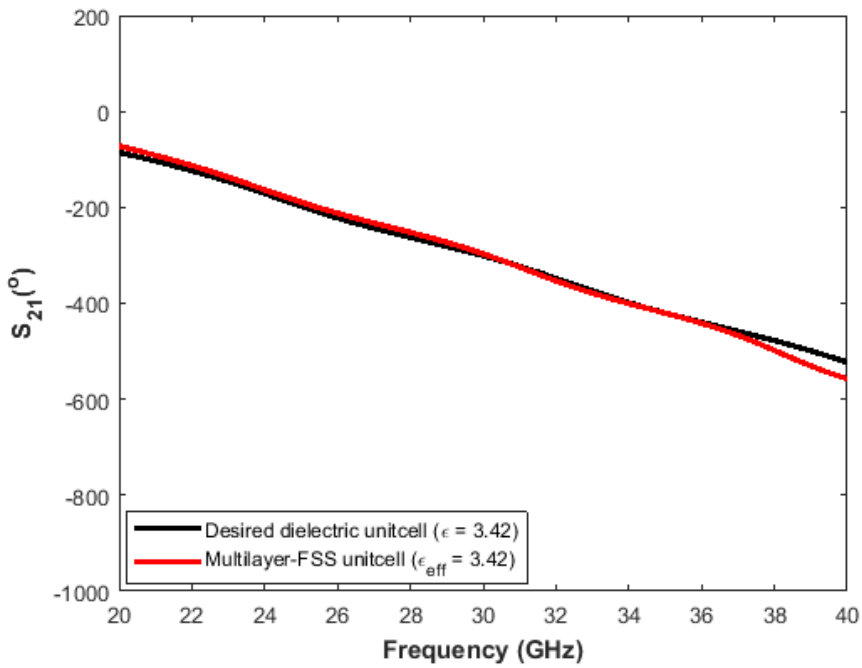

(b)

Fig. 4.8. S_{21} parameters of unit cells for ring no. 5 (a) S_{21} magnitude (b) S_{21} phase

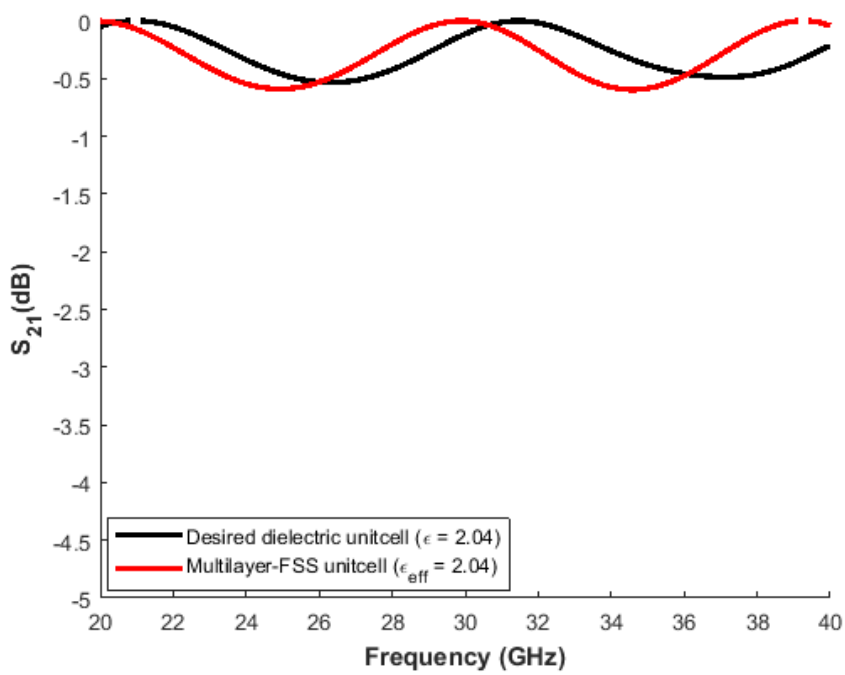

(a)

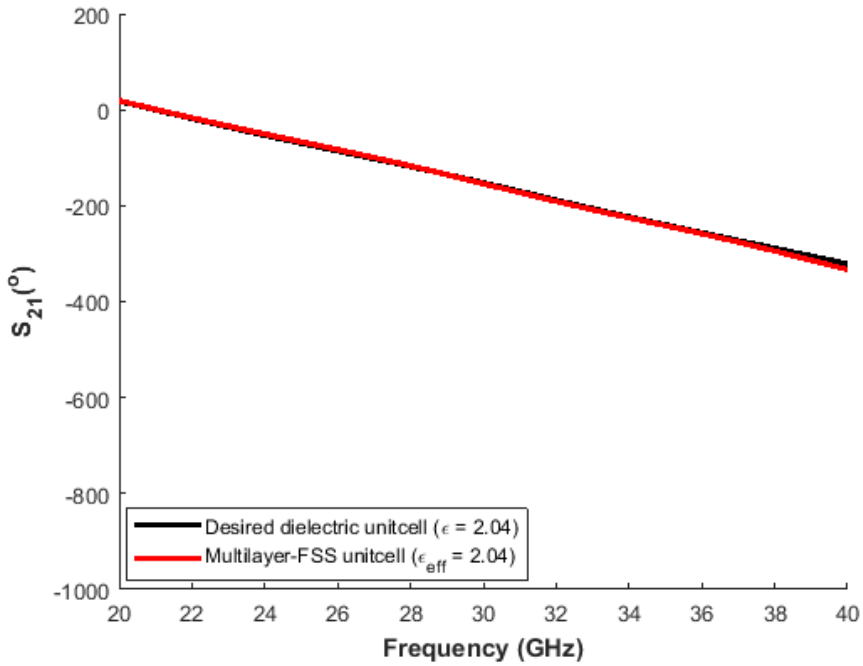

(b)

Fig. 4.9. S_{21} parameters of unit cells for ring no. 8 (a) S_{21} magnitude (b) S_{21} phase

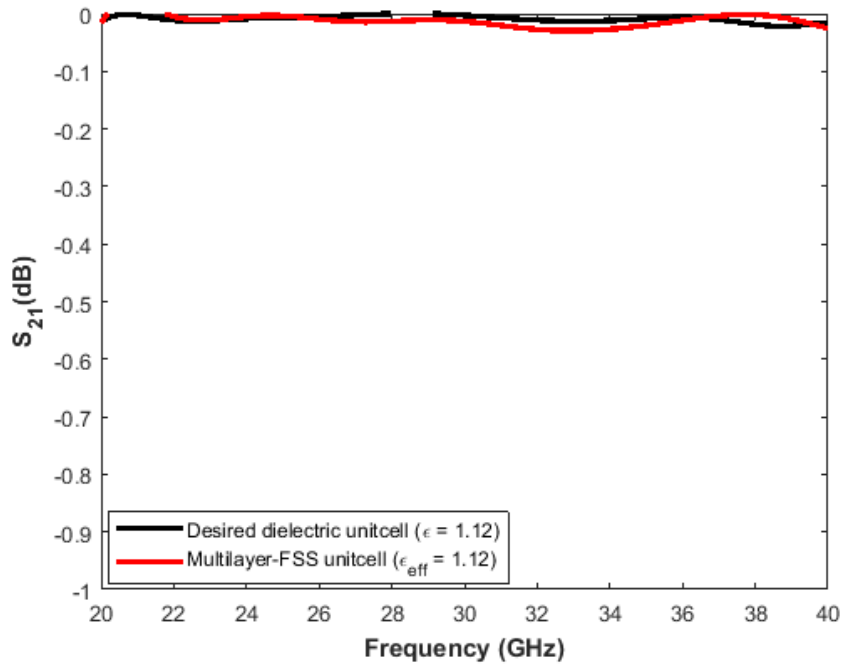

(a)

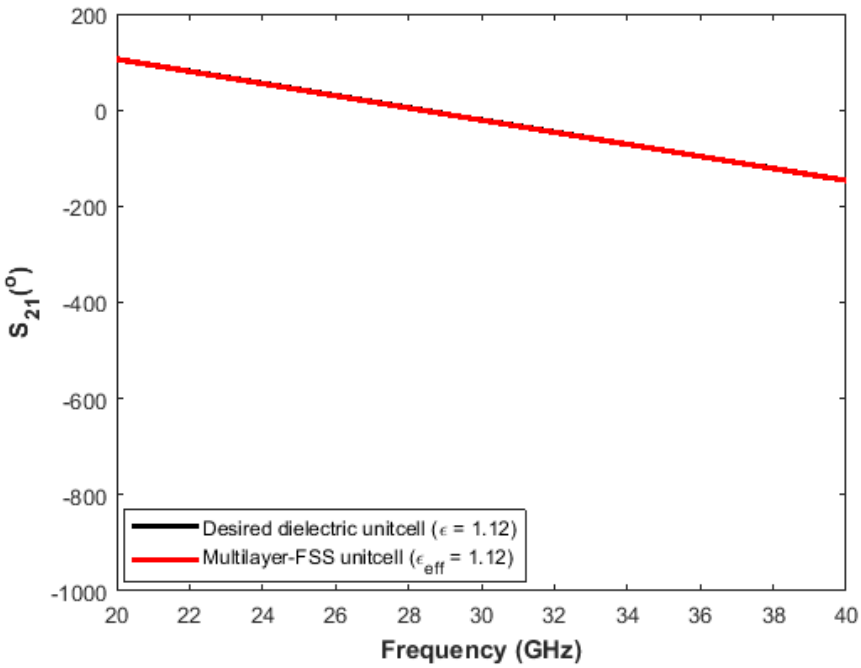

(b)

Fig. 4.10. S_{21} parameters of unit cells for ring no. 10 (a) S_{21} magnitude (b) S_{21} phase

4.5 Comparison of RO- and FSS-Based Planar Lens

We have carried out the FSS-based planar lens design as shown in Figs. 4.6 and 4.11, whose parameters are given in Table 4.2.

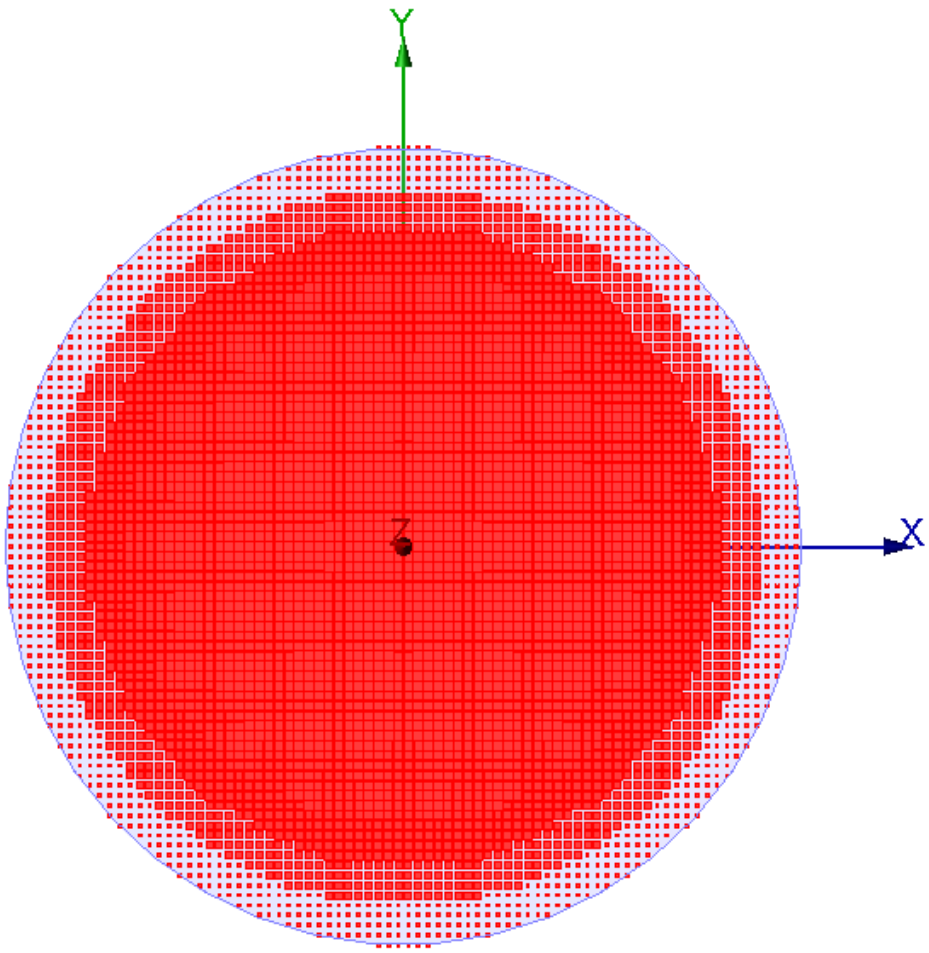

Fig. 4.11. Top view of proposed multilayer-FSS planar lens

Table 4.2: Parameters of FSS-based planar lens

Ring No.	1	2	3	4	5	6	7	8	9	10
ϵ_{eff}	4.40	4.28	4.08	3.78	3.42	2.99	2.52	2.04	1.57	1.12
Patch size 'a' (in mm)	0.983 (λ/10.2)	0.980	0.979	0.970	0.965	0.950	0.920	0.860	0.740	0.450 (λ/22)

The gain performances of the different planar lenses, viz, the RO lens and the multilayer-FSS lens using square patches, are shown in Fig. 4.12.

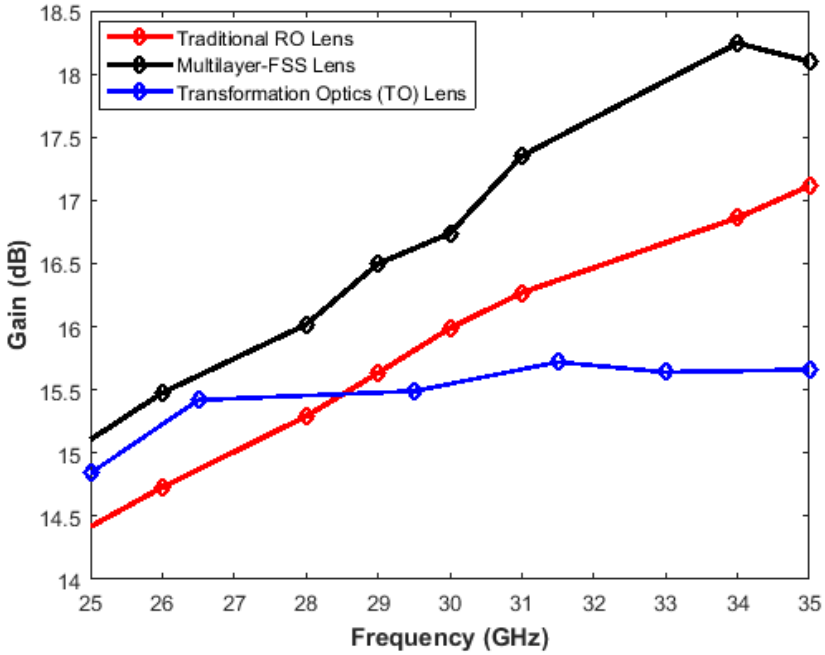

Fig. 4.12. Gain comparison of different planar lenses

We see that the FSS-based planar lens performs well in the desired frequency range (i.e., 25–35GHz); in fact, it is 0.85dB higher, on average, and provides a performance superior to the traditional RO lens over a wide band, for which dielectric materials are typically unavailable. It is also seen that the FSS-based lens also performs better than the similar lens designed by using transformation optics (TO) [45].

4.6 Conclusions

In this chapter, we have presented a new design of flat lens, which utilizes multilayer frequency selective surfaces (FSSs) in *free space.* The lens can be space-qualified since, unlike conventional designs for lenses, it does not need to use dielectric materials. We have also demonstrated a systematic procedure for realizing the requisite radially varying phase

shifts, by using locally periodic multilayer FSSs to realize a lightweight, low-profile and low-cost design.

Chapter 5

Low-Cost Phase Shifter Design for Beam-Scanning Antennas

5.1 Introduction

Phased array antennas are widely used for beam scanning applications in communication systems. It is well known that conventional phase shifters utilized in these applications are lossy, bulky and costly. Our objective in this work is to investigate low-cost phase shifters that could help mitigate these problems.

Extensive research has been carried out in recent years for designing phased array antennas, especially in the context of satellite communication applications, and the design of civilian radar-based sensors. A number of different approaches have been proposed for scanning the beams of phased array antennas for these applications. Most of these approaches call for biasing configurations that are needed, either for activating certain switches (e.g., pin diodes or varactor diodes [46]), or for modifying the electrical properties of materials [47], in order to realize the desired phase-shift when integrated with the antenna elements of the array. Fig. 5.1 shows some typical examples of such devices that are commonly used for this purpose. They introduce step-wise phase shifts in the fields radiated by the antenna elements to realize beam scanning by the array.

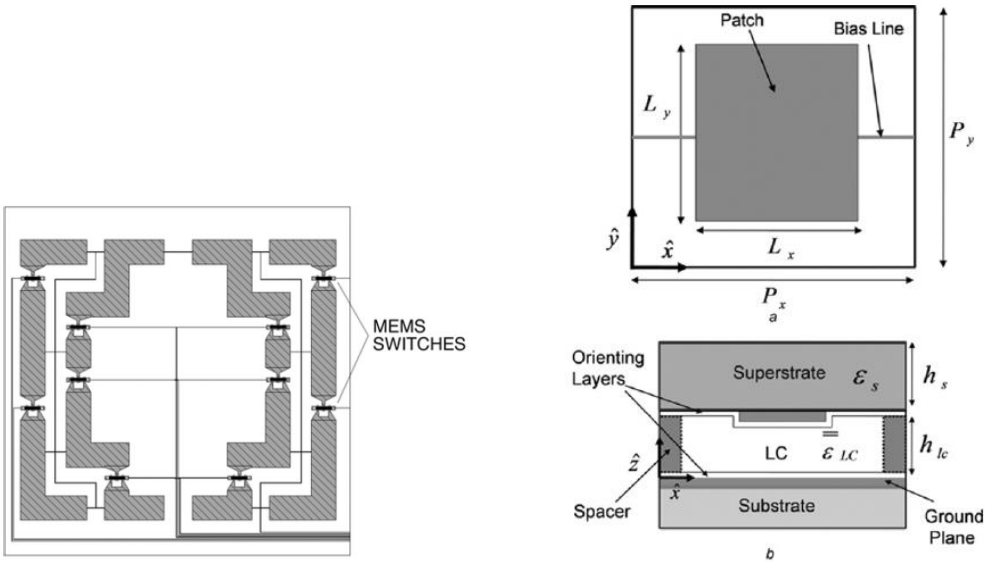

(a) (b)

Fig. 5.1. Examples of phase-shifting configurations: (a) Switch-based, (b) Liquid crystal-based

The goal of this research is to develop low-cost, variable phase shifters for the antenna elements of a scanning array. We propose an approach that realizes the desired phase shift in the array by using a combination of two steps. In the first of these, stepwise increments of 45° of phase shift are realized by inserting switches or other phase shifting devices in the "feed line," as opposed to in the radiating element. Next, a fine tuning of the phase of the field radiated by the antenna element is carried out by using variable phase shifters in the range of 0° to 45°, by implementing them in the antenna elements, using a technique described below. By combining the stepwise phase shifts in the feed lines, with the variable ones in the antenna element, we can realize a continuously varying phase shift in the range of 0° to 360° in the field radiated by each antenna element, which is our desired design goal.

5.2 Design Strategy for Phase-Shifter Design

Our strategy in this effort is to develop a variable phase shifter, with a phase range of 0° to 45°, which is based on the use of metasurface-based superstrates, and which we choose to be a truncated periodic structure. The superstrate is placed above the antenna element to introduce the desired phase shift in the wave traversing through it.

The first step in the design of low-cost metasurface-based variable phase shifters is to attempt to realize up to a maximum phase shift of S_{21} on the order of 45°, at the center frequency f=30GHz, for instance, when a unit cell of the superstrate is illuminated by a *plane wave* (see Fig. 5.2).

It is worthwhile mentioning at this point that initially we had set a design goal of the magnitude of S_{21} to be 0.5 dB, in order to ensure that the introduction of the superstrate above the antenna element would not compromise the gain of the element by more than the insertion loss of 0.5 dB. However, it was discovered later that such a restriction on the magnitude of $\mathbf{S}_{21}$ is unnecessary, since there is no clear and/or direct relationship between the insertion loss values of the superstrate derived by illuminating it by a plane wave source, and by an antenna element radiating from below the superstrate. In fact, it was found that the plane-wave insertion loss of the superstrate unit cell may even translate into relative *gain* when the superstrate is incorporated in the antenna element, because the physics of the radiation mechanism are very different in the two cases. For this reason, the restriction on the insertion loss of S_{21} for the *plane wave* case was removed, and we chose to work only with the gain performance of the *antenna element* in the presence of the superstrate. Consequently, the phase shift realized by the introduction of the superstrate

was determined independently for the antenna case in the design process, and the S_{21} of the plane wave case was only used as a guideline.

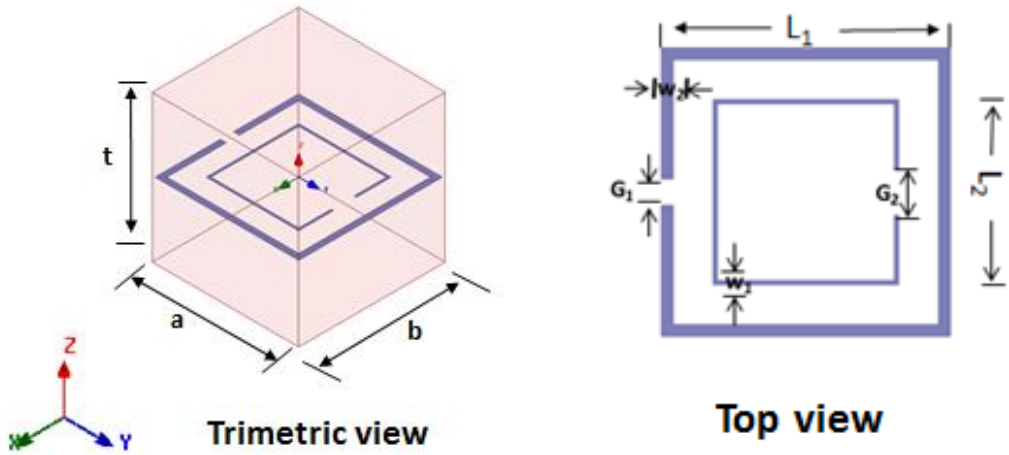

(a) (b)

Fig. 5.2. Unit-cell of metasurface-based phase shifter comprising (a) Trimetric view; (b) Top view

Our next step was to carry out the simulation of the unit cell by using a plane-wave source placed below the superstrate, in Port-1, along with the periodic boundary conditions in the EM simulator HFSS. The periodicities '*a*' & '*b*' of the unit cell were chosen to be equal, and on the order of λ/10, far away from the resonance of the structure comprising the unit cell, in order to ensure that the design would be relatively wideband.

Next, we optimize the parameters of the metasurface-based truncated periodic structure, comprised of nested square split rings, with the goal of achieving a S_{21} phase shift of 45°. We orientate the periodic structure along different planes, namely x-y, y-z and x-z, as shown in Fig. 5.3, and measure the magnitude as well as phase of S_{21} in the output port above the unit cell (i.e., in Port-2). The parameters of the element simulated are listed

in Table 5.1. Fig. 5.4 shows the S_{21} behavior of the of the unit cell of the superstrate under investigation.

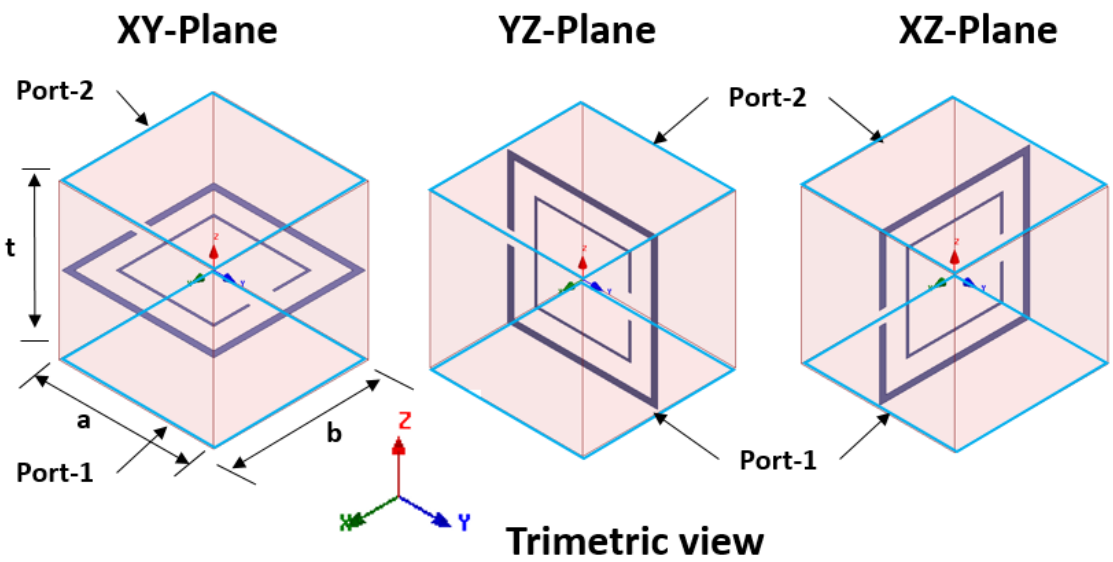

(a) (b) (c)

Fig. 5.3. Unit cell of the superstrate comprising nested square split rings: (a) xy-plane; (b) yz-plane; and (c) xz-plane

Table 5.1: Dimensions of metasurface-based phase-shifting element

L_1 (mm)	L_2 (mm)	W_1 (mm)	W_2 (mm)	G_1 (mm)	G_2 (mm)
0.98	0.63	0.03	0.08	0.09	0.16

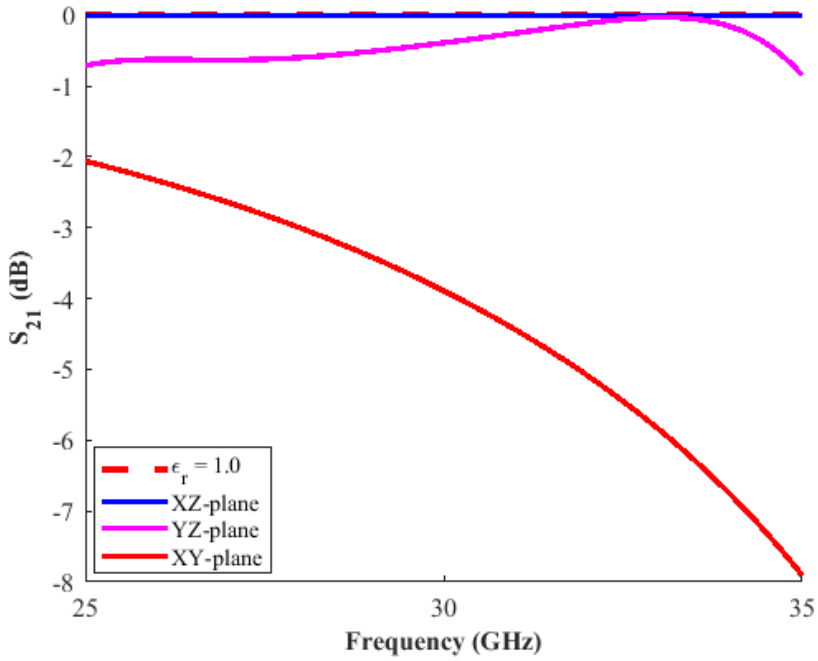

(a)

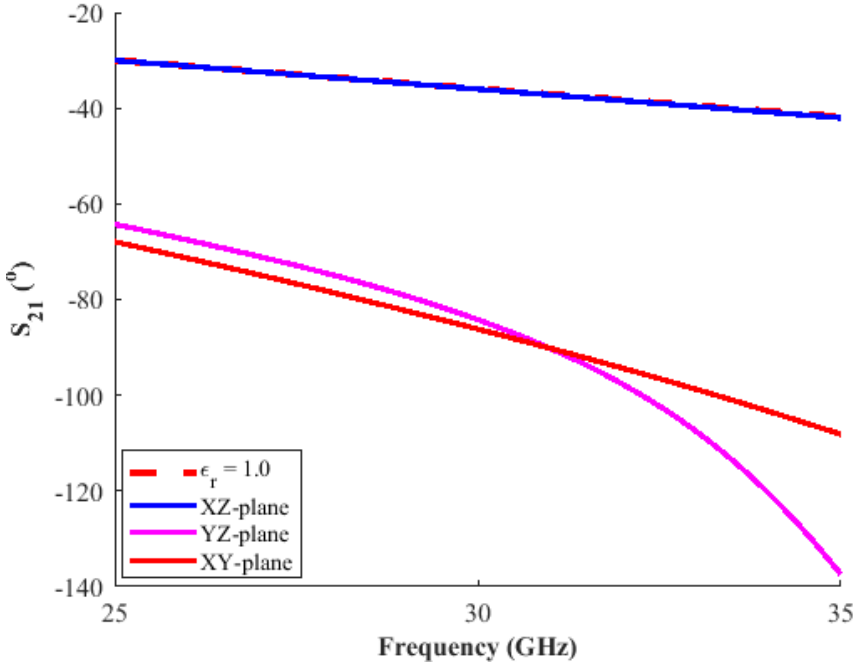

(b)

Fig. 5.4. Performance characteristics of the superstrate unit cell: (a) S_{21} magnitude; (b) S_{21} phase

Figs. 5.4(a) and (b) show that when the E_x-field of an incident plane wave is parallel to the periodic structure (Fig. 5.3(c)), and the H_y-field is orthogonal to the loop, we achieve a differential phase shift of 48.9° for the S_{21}, with a magnitude of -0.38dB, at the design frequency f =30GHz . Similarly, when the E_x-field of an incident plane wave is normal to the periodic structure (see Fig. 3(b)), the differential phase shift is 0° and the S_{21} magnitude is 0dB.

In contrast to these, we realize a differential phase shift of 75.6° when the incident plane wave on the periodic structure shown in Fig. 5.3(a) is Ex-polarized, which is considerably higher than what we had achieved for the Ex-polarized field. However, as shown in Fig. 5.4, the S_{21} magnitude for this case is -12.23dB, which is much higher than what we desire, even though we were willing to relax somewhat the insertion loss criterion of 0.5dB that we had set initially, as we have explained above.

It is evident from Fig. 5.4 that our objective of designing a low-cost variable phase shifter in the range of 0° to 45°, with a relatively low insertion loss, can be achieved by using the geometry in Fig. 5.5. We can obtain *variable* phase shifts ranging from 0° to 45° by systematically rotating the superstrate (truncated periodic structure) placed atop the antenna element, and thus varying its orientation from the y-z plane to the x-z plane.

Next, we study the performance of the metasurface-based superstrate when placed above a microstrip patch antenna (MPA), to determine its magnitude and phase behavior in the presence of the antenna element underneath. We begin the process by designing an MPA at the operating frequency f = 30GHz, by utilizing the closed-form expressions available in the literature [48] for designing MPAs. In Fig. 5.5, we show how we place the

superstrate, which is composed of a cluster of 7x5 elements of nested split rings, so that it can be rotated (τ) from 0° to 90°. The magnitude and phase for the same arrangements are shown in Fig. 5.6.

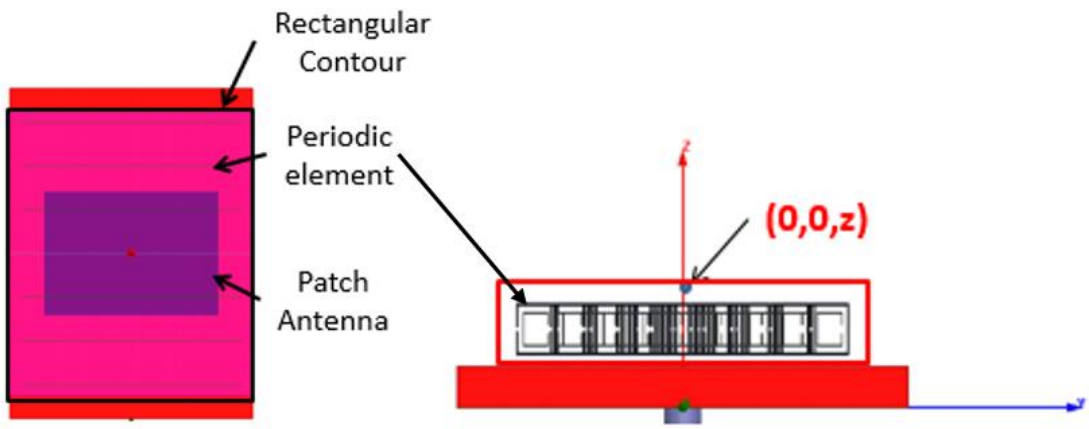

(a) (b)

Fig. 5.5. Metasurface-based superstrate with a rectangular shape loading an MPA source located below: (a) top view; (b) side view

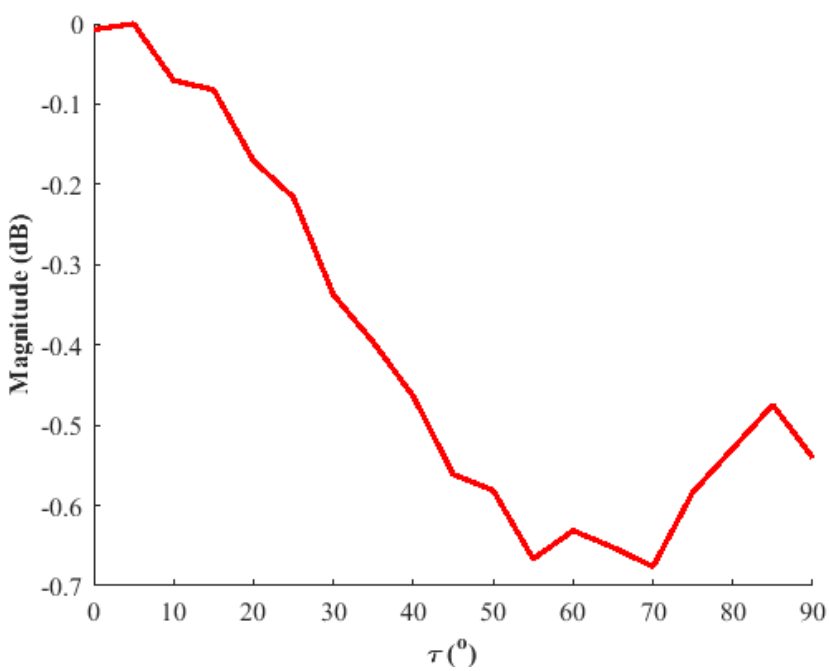

(a)

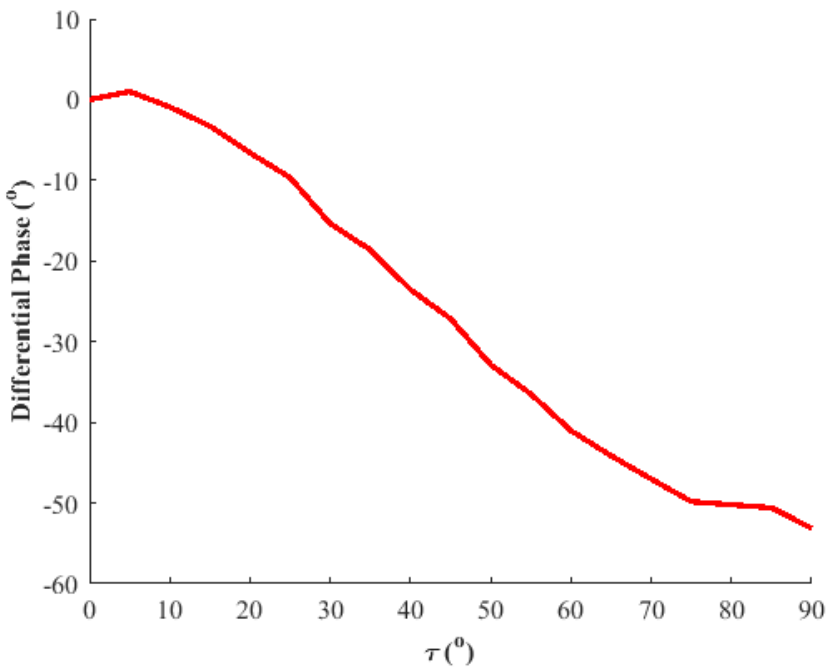

(b)

Fig. 5.6. Metasurface-based superstrate loaded on MPA source (a) Magnitude (dB); (b) Differential phase (°)

At this point, we observe that the rectangular shape of the superstrate, which appeared to be a logical choice to conform to the shape of the MPA, is not suitable for our application since it would start clashing with the element-plus-superstrate combination of the neighboring element (see Fig. 5.7) if we were to rotate it, which we would need to do to realize the variable phase shift. To circumvent the problem of obstruction of the neighboring elements to design the linear array, we decide to use a circular arrangement of periodic elements, as shown in Fig. 5.7.

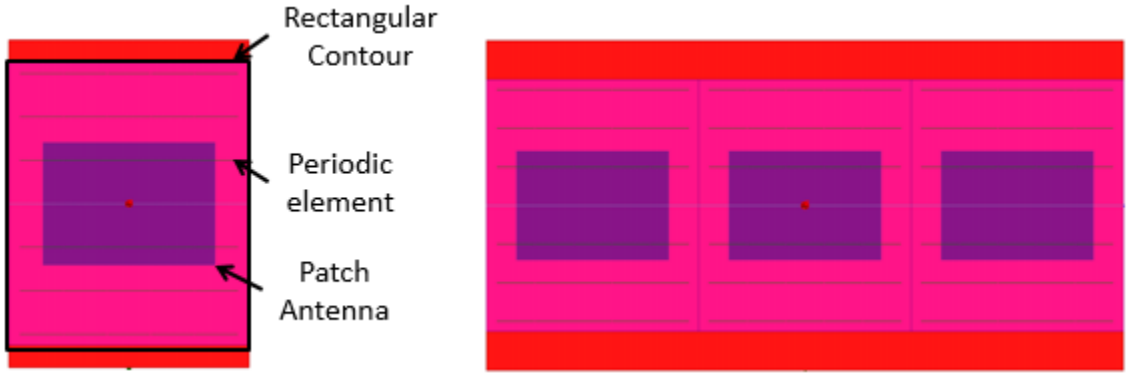

(a) Superstrates with rectangular shapes covering rectangular-shaped MPAs

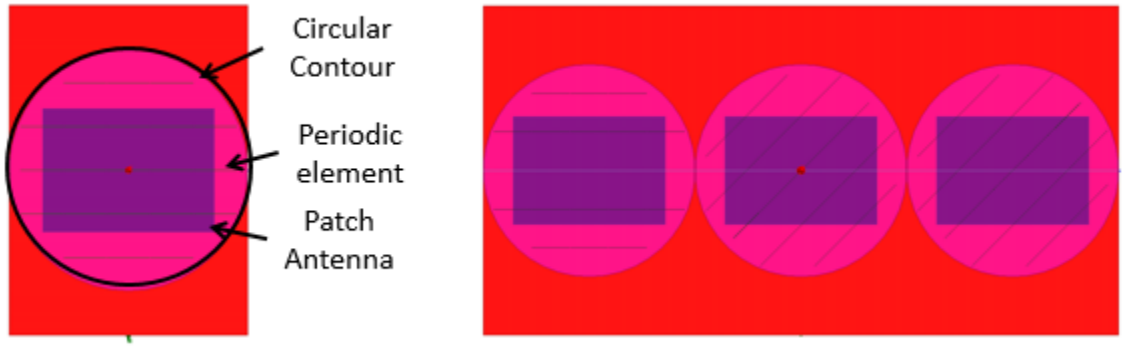

(b) Superstrates with circular shapes that enable rotation for phase-shifting

Fig 5.7. Metasurface-based superstrate loading an MPA; (a) rectangular; (b) circular.

The S_{21} magnitude and phase behaviors of the circular-shaped, metasurface-based superstrate loading an MPA is shown in Fig. 5.8.

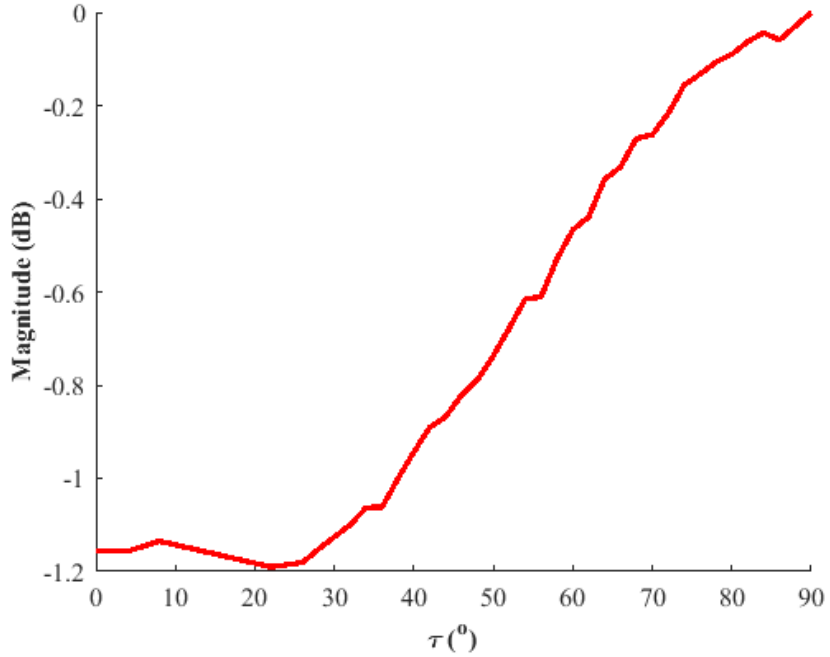

(a)

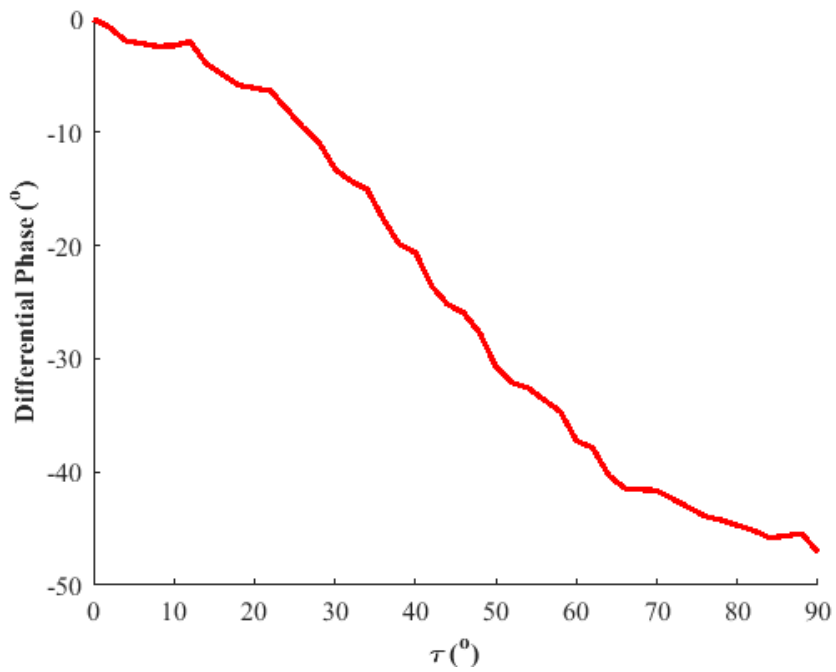

(b)

Fig. 5.8. Metasurface-based superstrate circular shape loaded on MPA source (a) Magnitude (dB) (b) Differential phase (°)

We can see from Fig. 5.8 that a differential phase shift of 47° with the S_{21} magnitude better than -1.2 dB, which was measured atop the superstrate at (0, 0, 2mm) as shown in Fig. 5.5, can be achieved at the design frequency f = 30GHz, by rotating the angle of the superstrate from 0° to 90°. We now create a database of S_{21} magnitude and phase *vs.* the angle of rotation (τ), from the results shown in Fig. 5.8, for future use.

By comparing the performances of the superstrate operating in the two scenarios, namely the plane-wave and antenna cases, we can see that in general there is no clear relationship that we can use to predict the magnitude and phase behaviors of the radiation characteristics of an antenna loaded with the metasurface-based phase shifter from the knowledge of its response to a plane wave. Thus, as pointed out earlier, the plane-wave results can only be used to develop initial guidelines for designing metasurface-based variable phase shifters of the type discussed herein, but not for final design.

5.3 Phase-Shifter in Linear Array for Beam Scanning

After realizing the desired phase shift range from 0° to 45°, and S_{21} magnitude on the order of 1.2 dB (or less) at the design frequency f = 30GHz, obtained by rotating the cluster angle (τ) from 0° to 90°, we proceed to design a linear array composed of 1x10 elements, to be used for beam scanning, using the metasurface-based superstrates as variable phase shifters and placing them above each of the antenna elements of the array, as shown in Fig. 5.9, to fine-tune the phase shifts of their radiated fields in the range of 0° to 45°, as supplements to their step-wise phase shifts realized by inserting switchable phase shifters in their feedlines.

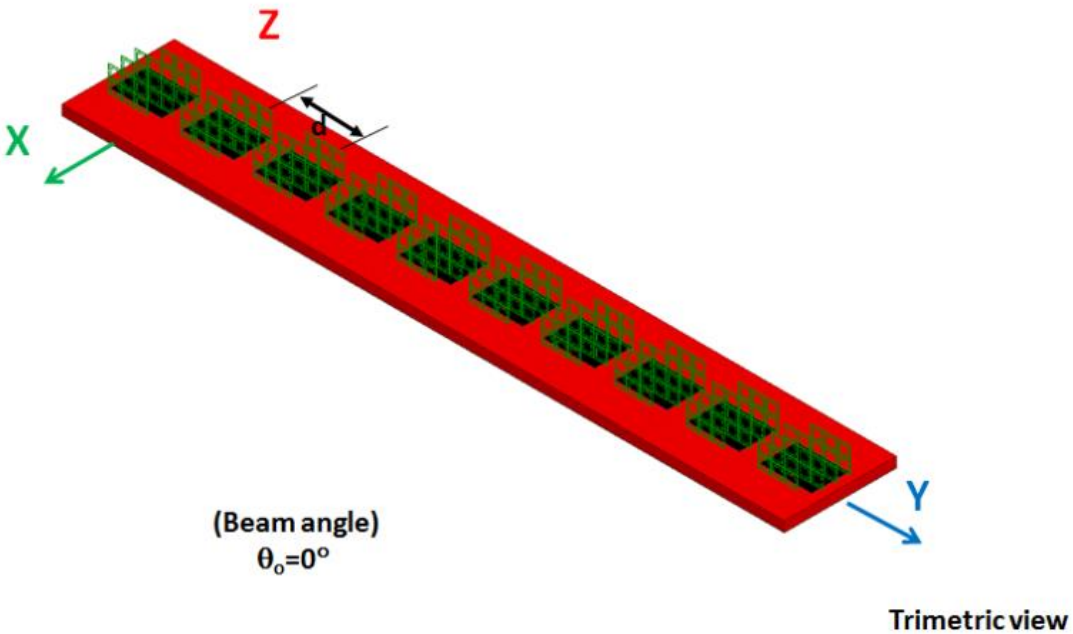

Fig. 5.9. Metasurface-based superstrate-loaded linear array of 1x10 elements

We have also determined, via numerical simulation, that grating lobes (GLs) can be avoided in a linear array designed for beam scanning if we choose the inter-element spacing to be less than 0.55λ. Let us assume that we wish to design a linear array that points its main beam at θ_o = 45°. The progressive phase shift needed for each element to scan the beam in the desired direction (i.e., θ_o = 45°) can be calculated using the following equation:

$$\text{Progressive phase } (\beta) \quad = -\frac{2\pi}{\lambda} d \sin\theta_0$$

Here, 'β' is the relative phase between the elements, 'd' is the spacing between each element in terms of λ, and 'θ_o' is the beam-pointing direction.

The progressive phase shifts (0°, 140°, 280°, etc.) that are needed by the elements of the array in order for it to scan the beam to 45° off boresight are shown in Table 5.2. The

desired phase shifts in the individual antenna elements are realized in two steps as follows: (i) in the first step, one part of the phase shift is introduced in the feed lines of the array elements by switching them in discrete steps of 0°, 45°, 90°, etc.; (ii) next, the second part of the phase shift is realized via the metasurface-based superstrate, by rotating the cluster at specific angles of rotation (τ), in accordance with the entries provided in Table 5.2, which represent the total of the two constituent phase shifts.

Table 5.2: Desired phase shifts needed for the array scan angle of $\theta_o = 45°$

Beam angle : 45°; d = 0.55λ; Progressive phase shift β = -140°										
Elements	**1**	**2**	**3**	**4**	**5**	**6**	**7**	**8**	**9**	**10**
Progressive phases at each element	**0**	**140**	**280**	**420**	**560**	**700**	**840**	**980**	**1120**	**1260**
Phase substraction(n*360°)	-	-	-	-	360	360	720	720	1080	1080
Desired Phase at each element	0	140	280	60	200	340	120	260	40	180
Phase using Standard Phase shifter (Discrete steps : 0,45,90..)	**0**	**135**	**270**	**45**	**180**	**315**	**90**	**225**	**0**	**180**
Phase using Rotatable Phase Shifter	**0**	**5**	**10**	**15**	**20**	**25**	**30**	**35**	**40**	**0**
Rotation angle of Split Ring (τ)	**0**	**18**	**27**	**34**	**39**	**44**	**51**	**57**	**64**	**0**

Fig. 5.10 shows a 1×10 linear array with its elements loaded with the metasurface-based superstrate variable phase shifter designed to scan the beam to $\theta_o = 45°$off boresight.

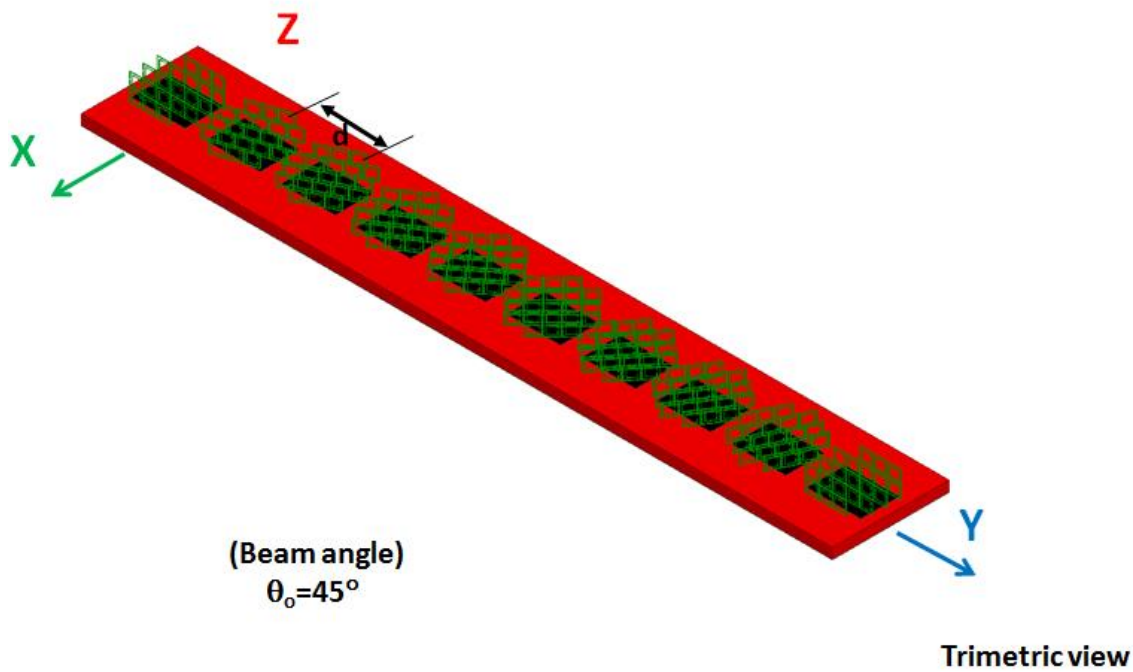

Fig. 5.10. Linear array of 1x10 elements loaded with the metasurface-based superstrate

To validate the results of the beam scanning design, we have checked the phase distribution of the field on a surface just above the metasurface-based superstrate, against the calculated phase given in Table 5.3. Fig. 5.11 shows that the realized phase values are in close agreement with the desired ones at the design frequency of 30GHz.

5.4 Results

Fig. 5.12 depicts the gain plots of the 1x10 array for four different beam-scanning angles, namely 0°, 15°, 30° and 45°. Additionally, Table 5.4 presents the gain values for different scan angles in a tabular form.

Table 5.3: Phase comparison of 1x10 linear array for the scan angle of $\theta_o = 45°$

Beam angle : 45°; d = 0.55λ; Progressive phase shift β = -140°										
Elements	**1**	**2**	**3**	**4**	**5**	**6**	**7**	**8**	**9**	**10**
Progressive phases(°) at each element (Calculated)	0	140	280	420	560	700	840	980	1120	1260
Progressive phases(°) at each element (Measured on top of the superstrate)	0	141	292	431	571	712	853	994	1136	1277

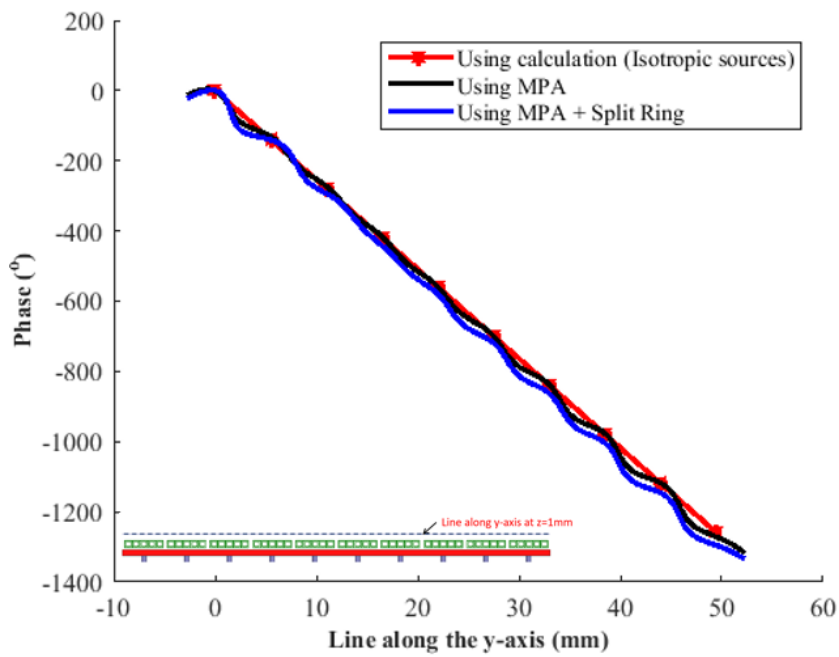

Fig. 5.11. Phase comparisons of 1x10 linear array for the scan angle of $\theta_o = 45°$

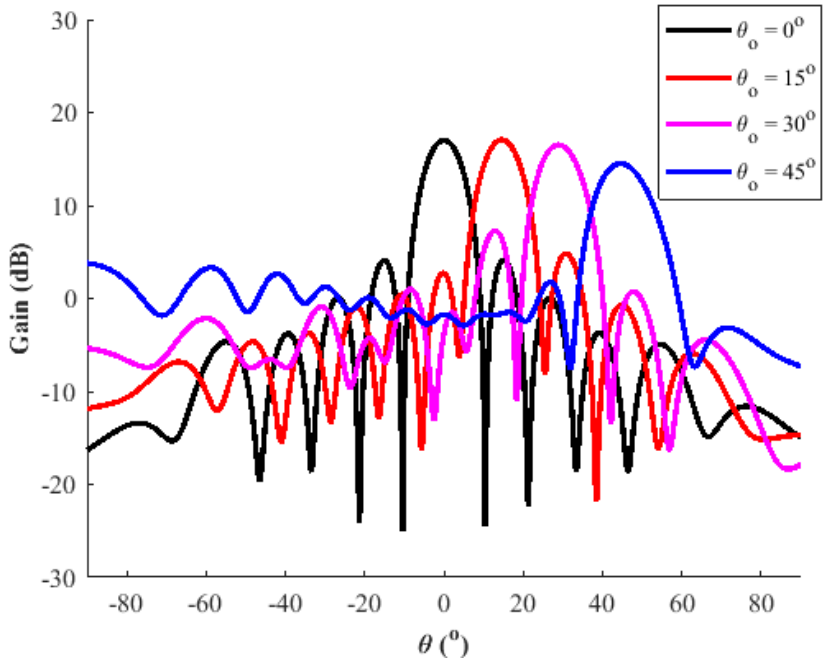

Fig. 5.12. Gain for 1×10 element linear array for different scan angles

Table 5.4: Gain values for the different beam scan angles

Sr. No.	Beam angle (θ_o)	Gain (dB)
1	0°	16.91
2	14.6°	16.89
3	29.1°	16.53
4	44.9°	14.9

Fig. 5.12 clearly demonstrates that the beam can be systematically scanned from boresight to 45° by rotating the metasurface-based superstrate that loads the 1×10 element linear array. It should be pointed out that the phase-shifting mechanism discussed herein is only viable for the linear polarization case and that a different design philosophy is needed

to deal with the circularly polarized case. The CP case is currently under study and the results of the investigation will be reported in the future.

Chapter 6

Offset-Fed Metal-Only Reflectarray (MORA) Antenna Designs Using Frequency Selective Surfaces (FSSs)

6.1 Introduction

Planar high-gain antennas have witnessed an increasing demand for applications such as satellite communications, direct broadcasting services (DBS), radar, etc. Conventional reflectors or electronically scanned array antennas have been employed to satisfy the need for high gain. Reflector antennas are designed to divert the beam radiated by the feed source in the desired direction by shaping the curved and electrically large surfaces, based on the geometrical optics, which may make them undesirable for certain applications where low-profile as well as low-cost fabrication are required. In addition, close attention must be paid when fabricating a reflector antenna for high frequency applications, since the surface accuracy must be high at these frequencies to prevent gain loss. Alternative antenna designs (e.g., electronically scanned antenna arrays) have desirable features such as low-profile scan capability; however, they are complex in nature, since they comprise multiple transmit/receive modules, a processing unit, phase shifters, etc., which are needed for beamforming. All these features add to their cost.

A reflectarray antenna [49]–[54], is a planar array of printed phasing elements illuminated by a prime-focus feed source, which is shown in Fig. 6.1(b). The reflectarray uses a reflecting surface to control the phase of the outgoing beam by placing phasing elements on its surface to transform an obliquely incident spherical wave into a planar wave

front, mimicking the performance of a parabolic reflector, but with a flat surface. In contrast to a conventional array antenna, a mature, inexpensive manufacturing technique like lithography is used for the phasing elements in reflectarray antennas. Traditionally, printed dipoles, microstrip patches, rings or loops are used in reflectarrays as phase-shifting elements.

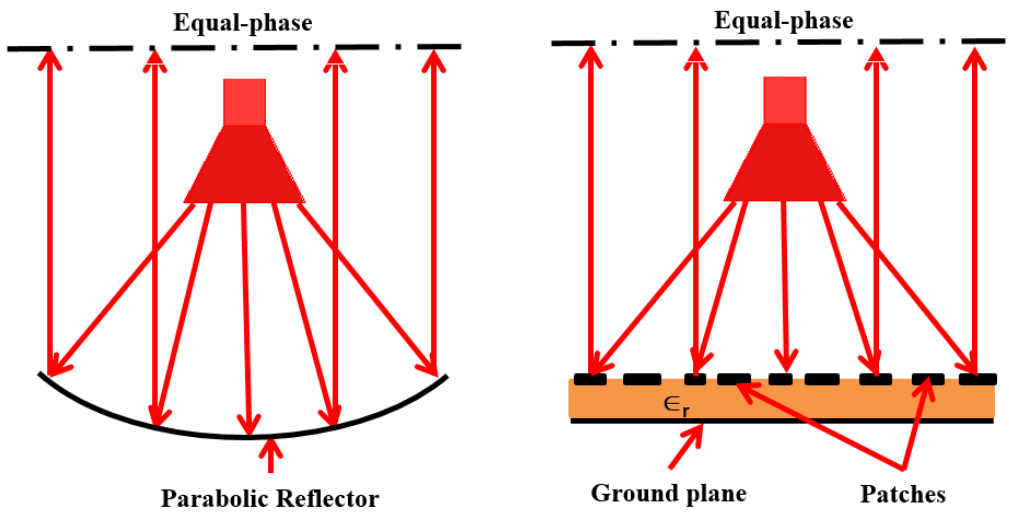

Fig. 6.1. Design schematics of reflectarray (RA) (a) Parabolic reflector; (b) Printed RA

Recently, the metal–only reflectarray antennas (MORAs) have received attention because they require neither etching nor dielectric substrates; hence, they are not only low cost, but also less susceptible to environmental conditions when deployed in space. Several metal-only designs have been proposed by researchers, including one of the earliest examples in [54] that uses slot-type phasing elements [55]–[56].Three-dimensional designs have also been proposed in [57]–[59].

In this chapter, we present two different offset-fed MORA designs using 2D and 3D phase-shifting elements. The first of these designs consists of two metallic sheets separated

without any dielectric materials in between, while the second is composed of 3D elements. We carry out a study of the radiation performance characteristics of the above MORAs in this chapter.

6.2 Offset-Fed Metal-Only Reflectarray (MORA) Designs

We denote the feed horn as illuminating the reflectarray surface at an angle θ, as shown in Fig. 6.4. We place the phase shifting elements above the ground plane, at a height of h, which reflect the incident field in a way such that the reflected beam is directed in the desired direction(φ_b, θ_b). For a collimated beam in the direction(φ_b, θ_b), the required progressive phase distribution can be expressed as [50]:

$$\emptyset(x_i, y_i) = -k_o sin\theta_b cos\varphi_b x_i - k_o sin\theta_b sin\varphi_b y_i \qquad (6.1)$$

where (x_i, y_i) are the coordinates of element i, and k_o is the wave number in vacuum.

Since the phase of the reflected field at each element is the sum of the phase of the incident field and the phase-shift introduced by each element of the reflectarray, we can write:

$$\emptyset(x_i, y_i) = -k_o d_i + \emptyset_R(x_i, y_i) \qquad (6.2)$$

where $\emptyset_R(x_i, y_i)$ is the phase contributed by the phase-shifting element i, and d_i is distance of the element to the phase center of the feed (see Fig. 6.2).

From (6.1) and (6.2), we can deduce that the phase-shift required at each element is given by:

$$\emptyset_R = k_o\big(d_i - (x_i cos\varphi_b + y_i sin\varphi_b)\big)sin\theta_b \qquad (6.3)$$

After calculating the desired phase-shifts given by (6.3) at each element, we move on towards the selection of phase-shifting elements for our reflectarray designs. After considering a number of potential candidates, we choose the 2D cross-slot, 3D-cross and 3D-cross-groove phasing elements for our MORA designs, which are shown in Figs. 6.3, 6.4 and 6.5.

The design specifications for the reflectarray are *f* (design frequency) = 35.6GHz; A*x* × A*y* (aperture size) where $A_x = A_y$ = 96.83mm (11.5λ); θ (tilt angle) = 30°; ϕ = 180°; H_f (height of feed) = 75mm (8.9λ). The desired frequency band is Ka-band (35.35–35.85GHz) and the center frequency chosen for our design is 35.6GHz. We use a Ka-band pyramidal horn antenna with an open end dimension of 12.3mm by 8.9mm at the height of 75mm as the feed antenna.

6.2.1 Metal-Only Reflectarray Design Using Cross-Slot Element

We introduce an alternative reflectarray design in this section using the cross-slot phasing element. The phase-shifting element for the reflectarray design is shown in Fig. 6.2, which has impressive reflection performance, such as capability of achieving full 360° phase shift that was not realizable using conventional elements [57]. The part shown in green in the schematics of the design is the upper layer metal, which is placed at height *h* above a metallic ground plane, depicted in red. We evaluate the reflection performance of the phasing element by varying the length of the slot L, and track the corresponding phase of the reflection coefficient. The dimensions of the phasing elements are cross-slot width *G*

= 0.5mm; slot connection width g = 0.2mm, height h = 0.787mm and periodicity of the element A = 4.21mm ($\lambda/2$). We use a commercial FEM solver to model the element. The phase response of the reflection coefficient of the unit cell is shown in Fig. 6.3, at the center frequency f (design frequency) = 35.6GHz as well as for the entire working frequency band (i.e., Ka-band: 35.35–35.85GHz). The plot shows that we can realize the desired phase range of 360° by varying the length, L of this element.

Next, we choose the cross-slot length 'L' from Fig. 6.3 based on the requisite reflection phase, which is calculated using (6.3). We then place cross-slot elements with appropriate lengths along the x-axis for different values of y. The placements of these cross-slots complete our offset-fed MORA antenna design as shown in Fig. 6.4 to direct the main beam in the normal direction. Fig. 6.5 shows a typical reflectarray design realized by using cross-slot phasing elements.

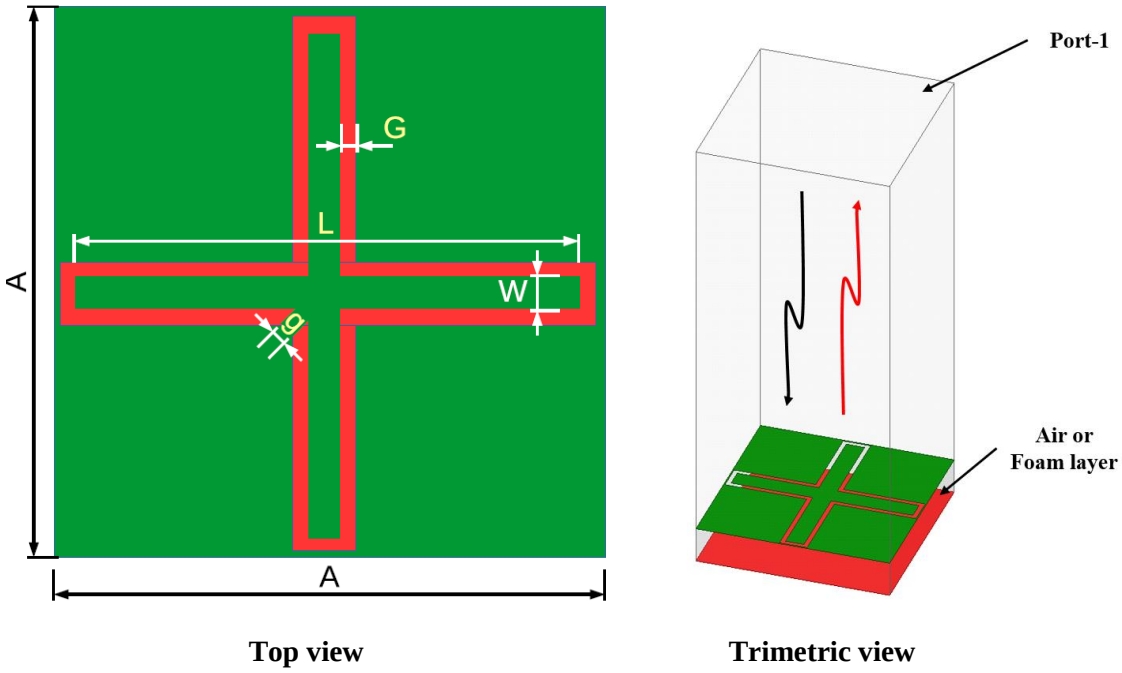

Fig. 6.2. Cross-slot phasing element; green part is metal and red part is the slot carved out of metal

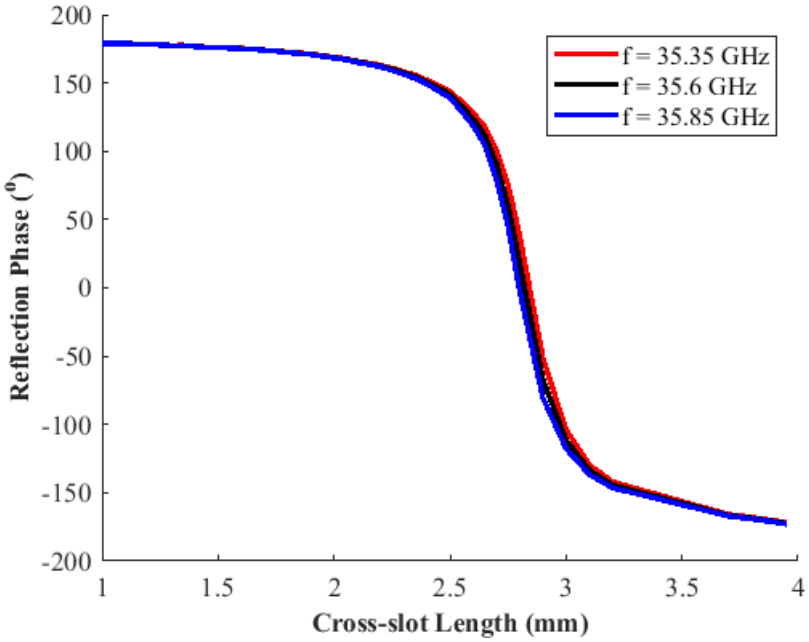

Fig. 6.3. Reflection phase of cross-slot phasing element

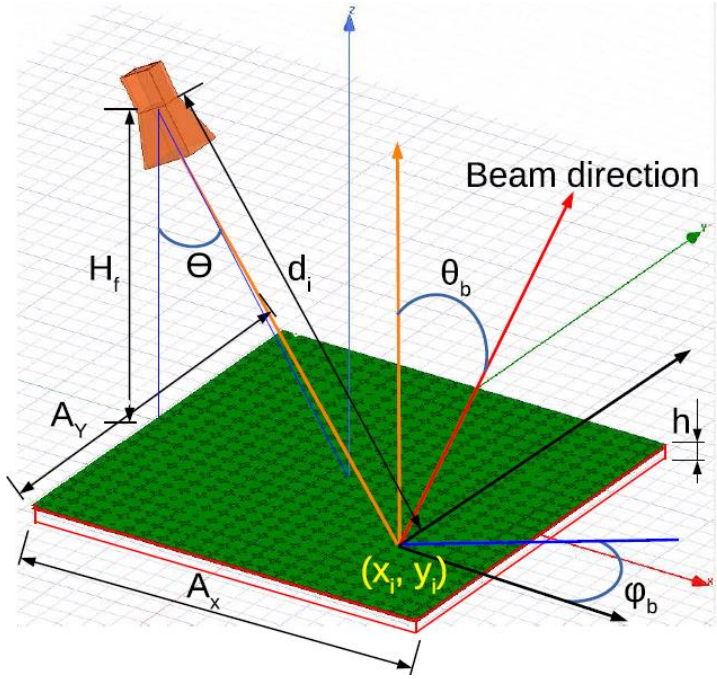

Fig. 6.4. Metal-only reflectarray (MORA) using cross-slot phasing element

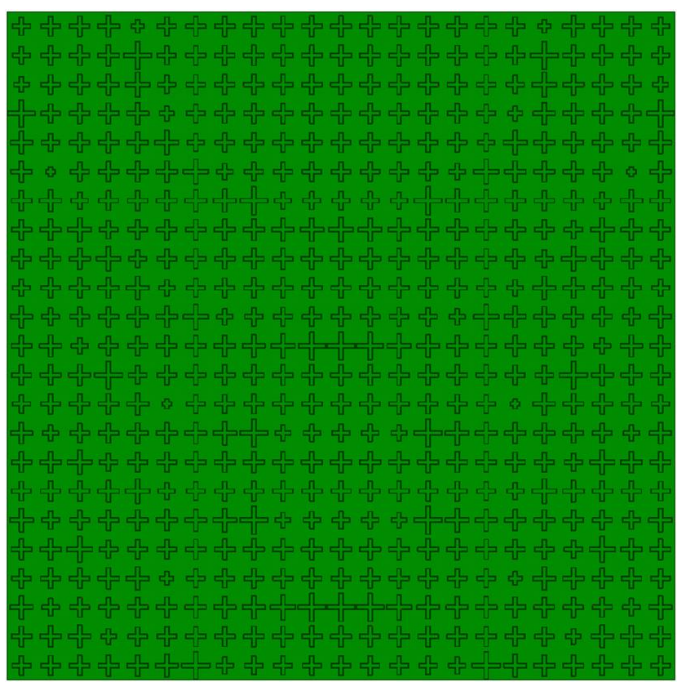

Fig. 6.5. Typical reflectarray derived by using cross-slot phasing elements

To validate the performances of the reflectarray (i.e., the direction of the main beam), we check "total" phase distribution of the field on a surface just above the cross-slot, against the calculated total phase given in Table 6.1. These phase values are for the phasing element placed along the x-axis for y = 0mm. Fig. 6.6 shows that the realized phase values at the design frequency of 35.6GHz are in close agreement with the desired ones.

Table 6.1: Phase comparison of cross-slot reflectarray for the beam angle of $\theta_b = 0°$

Location along x-axis (mm)	-(Ax/2) -46.3	-42.1	-37.9	-33.7	-29.5	-25.3	-21.1	-16.8	-12.6	-8.4	-4.2
Desired Total Reflected Phase(°)	0	0	0	0	0	0	0	0	0	0	0
Line placed at y = 0	-3.65	-4.16	-3.01	-1.01	-0.16	-1.26	-2.36	-1.73	-0.66	-0.11	-1.16

Location along x-axis(mm)	0.0	4.2	8.4	12.6	16.8	21.1	25.3	29.5	33.7	37.9	42.1	(Ax/2) 46.3
Desired Total Reflected Phase(°)	0	0	0	0	0	0	0	0	0	0	0	0
Line placed at y = 0	-2.77	-2.25	-2.16	-1.11	-1.13	-1.01	-2.22	-3.33	-4.73	5.05	-6.41	-10.1

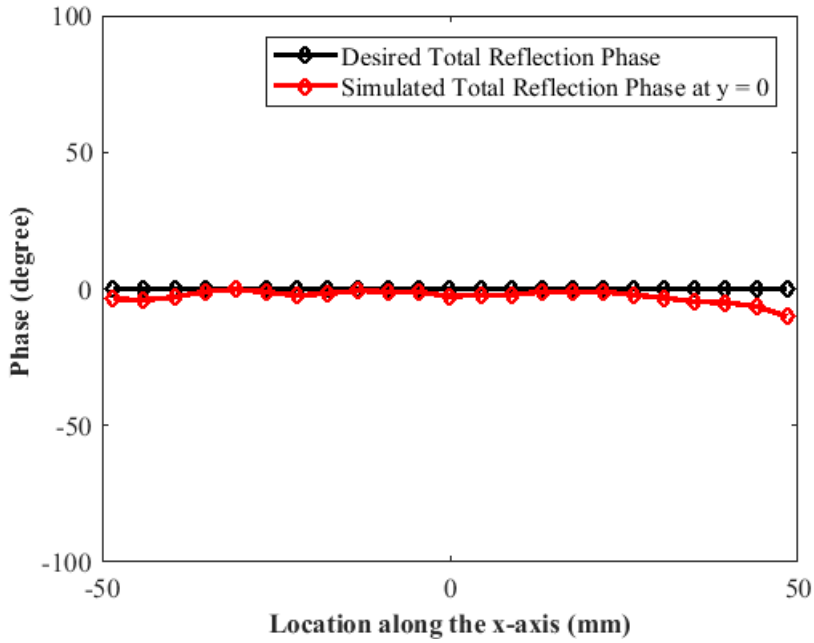

Fig. 6.6. Phase comparison of cross-slot reflectarray along x-axis at y=0 for radiation in normal direction

6.2.1.1 Results

Figs. 6.7 and 6.8 show the radiation patterns of the reflectarray with radiation in normal and specular directions, respectively. The aperture efficiency of the reflectarray is calculated by using the following well-known definition:

$$\eta = \frac{G\lambda^2}{4\pi A} \tag{6.4}$$

where A and G denote the physical area and gain, respectively.

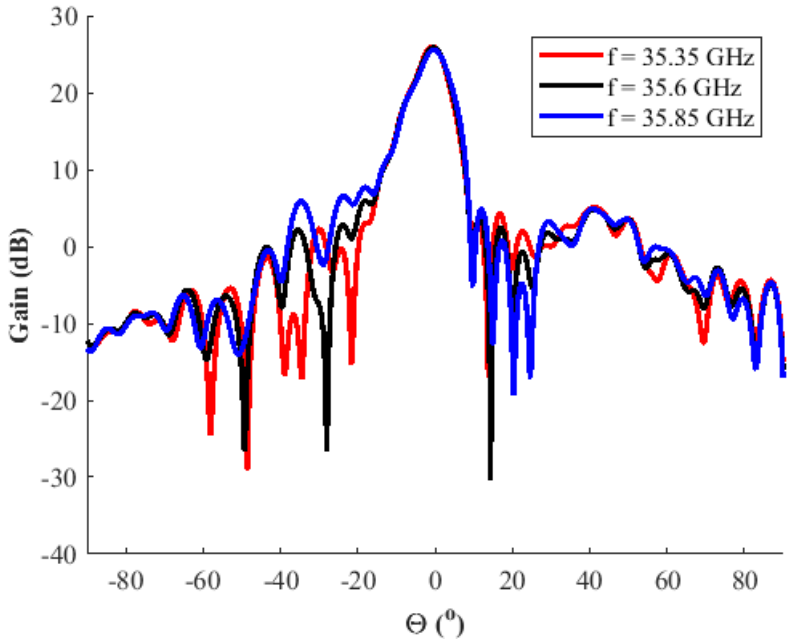

Fig. 6.7. Simulated radiation pattern of the MORA designed using cross-slot phasing element in the normal direction

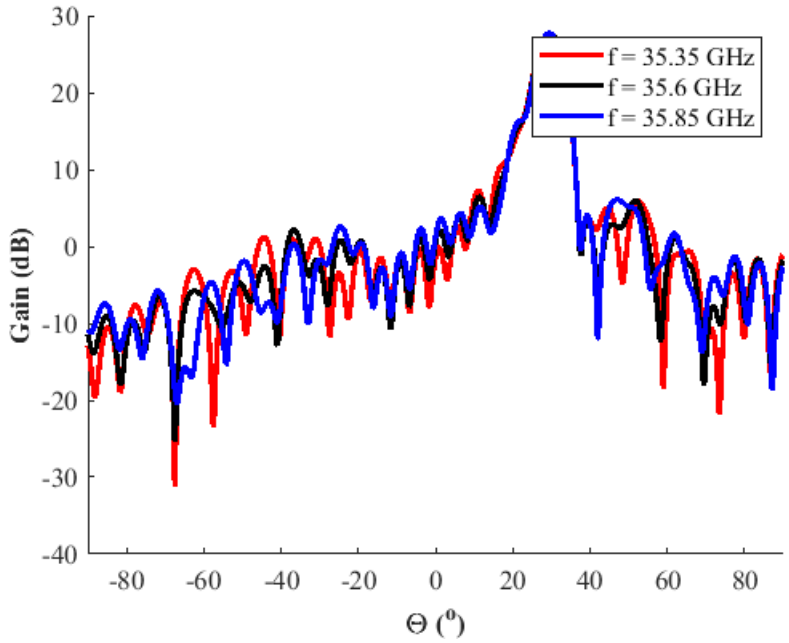

Fig. 6.8. Simulated radiation pattern of the MORA designed using cross-slot phasing element in the specular direction

The simulated gain of metal-only reflectarray designed using the 2D cross-slot type of phasing element is found to be 26.2dBi at 35.6GHz with an aperture efficiency of 25.1% and sidelobe level of -21dB for the normally directed beam. The corresponding values of the specularly directed beam reflectarray are gain of 28dBi at 35.6GHz, aperture efficiency of 35.4%, and sidelobe level of -21dB. We find that the gain of reflectarray with the specularly radiated beam is higher than that of the one with the normally radiated beam. We also find that the sidelobe level of the reflectarray with the specularly radiated beam is lower than that of the one with normally radiated beam.

6.2.2 Metal-Only Reflectarray Design Using 3D-Cross Element

For this reflectarray, we use the 3D-cross phasing element as shown in Fig. 6.9, which provides a linear phase shift of up to 360° by linearly varying the element height. It is also worthwhile to mention that the reflectarray is lightweight due to simple structure of the phasing element, which utilizes less metal with 3D-printing. The red part in the unit cell as shown in Fig. 6.9 is the metallic ground plane on which the 3D-cross element (shown in green) is printed. We evaluate the reflection performance of the phasing element by varying the height '*h*' of the element. The dimensions for the phasing element are 3D-cross width W = 0.5mm; 3D-cross length A_L = 4.21mm and periodicity of the element *A* = 4.21mm (λ/2). The reflection phase response of the unit cell is shown in Fig. 6.10, for *f* (design frequency) = 35.6GHz as well as for the entire frequency band (i.e., Ka-band: 35.35–35.85GHz). The plot shows that we can realize the desired phase range of 0 to 360° by varying the 3D-cross phasing element height *h* from 0.15 to 4.9mm with the resolution of

0.05mm.

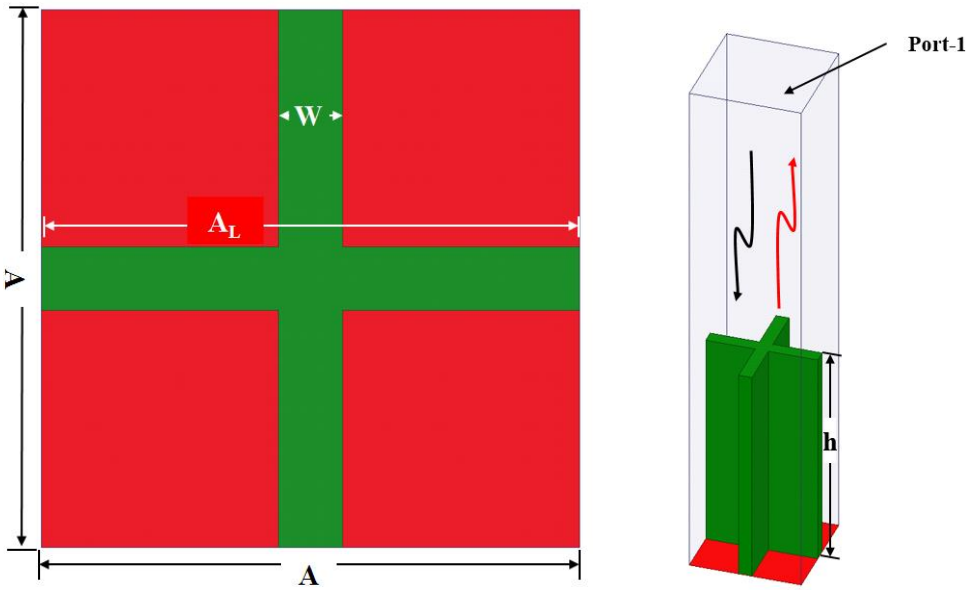

Fig. 6.9. 3D-cross phasing element; green part is 3D metallic element and red part ground plane

We choose the 3D-cross height '*h*' from Fig. 6.10 based on the desired reflection phase from (6.3) to radiate the beam in the normal direction. Next, we place 3D-cross elements along the x-axis for different values of *y*. The placements of these elements complete our offset-fed reflectarray antenna design as shown in Fig. 6.11 for the main beam in the normal direction. Fig. 6.12 shows a reflectarray design realized by using 3D-cross phasing elements.

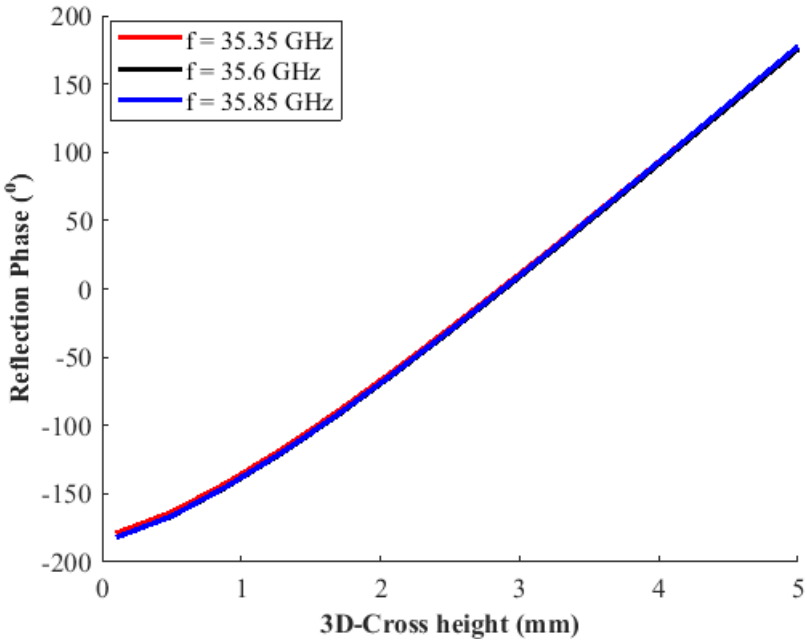

Fig. 6.10. Reflection phase of 3D-cross phasing element

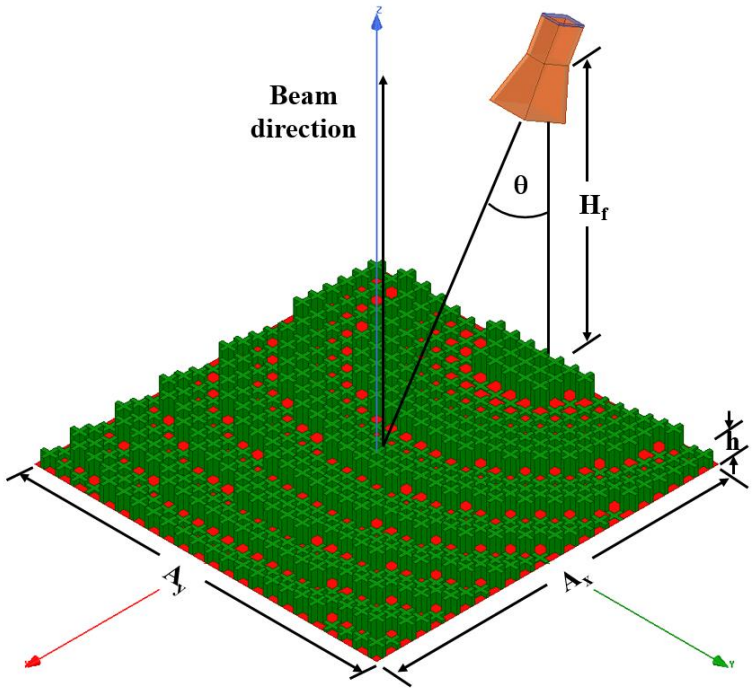

Fig. 6.11. Metal-only reflectarray using 3D-cross phasing element

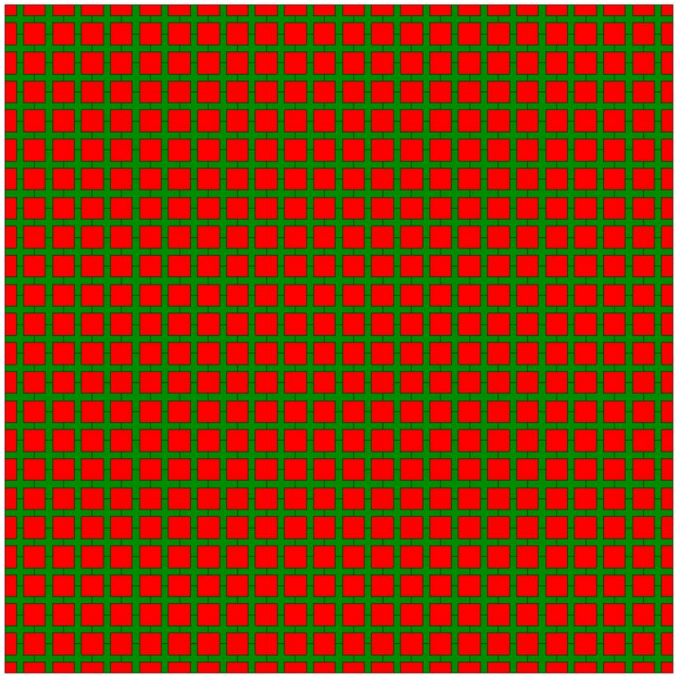

Fig. 6.12. Typical reflectarray derived by using 3D-cross phasing elements

We checked the phase distribution of the field on a surface just above the 3D-cross, against the desired total reflection phase given in Table 6.2. These phase values are for the phasing elements placed along the x-axis for y=0. Fig. 6.13 shows that the simulated phase values are in close agreement with the desired ones at the design frequency of 35.6GHz, except for the phase values at the edges of the reflectarray far away from the source location (i.e., at x = $A_x/2$).

Table 6.2: Phase comparison of 3D-cross reflectarray for the beam angle of $\theta_b = 0°$

Location along x-axis (mm)	-(Ax/2) -46.3	-42.1	-37.9	-33.7	-29.5	-25.3	-21.1	-16.8	-12.6	-8.4	-4.2
Desired Total Reflected Phase(°)	0	0	0	0	0	0	0	0	0	0	0
Line placed at y = 0	-4.45	-3.16	-2.11	-2.01	-1.36	-1.16	-1.26	-1.43	-1.66	-1.51	-1.01

Location along x-axis(mm)	0.0	4.2	8.4	12.6	16.8	21.1	25.3	29.5	33.7	37.9	42.1	(Ax/2) 46.3
Desired Total Reflected Phase(°)	0	0	0	0	0	0	0	0	0	0	0	0
Line placed at y = 0	-5.71	-5.45	-4.44	-4.32	-4.23	-5.11	-4.31	-5.44	-5.53	-6.05	-7.11	-11.2

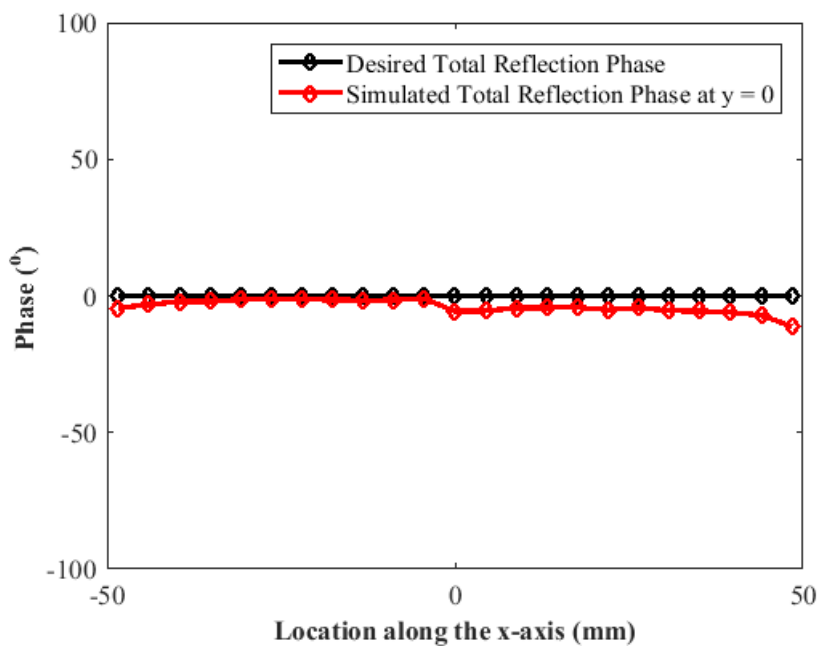

Fig. 6.13. Phase comparison of 3D-cross reflectarray along x-axis at y=0 for radiation in normal direction

6.2.2.1 Simulated Results for Reflectarray Designs

Fig. 6.14 shows the radiation patterns of the reflectarray with the main beam in the normal direction. The aperture efficiency of the reflectarray is calculated using 6.4. The simulated gain is 28.9dBi at 35.6GHz with an aperture efficiency of 47% and sidelobe level of -19.7dB for the beam radiating in the normal direction. We also show in Fig. 6.14 that the gain performances are consistent within the desired frequency band. We find that the gain of the reflectarray with 3D-crosses is higher than that of the normally radiated beam design using 2D cross-slots.

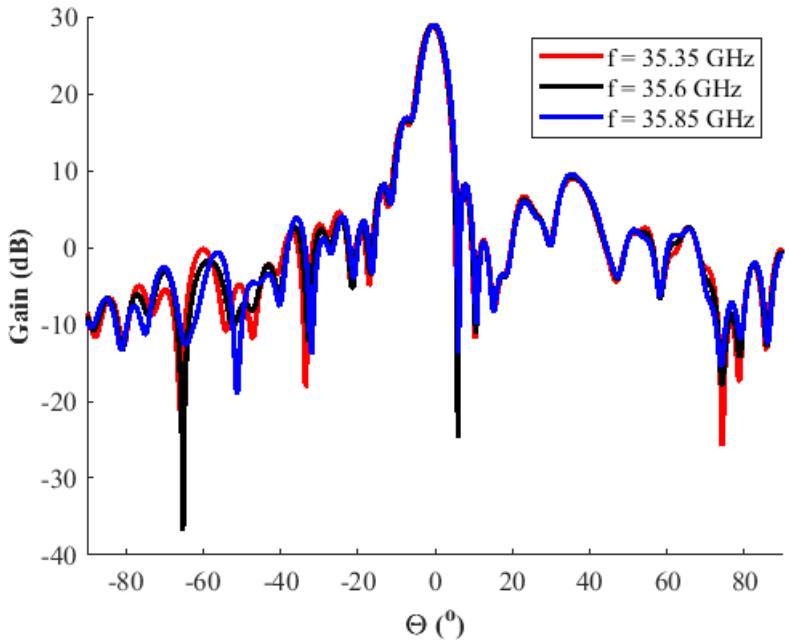

Fig. 6.14. Simulated radiation pattern of the MORA designed using 3D-cross phasing element

6.2.3 Metal-Only Reflectarray Design Using 3D-Cross-Groove Element

In this section, we demonstrate a dual-band (Ka/W) reflectarray design. We use 3D-cross-grooves as phasing elements to design the Ka-band and rotate cross-groove phasing elements for W-band reflectarray design. The 3D-cross-groove element is the complementary structure to the phasing element presented in Sec. 6.2.2 (i.e., the 3D-cross). The reasons for choosing a new phasing element are that it has a flat-top surface and that it shows no blockage effects due to tall elements, which was a cause for concern of the phasing element that we discussed in Sec. 6.2.2. This new phasing element for the Ka-band reflectarray design is shown in Fig. 6.15, which provides a phase shift with 360° coverage by varying the element depth. The black line forming the cross-groove in the green metallic block is shown in Fig. 6.15. We also introduce the rotated cross-groove phasing element in Fig. 6.17 for the W-band reflectarray design. We evaluate the reflection performances of both phasing elements by varying the depths 'A_{GD}' and 'B_{GD}' of the elements.

We carried out a parametric study of the A_{GW} (groove width) and evaluated the reflection phase responses of the proposed phasing element to a *y*-polarized incident field. The result is shown in Fig. 6.16 for f (design frequency) = 35.6GHz. We note that the groove widths have an impact on the slope of the reflection phase. With a A_{GW} = 0.1mm and 0.3mm we achieved the coverage of 360° phase shift; but the slope of the phase curve at resonance is somewhat steep for this design, which presents a manufacturing challenge owing to tolerance issues. We also conducted a parametric study of the width of the rotated cross-groove B_{GW} and evaluated the reflection phase responses as shown in Fig. 6.18. We adopted the combination of A_{GW} = 0.5mm and B_{GW} = 0.5mm for Ka and W-band,

respectively, because it was observed that the reflection phase slope is gentler, which indicates a less drastic transition and broader element bandwidth.

The dimensions for the Ka-band phasing element are groove width A_{GW} = 0.5mm, groove length A_{GL} = 4.85mm and periodicity of the element A = 5mm (0.59λ at 35.6GHz). Similarly, the dimensions for the W-band phasing element are B_{GW} = 0.5mm, groove length B_{GL} = 2mm and periodicity of the element B = 2.5mm (0.78λ at 94.05GHz).

In Sec. 6.2.3.1, we explain the design steps for the dual-band (Ka/W) metal-only reflectarray to radiate the beam in the normal direction, which utilizes cross-groove rotated cross-groove phasing elements to achieve the desired phase compensation on the surface of the reflectarray.

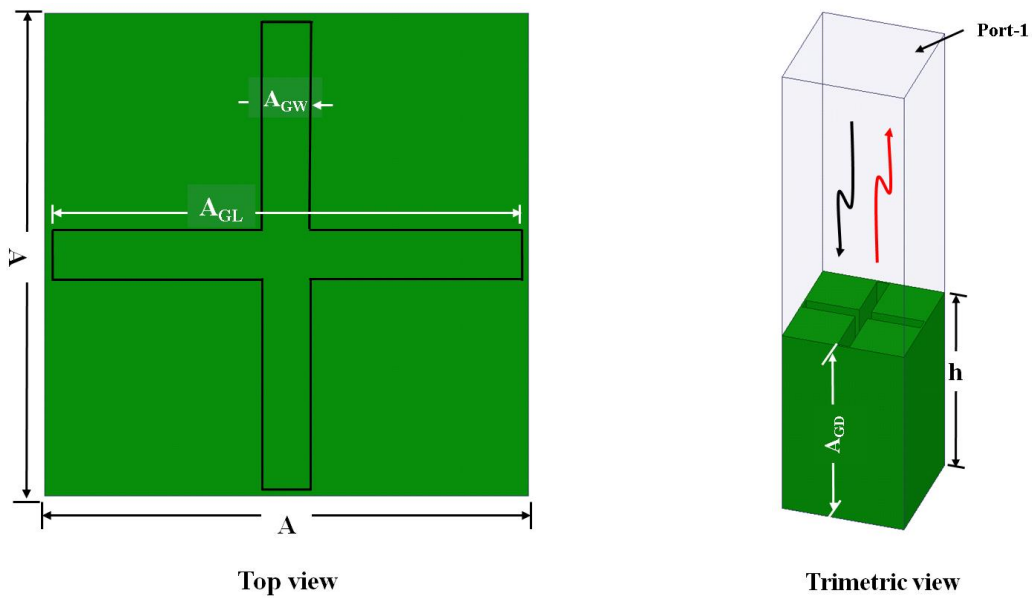

Fig. 6.15. Ka-band (Low-frequency(Lf)) phasing element (a) Top view; (b) Trimetric view

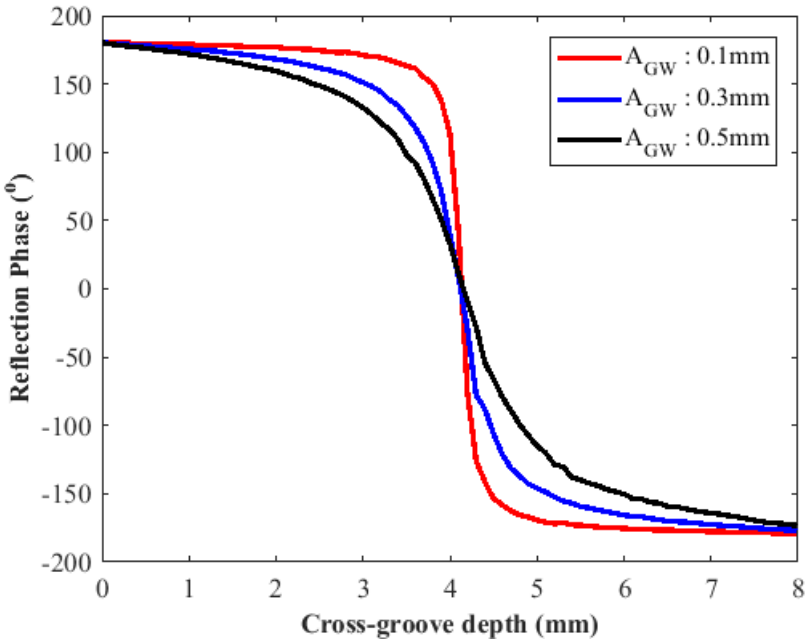

Fig. 6.16. Reflection phase of cross-groove phasing element for different groove widths

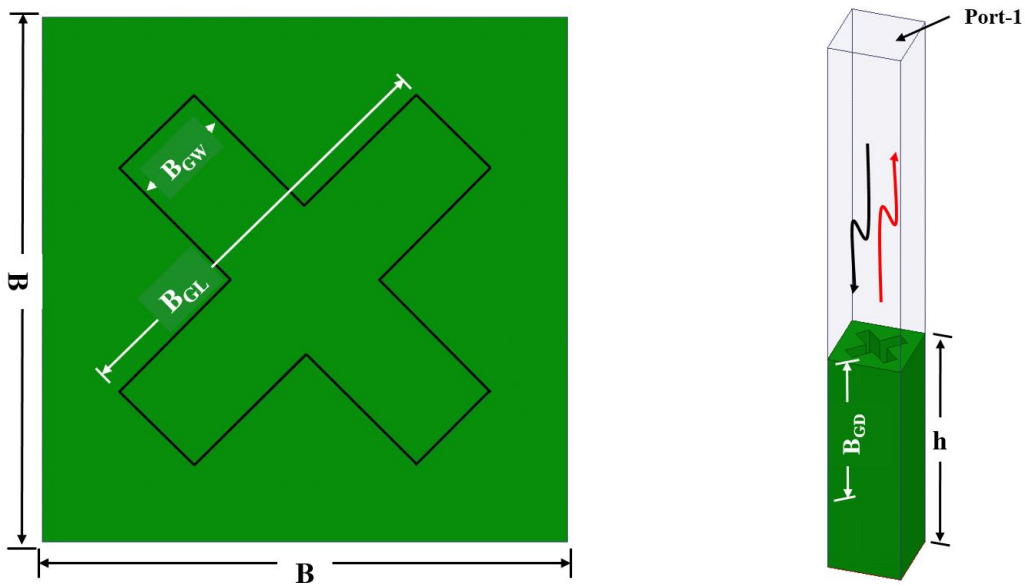

Fig. 6.17. W-band (high-frequency(Hf)) phasing element (a) Top view; (b) Trimetric view

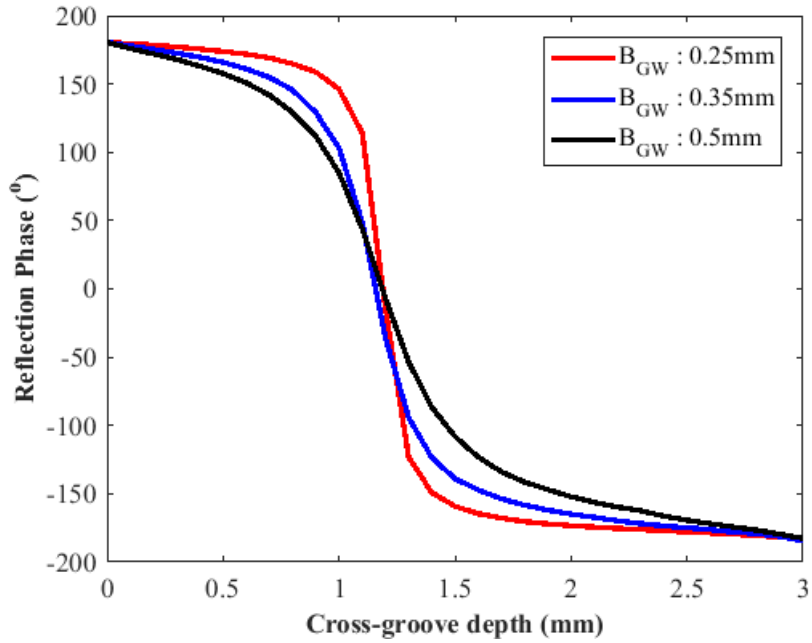

Fig. 6.18. Reflection phase of cross-groove at *f* (design frequency) = 94.05GHz, for different groove widths

6.2.3.1 Design Steps for Dual-Band (Ka/W-Band) MORA Design

To design the dual-band metal-only reflectarray (MORA) at 35.6GHz (Ka-Band) and 94.05GHz (W-band), we start with a Ka-band reflectarray design. As shown in Fig. 6.15, we use the 3D-cross-groove phasing element to design the dual-band MORA. The low-frequency (Lf) phasing element has a periodicity of 5*mm*, which is 0.59λ at 35.6GHz. The high-frequency(Hf) phasing element is shown in Fig. 6.17. The phasing element is a 45° rotated cross-groove with a periodicity of 2.5mm, which is 0.78λ at 94.05GHz. These W-band phasing elements are placed in the four quadrants separated by the Ka-band 3D-cross-groove, which is at the center of the unit cell as shown in Fig. 6.19.

1) Design Steps for Ka-Band (*f* = 35.6Ghz) Reflectarray Using Cross-Groove Phasing Elements

i. We begin the process with a single-band design and use the cross-groove phasing element, as shown in Fig. 6.15.

ii. After determining the unit cell dimension for low-frequency phasing elements, which is 0.59λ at 35.6GHz, we calculate the desired reflection phase using (6.3) at the center of each Lf cell on the reflectarray surface for a desired exit beam angle (i.e., $\theta = 0°$ and $\phi = 0°$).

iii. Next, based on the desired reflection phase, we select the Lf element depth from the S-curve as shown in Fig. 6.16. This completes our design for the offset-fed Ka-band reflectarray design, as shown in Fig. 6.21.

iv. Finally, we move to the design of a W-band MORA in the presence of Ka-band elements.

2) Design Steps for W-Band (*f* = 94.05GHz) Reflectarray Using 45° Rotated Cross-Groove Phasing Elements in the Presence of Ka-Band Elements

i. The design of a W-band reflectarray is carried out in the presence of Ka-band elements, for the unit cell dimension of 0.78λ for the Hf phasing element at 94.05GHz.

ii. The Hf phasing elements are placed in four quadrants, as shown in Fig. 6.19, in the presence of the center cell, as discussed earlier.

iii. We start by choosing the cell on the reflectarray surface for which the Hf phasing element depth has to be decided. Note that the depth of the Lf element for the particular cell has already been determined previously.

iv. We fix the Lf phasing element depth and vary the Hf phasing element (i.e., rotated cross-groove) depth to generate the S-curve. Based on the desired reflection phase, calculated from equation (6.3), we select the Hf phasing element depth from the S-curve. This is the main idea behind the choice of the depths of the phasing elements for each cell of the single layer of the dual-band reflectarray.

v. This procedure is repeated for the entire reflectarray to complete the design for the dual-band offset-fed metal only reflectarray.

For example, one cell of the reflectarray, for which the Hf phasing element depth has to be determined, consists of Lf element depth = 1mm, which is shown in Fig. 6.20. We simulate the unit cell by fixing the Lf element depth = 1mm and vary the Hf phasing element depth from 0 to 3mm to generate the S-curve, shown in Fig. 6.20. This curve is then used for choosing the depth of the Hf phasing element to realize the desired reflection phase, calculated from equation (6.3) to direct the beam along $\theta = 0°$ and $\phi = 0°$.

Following the steps described above leads to the design of a fully functional reflectarray, is shown in Fig. 6.22, which operates in a dual-band (Ka/W-band) mode.

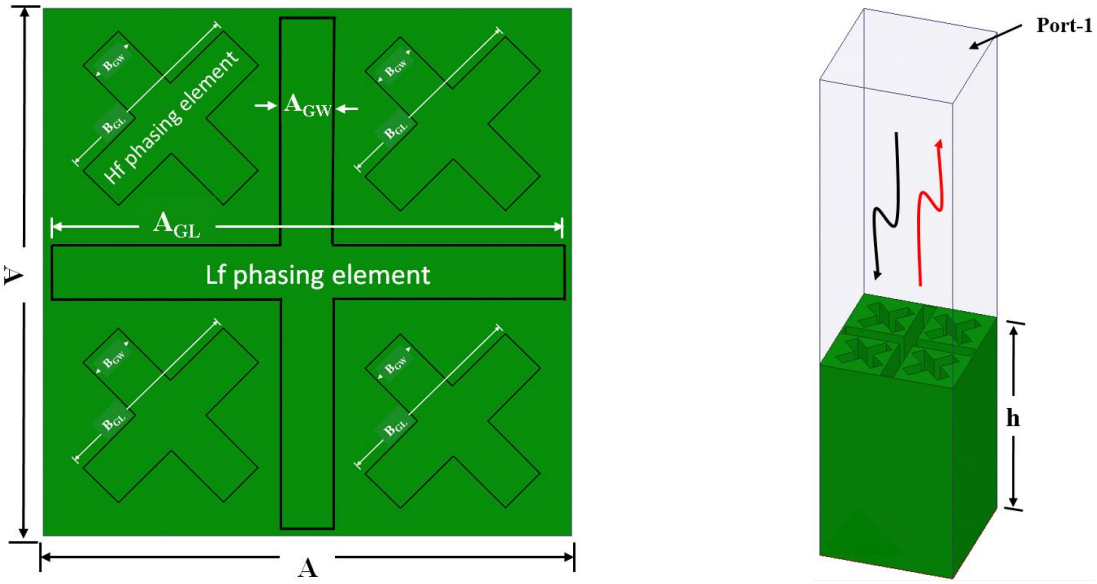

Fig. 6.19. Dual-band (Ka/W-band) phasing element (a) Top view; (b) Trimetric view

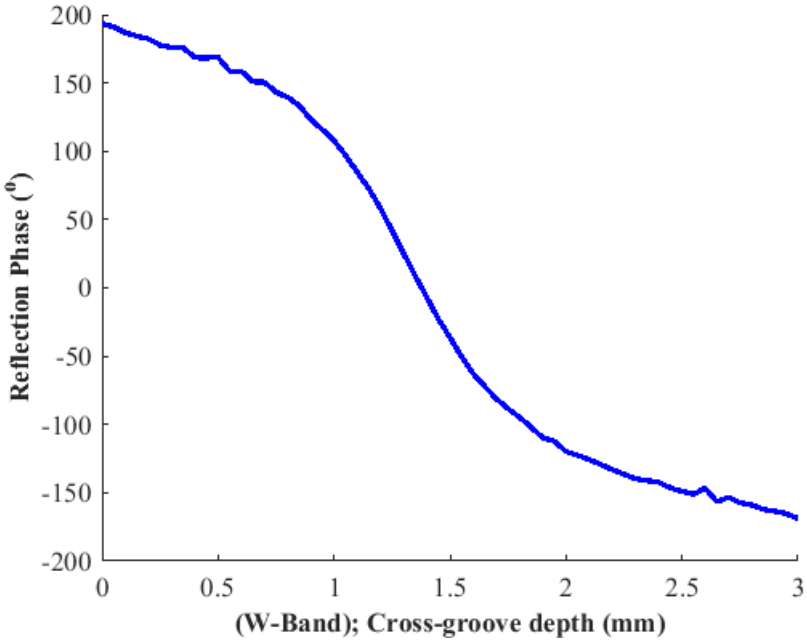

Fig. 6.20. Reflection phase of Hf phasing element depth by fixing Lf element depth = 1mm

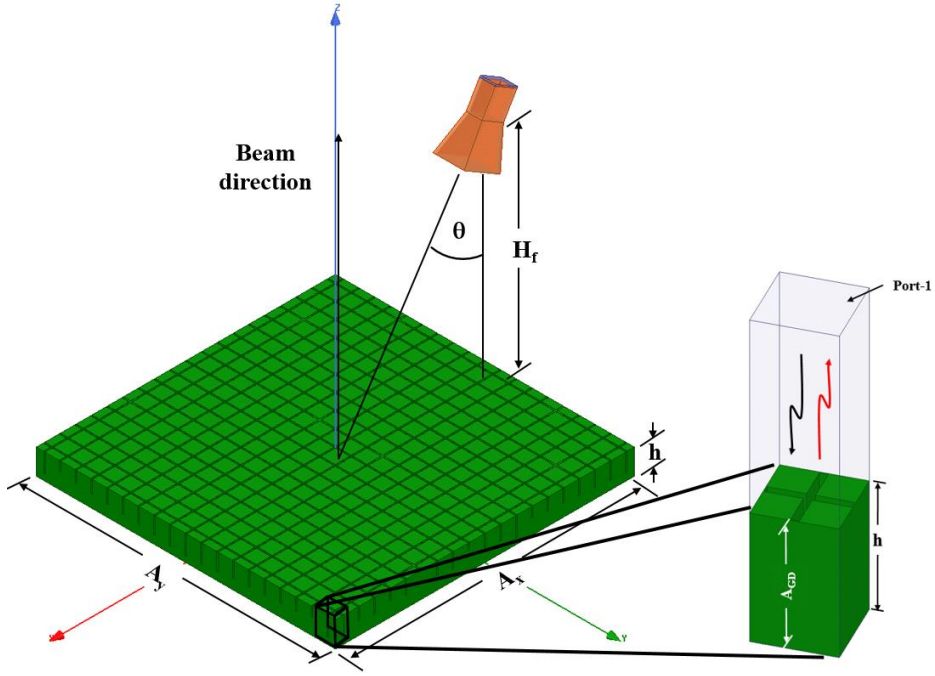

Fig. 6.21. Offset-fed Ka-band proposed MORA using cross-groove phasing element

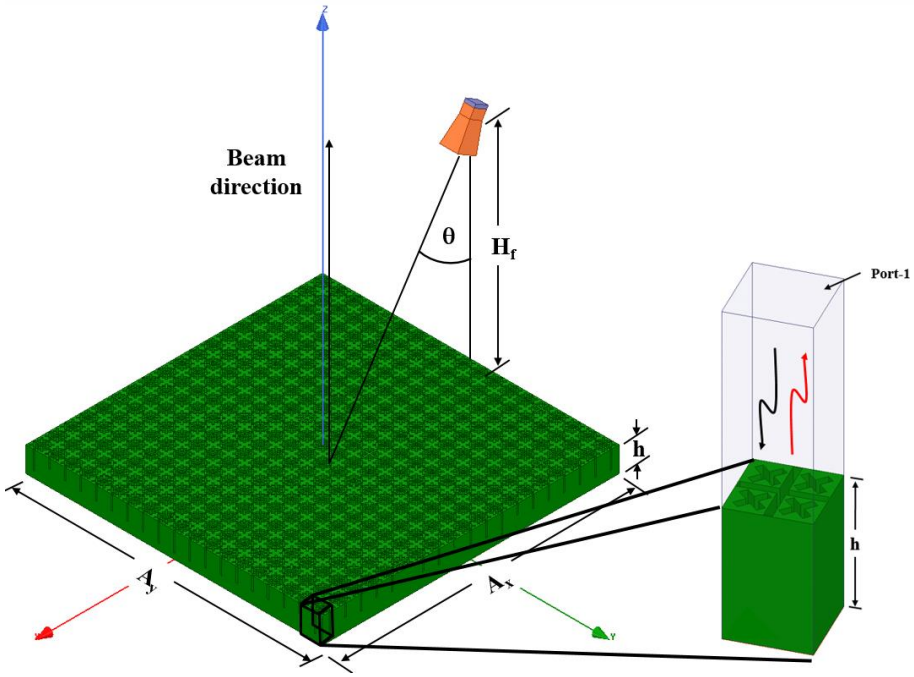

Fig. 6.22. Proposed dual-band metal-only reflectarray

To validate the radiation pattern in the normal direction, we start by checking the phase distribution of the field on a surface just above the cross, against the desired total reflection phase given in Table 6.3. These phase values are for the Ka-band phasing elements placed along the x-axis at y = 0*mm*.

Table 6.3: Phase comparison of Ka-band, cross-groove reflectarray for the beam angle of $\theta_b = 0°$

Location along x-axis (mm)	-(Ax/2) -45.05	-40.05	-35.05	-30.05	-25.05	-20.05	-15.05	-10.05	-5.05	0
Desired Total Reflected Phase (°)	0	0	0	0	0	0	0	0	0	0
Line placed at y = 0	-4.65	-5.16	-4.01	-3.01	-0.16	-0.26	-0.36	-0.73	-0.66	-0.11

Location along x-axis (mm)	5.05	10.05	15.05	20.05	25.05	30.05	35.05	40.05	+(Ax/2) 45.05
Desired Total Reflected Phase (°)	0	0	0	0	0	0	0	0	0
Line placed at y = 0	-0.16	-1.77	-2.25	-2.16	-1.11	-1.13	5.05	-6.41	-12.1

6.2.3.2 Simulation Results for Dual-Band Reflectarrays

Figs. 6.23 and 6.24 show the radiation patterns of the proposed dual-band (Ka/W) reflectarrays. We use Ka-band pyramidal horn (open-end dimension of 12.3mm x 8.9mm) and W-band pyramidal horn (open-end dimension of 4.83mm x 3.81mm) as the feed sources at the height of 75mm. The full wave simulation of 19x19 and 38x38 elements for the Ka and W-band reflectarrays, respectively, was conducted in HFSS with computation resources consisting of AMD Opteron Processor 6128 with 32 cores and 256GB of RAM installed.

Fig. 6.23 shows that the simulated gain for the Ka-band reflectarray in the presence of the W-band is found to be 29.1dBi at 35.6GHz with an aperture efficiency of 51.6% and sidelobe level of -21.1dB for the normally directed beam. The corresponding values for the W-band reflectarray in presence of Ka-band are gain of 31.5dBi at 94.05GHz and sidelobe level of -16.5dB. Figs. 6.25 and 6.26 show the gain response of the Ka-band reflectarray in the presence of the W-band elements and the W-band reflectarray in the presence of the Ka-band elements, respectively, which shows broadband behavior. We also show that the gain increases with frequency.

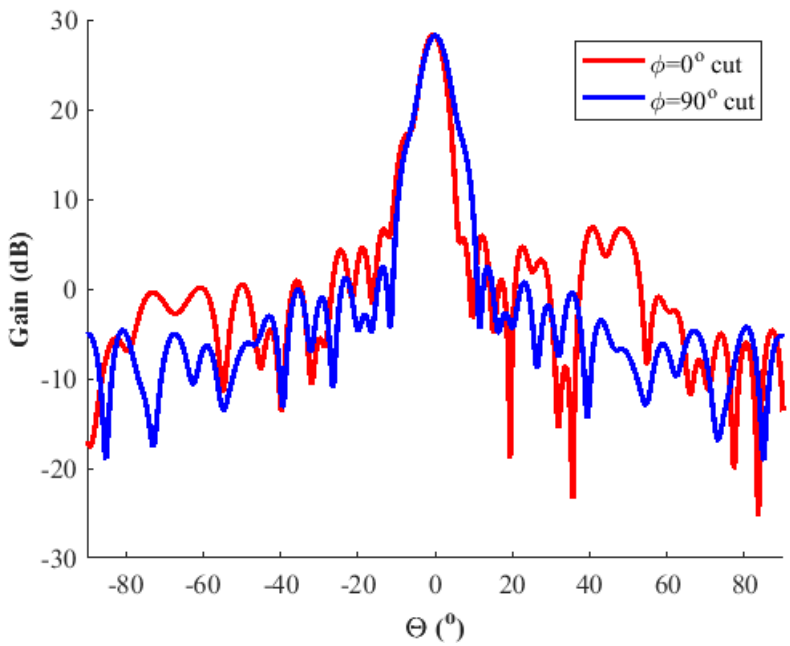

Fig. 6.23. Simulated radiation pattern of the dual-band MORA using cross-groove phasing element in presence of W-band elements

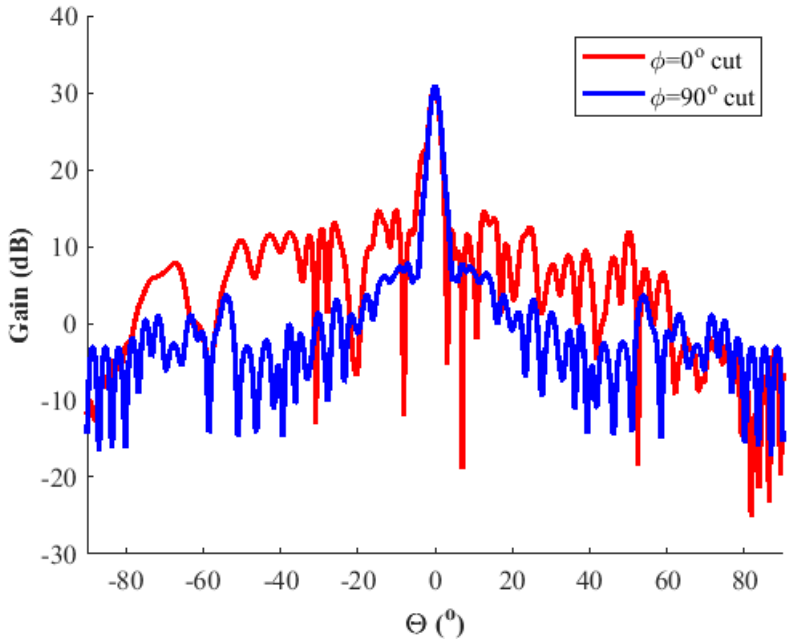

Fig. 6.24. Simulated radiation pattern of the dual-band MORA using cross-groove phasing element in presence of Ka-band elements

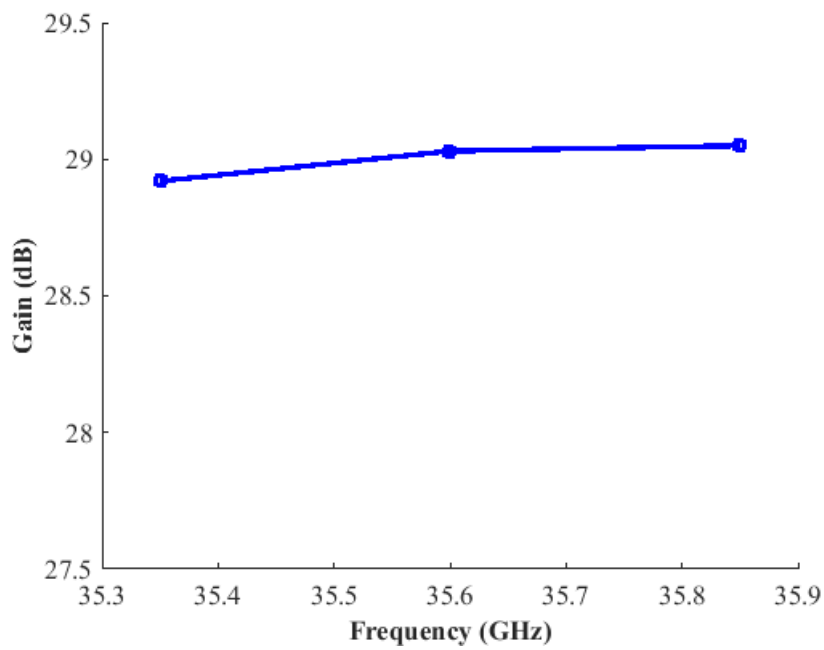

Fig. 6.25. Gain response within desired frequency band of the proposed Ka-band MORA in presence of W-band elements

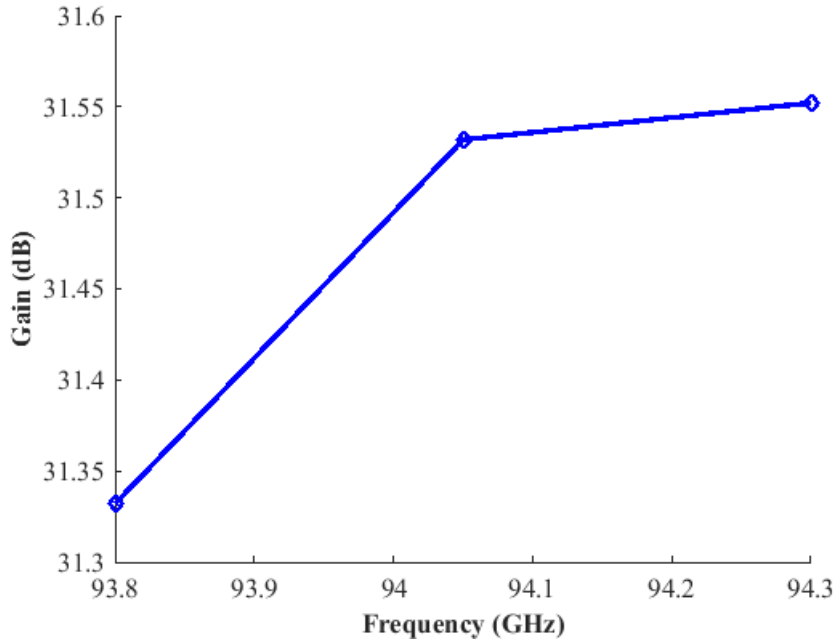

Fig. 6.26. Gain response within desired frequency band of the proposed W-band MORA in presence of Ka-band elements

6.3 Conclusions

In this chapter, we have presented three illustrative designs of metal-only reflectarray, designed by using 2D and 3D phasing elements such as cross-slot, 3D-cross and 3D-cross-groove configurations. These designs are suitable for space applications for which the use of dielectrics is not permissible. A novel phasing element is also introduced to compensate the reflection phases by varying the height and depth of the 3D-cross and cross-groove, respectively. The simulated radiation performances are shown in Table 6.4.

Table 6.4: Radiation performances of proposed MORA for the beam angle of $\theta_b = 0°$

Type of Phasing element for MORA Design	Frequency (GHz)	Gain (dBi)	Aperture Efficiency (η)	Sidelobe level (SLL)	Thickness (mm)
Cross-slot	35.6	26.2	25.1%	-21dB	0.787
3D-cross	35.6	28.9	47%	-19.7dB	4.9
3D-cross-groove	35.6	29.1	51.6%	-21.1dB	8

The proposed single- and dual-band metal-only reflectarrays show superior radiation performances compared to the high-gain reflectarray design proposed in [60]. The proposed designs also demonstrate increased gain performances for the desired frequency band from 35.35 to 35.85GHz with a step of 250MHz.

Chapter 7

Conclusions and Future Work

The objective of this dissertation has been to address some of the issues encountered in designing millimeter wave antennas using artificially engineered materials and metasurfaces. We investigated some problems and proposed techniques to solve them.

In Chapter 2, we showed how we can systematically design an RO, RO (ZP) and RO-based COTS planar lens using artificial dielectrics synthesized by implementing the DaD approach. The designed lens has the desirable characteristics of low loss and low reflection. Also, the synthesized lens performed well throughout the desired frequency band. Future work can include studying different types of FSS to improve the behavior of DaD lenses. Keeping the 3D-printing technique in mind, we could choose the type of FSS that would be more tolerant of the manufacturing standards.

In Chapter 3, we showed the DORA design, which uses the lens design approach (i.e., dielectric blocks) of flat lens design discussed in Chapter 2. These dielectric materials are arranged in the manner to point the beam in the specular direction (i.e., $\theta = 33°$; $\phi = 0°$). The proposed DORA design gives a linearly increasing gain variation compared to the bandwidth as typically reported in the literature (i.e., 10% for the designs based on the conventional approach). We can further utilize the DaD approach to implement the DORA design, which calls for dielectrics that are not available off-the-shelf.

In Chapter 4, we presented a new design of the flat lens, which utilizes multilayer frequency selective surfaces (FSSs) in *free space.* The lens can be space-qualified since, unlike conventional designs for lenses, it does not need to use dielectric materials. We have

also demonstrated a systematic procedure for realizing the requisite radially varying phase shifts, by using locally periodic multilayer FSSs to realize a lightweight, low-profile, and low-cost design. Future work could include exploring different FSS elements that would help to improve the gain performance and realize a lightweight and low-profile design.

In Chapter 5, we demonstrated that the beam could be systematically scanned from boresight to 45° by rotating the metasurface-based superstrate that loads the 1×10 element linear array. We also pointed out that the phase-shifting mechanism discussed was only viable for the linear polarization case and that a different design philosophy is needed to deal with the circularly polarized case. Further research is needed to develop the circular polarization-based phase-shifter for applications like reconfigurable arrays, etc.

We concluded the work by investigating metal-only reflectarray antenna designs in Chapter 6. We presented three illustrative designs of metal-only reflectarrays, designed by using 2D and 3D phasing elements such as cross-slot, 3D-cross, and 3D-cross-groove configurations. These designs are suitable for space applications for which the use of dielectrics is not permissible. A novel phasing element was also introduced to compensate the reflection phases by varying the height and depth of the 3D-cross and cross-groove. The proposed single- and dual-band metal-only reflectarrays show superior radiation performances compared to the existing high-gain reflectarray designs. We can further explore the design by making it work for the tri-band application.

Publications from this Dissertation

Journals

1. "3D-printed planar graded index lenses," *IET Microwaves, Antennas & Propagation*, vol. 10, no. 13, pp. 1411–1419, 2016.
2. "Flat lens design using artificially engineered materials," *Progress In Electromagnetics Research C*, Vol. 64, 71–78, 2016.
3. "Flat-base broadband multibeam Luneburg lens for wide-angle scan", *J. Electromagnetics. Waves Application.* vol. 29, no. 10, pp. 1329-1341, 2015.

Conference Proceedings

1. "Offset-fed Metal-only Reflectarray Antenna Design Using 3D-cross Elements," 2018 *12th European Conference on Antennas and Propagation (EuCAP)*, London, UK, 2018. (submitted)
1. "Offset-fed Metal-only Reflectarray Antenna Designs," *IEEE Asia-Pacific Conference on Antennas and Propagation (APCAP 2017)*, Xi'an, China, October 16–19, 2017 (accepted)
2. "A Novel Approach to Designing Phase Shifters for Array Antennas for Satellite Communication by using Reconfigurable FSS Screens" *PIERS*, Shanghai, China, August 8–11, 2016
3. "Flat Lens Design Using Space-qualifiable Multilayer Frequency Selective Surfaces," *IEEE APS–URSI*, Fajardo, Puerto Rico, June 26–July 1, 2016

4. "Synthesizing Broadband Low–loss Artificially Engineered Materials (Aka Metamaterials) for Antenna Applications," *International Symposium on Antennas and Propagation (ISAP2015)*, Hobart, Tasmania, Australia, November 9–12, 2015
5. "Low Profile Lens and Reflectarray Design for MM Waves," *IEEE APS–URSI*, Vancouver, BC, Canada, July 19–25, 2015
6. "Techniques for Synthesizing Artificial Dielectrics for Lens and Reflectarray Designs," *Loughborough Antennas and Propagation Conference (LAPC)*, Nov. 10–11, 2014
7. "A Technique for Designing Flat Lenses Using Artificially Engineered Materials," *IEEE APS–URSI*, Memphis, TN, USA, July 6–12, 2014

Bibliography

[1] Zhang, K., X. Ding, L. Zhang, and Q. Wu, "Anomalous three-dimensional refraction in the microwave region by ultra-thin high efficiency metalens with phase discontinuities in orthogonal directions," *New Journal of Physics*, Vol. 16, No. 10, 103020, 2016.

[2] Gagnon, N., A. Petosa, and D. A. Mcnamara, "Thin microwave phase-shifting surface lens antenna made of square elements," *Electronics Letters*, Vol. 46, No. 5, 327–329, Mar. 4, 2010.

[3] Phillion, R. H. and M. Okoniewski, "Lenses for circular polarization using planar arrays of rotated passive elements," *IEEE Transactions on Antennas and Propagation*, Vol. 59, No. 4, 1217–1227, Apr. 2011.

[4] Gagnon, N. and A. Petosa, "Using rotatable planar phase shifting surfaces to steer a high-gain beam," *IEEE Transactions on Antennas and Propagation*, Vol. 61, No. 6, 3086–3092, Jun. 2013.

[5] Zhang, K., X. Ding, D. Wo, F. Meng, and Q. Wu, "Experimental validation of ultra-thin metalenses for N-beam emissions based on transformation optics," *Applied Physics Letters*, Vol. 108, No. 5, 053508, 2016.

[6] Zhang, Y., R. Mittra, and W. Hong, "A zoned two-layer flat lens design," *International Workshop on Antenna Technology (iWAT)*, 412–415, Mar. 7–9, 2011.

[7] Zhang, Y., R. Mittra, and W. Hong, "On the synthesis of a flat lens using a wideband low-reflection gradient-index metamaterial," *Journal of Electromagnetic Waves and Applications*, Vol. 25, No. 16, 2178–2187, 2011.

[8] R. Yang, W. Tang, Y. Hao, and I. Youngs, “A coordinate transformation based broadband flat lens via microstrip array,” IEEE Antennas and Wireless Propagation Letters, Vol. 10, pp. 99–102, 2011.

[9] Yang, R., W. Tang, and Y. Hao, “A broadband zone plate lens from transformation optics,” *Opt. Express*, Vol. 19, No. 13, 12348–12355, 2011.

[10] Jain, S., M. Abdel-Mageed, and R. Mittra, “Flat-lens design using field transformation and its comparison with those based on transformation optics and ray optics,” *IEEE Antennas and Wireless Propagation Letters*, Vol. 12, 777–780, 2013.

[11] Arya, R. K., S. Pandey, and R. Mittra, “Synthesizing broadband low-loss artificially engineered materials (Aka metamaterials) for antenna applications,” *International Symposium on Antennas and Propagation (ISAP2015)*, Hobart, Tasmania, Australia, Nov. 9–12, 2015.

[12] Arya, R. K., S. Pandey, and R. Mittra, “A technique for designing flat lenses using artificially engineered materials,” *IEEE APS-URSI*, Memphis, TN, USA, Jul. 6–12, 2014.

[13] Vardaxogolu, Y., R. Mittra, R. K. Arya, and S. Pandey, “Techniques for synthesizing artificial dielectrics for lens and reflectarray designs,” *Loughborough Antennas and Propagation Conference (LAPC)*, Nov. 10–11, 2014.

[14] Pandey, S., R. K. Arya, and R. Mittra, “Low profile lens and reflectarray design for MM waves,” *IEEE APS-URSI*, Vancouver, BC, Canada, Jul. 19–25, 2015.

[15] H. Jasik, *Antenna Engineering Handbook*, Chapters 12 and 15, McGraw - Hill, New York, 1961.

[16] J. Huang and J. A. Encinar, Reflectarray Antennas: John Wiley & Sons, 2007.

[17] R. E. Munson and H. Haddad , “ Microstrip reflectarray for satellite communication and RCS enhancement and reduction , ” U.S. patent 4,684,952, Washington, D.C., August 1987 .

[18] D. M. Pozar, S. D. Targonski, and H. D. Syrigos, "Design of millimeter wave microstrip reflectarrays," IEEE Trans. on Antennas and Propag., Vol. 45, pp. 287-296, 1997.

[19] D. M. Pozar, S. D. Targonski, and R. Pokuls, "A shaped-beam microstrip patch reflectarray," IEEE Trans. on Antennas and Propagation, Vol. 47, pp. 1167-1173, 1999.

[20] D. Berry, R. Malech, and W. Kennedy, "The reflectarray antenna," IEEE Trans. on Antennas Propag., Vol. 11, No. 6, pp. 645-651, Nov. 1963.

[21] C. S. Malagisi, "Microstrip disc element reflect array," in Electronics and Aerospace Systems Convention, 1978, pp. 186-192.

[22] D. M. Pozar and T. A. Metzler, "Analysis of a reflectarray antenna using microstrip patches of variable size," Electronics Letters, Vol. 29, pp. 657-658, 1993.

[23] R. E. Munson and H. Haddad, "Microstrip reflectarray for satellite communication and RCS enhancement and reduction," US patent 4684 952, Aug. 1987.

[24] J. Luther, "Microstrip patch electrically steerable parasitic array radiators," Diss. University of Central Florida Orlando,, Florida, 2013.

[25] J. Huang, "Microstrip reflectarray antenna for the SCANSCAT radar application," in Jet Propulsion Lab, Pasadena, CA, No 90-45, Nov. 1990.

[26] D. M. Pozar, S. D. Targonski, and R. Pokuls, "A shaped-beam microstrip patch

reflectarray," IEEE Trans. Antennas Propagation, Vol. 47, pp. 1167-1173, 1999.

[27] J. Huang and A. Feria, "A 1-m X-band inflatable reflectarray antenna," Microwave and Optical Technology Letters, Vol. 20, pp. 97-99, 1999

[28] D. M. Pozar, "Bandwidth of reflectarrays," in *Electronics Letters*, vol. 39, no. 21, pp. 1490-1491, 16 Oct. 2003.

[29] H. Hasani, M. Kamyab, and A. Mirkamali, “Broadband reflectarray antenna incorporating disk elements with attached phase-delay lines,” IEEE Antennas Wireless Propagation. Letter, Vol. 9, pp. 156–158, 2010.

[30] H. Hasani, M. Kamyab, and A. Mirkamali, “Low cross-polarization reflectarray antenna,” IEEE Trans. Antennas Propagation, vol. 59, no. 5, pp. 1752–1756, May 2011.

[31] R. Shamsaee and Z. Atlasbaf, “Design and implementation of a broadband single layer circularly polarized reflectarray antenna,” IEEE Antennas Wireless Propagation. Letter, Vol. 11, pp. 973–976, 2012.

[32] I. Derafshi, N. Komjani, and M. Mohammadirad, “Single-layer broadband reflectarray antenna by using quasi-spiral phase delay line,” IEEE Antennas Wireless Propagation. Letter, Vol. 14, pp. 84–87, 2015.

[33] D.M. Pozar, Microwave engineering, Wiley, Hoboken, NJ 2005, chapter 6.

[34] Y. Zhang, R. Mittra and W. Hong, “On the synthesis of a flat lens using a wideband low-reflection gradient–index metamaterial,” J. of Electromagnetic Waves and Appl., Vol. 25, pp. 2178–2187, 2011.

[35] D. McGrath, “Planar three-dimensional constrained lenses,” IEEE Trans. Antennas Propagation 34, 46–50 (1986).

[36] D. T. McGrath, P. M. Proudfood, and M. A. Mehalic, “The microstrip constrained lens,” Microwave J. 38, 24 (1995).

[37] S. Jain, M. Abdel–Mageed and R. Mittra, “Flat–Lens Design Using Field Transformation and Its Comparison With Those Based on Transformation Optics and Ray Optics,” IEEE Antennas and Wireless Propagation Letters, Vol. 12, pp. 777–780, 2013.

[38] Y. Zhang, R. Mittra and W. Hong, "Systematic design of planar lenses using artificial dielectrics," *2010 IEEE Antennas and Propagation Society International Symposium*, Toronto, ON, 2010, pp. 1-4.

[39] R. K. Arya, S. Pandey and R. Mittra, “A Technique for Designing Flat Lenses Using Artificially Engineered Materials,” IEEE APS–URSI, Memphis, TN, USA, July 6–12, 2014.

[40] Y. Vardaxogolu, R. Mittra, R. K. Arya and S. Pandey, “Techniques for Synthesizing Artificial Dielectrics for Lens and Reflectarray Designs,” Loughborough Antennas and Propagation Conference (LAPC), Nov. 10– 11, 2014.

[41] S. Pandey, R. K. Arya and R. Mittra, “Low Profile Lens and Reflectarray Design for MM Waves,” IEEE APS–URSI, Vancouver, BC, Canada, July 19–25, 2015.

[42] R. K. Arya, S. Pandey and R. Mittra, “Synthesizing Broadband Low– loss Artificially Engineered Materials (Aka Metamaterials) for Antenna Applications,” International Symposium on Antennas and Propagation (ISAP2015), Hobart, Tasmania, Australia, November 9–12, 2015.

[43] De Song Wong, Shi-Wei Qu and Chi Hou Chan, Frequency Selective Surfaces,

Chapter in *Handbook of Antenna Technologies*, Springer, Singapore 2015.

[44] N. Kundtz and D. R. Smith, “Extreme-angle broadband metamaterial lens,” Nat. Mater., Vol. 9, No. 123, pp. 129–132, 2009.

[45] R. Yang, W. Tang and Y. Hao, “A broadband zone plate lens from transformation optics,” Opt. Express, Vol. 19, No. 13, pp. 12348–12355, 2011.

[46] G. Perez-palomino, J. A. Encinar, M. Barba and E. Carrasco, “Design and evaluation of multi-resonant unit cells based on liquid crystals for reconfigurable reflectarrays,” in *IET Microwaves, Antennas & Propagation*, vol. 6, no. 3, pp. 348-354, February 21 2012..

[47] P. T. Teo, K. A. Jose, Y. B. Gan and V. K. Varadan, "Beam scanning of array using ferroelectric phase shifters," in *Electronics Letters*, vol. 36, no. 19, pp. 1624-1626, 14 Sep 2000.

[48] R. Garg, P. Bhartia, I. Bahl, & A. Ittipiboon, *Microstrip antenna design handbook*, Artech, j. A. House, boston, london, 2001.

[49] J. Shaker, M. R. Chaharmir, and J. Ethier, Reflectarray Antennas: Analysis, Design, Fabrication and Measurement, Artech House Antennas and Propagation Library, Artech House, 2013.

[50] J. Huang and J. Encinar, Reflectarray Antennas. John Wiley & Sons, 2008.

[51] J. Budhu and Y. Rahmat-Samii, “Understanding the appearance of specular reflection in offset fed reflectarray antennas,” in Antennas and Propagation (APSURSI), 2011 IEEE International Symposium on, pp. 97–100, IEEE, 2011.

[52] D. M. Pozar, S. D. Targonski, and H. Syrigos, “Design of millimeter wave

microstrip reflectarrays," IEEE transactions on antennas and propagation, Vol. 45, No. 2, pp. 287–296, 1997.

[53] R. Mittra, S. Pandey and Ravi Arya, "Low Profile Lens and Reflectarray Design for MM Waves," IEEE APS–URSI, Vancouver, BC, Canada, July 19–25, 2015

[54] D. Berry, R. Malech and W. Kennedy, "The reflectarray antenna," IEEE Transactions on Antennas and Propagation, Vol. 11, No. 6, pp. 645–651, 1963.

[55] G. Carluccio, A. Mazzinghi and A. Freni, "Design of complementary reflectarray," Electronics Letters, Vol. 50, No. 1, pp. 16–17, 2014.

[56] Y. H. Cho, W. J. Byun, and M. S. Song, "High gain metal-only Reflectarray antenna composed of multiple rectangular grooves," IEEE Transactions on Antennas and Propagation, Vol. 59, No. 12, pp. 4559–4568, 2011.

[57] R. Deng, F. Yang, S. Xu and M. Li, "A low-cost metal-only Reflectarray using modified slot-type phoenix element with 360 phase coverage," IEEE Transactions on Antennas and Propagation, Vol. 64, No. 4, pp. 1556–1560, 2016.

[58] W. Lee, M. Yi, J. So and Y. J. Yoon, "Non-resonant conductor Reflectarray element for linear reflection phase," Electronics Letters, Vol. 51, No. 9, pp. 669–671, 2015.

[59] H.-T. Chou, C.-Y. Lin and M.-H. Wu, "A high efficient Reflectarray antenna consisted of periodic all-metallic elements for the Ku-band DTV applications," IEEE Antennas and Wireless Propagation Letters, Vol. 14, pp. 1542–1545, 2015.

[60] R. Deng, F. Yang, S. Xu and M. Li, "A 100 GHz metal-only reflectarray for high-gain antenna applications," IEEE Antennas Wireless Propagation. Letter. Vol. 15, pp. 178–181, 2016.

Vita

Shaileshachandra V Pandey

Shaileshachandra V Pandey is a doctoral student in the Department of Electrical Engineering at the Pennsylvania State University under the eminent guidance of Dr. Raj Mittra. Currently, he is involved in the design and analysis of 2D and 3D FSS elements for lenses, transmitarray, phase-shifter and reflectarray designs. He received his Master of Technology (M.Tech.) Degree in RF and Microwave Engineering from the Indian Institute of Technology, Kharagpur, India in 2008. Before joining Penn State University in August, 2012, he worked as an Assistant Professor at Nirma University, Gujarat, India for four years from 2008 to 2012. His research interests include antenna design for microwave and millimeter wave applications, analysis of frequency selective surfaces (FSSs) for low-profile and high-gain antenna performances and RF circuit design. He has authored a number of publications in leading IEEE journals and conferences.